Technische Universität Ilmenau
Faculty of Computer Science and Automation
Department of Control Engineering

Norwegian University of Science and Technology
Faculty of Information Technology and Electrical Engineering
Department of Engineering Cybernetics

Master Thesis

Modeling and Control of Spacecraft Attitude - Control Allocation for a Variable Pointing and Maneuvering Satellite

To achieve the degree:

Master of Science (M. Sc.)

---

submitted by:	Frieda Franke
date of submission:	9 July 2021
date and place of birth:	6 June 1996 in Leipzig
course of studies:	Industrial Engineering
supervisor TU Ilmenau:	Prof. Dr.-Ing. Johann Reger
supervisor NTNU:	Prof. Dr.-Ing. Jan Tommy Gravdahl

For Alexandra

Declaration

I declare that the work is entirely my own and was produced with no assistance from third parties.
I certify that the work has not been submitted in the same or any similar form for assessment to any other examining body and all references, direct and indirect, are indicated as such and have been cited accordingly.

(Frieda Franke)
Ilmenau, 9 July 2021

Abstract

A nonlinear state space model is developed, providing the kinematics and dynamics equations for a rigid body satellite actuated by reaction wheels and magnetorquers. Control allocation deals with the problem of how to distribute the control vector among a redundant set of actuators. Due to physical actuator limitations, a constrained control allocation problem is given. When performing aggressive maneuvers, there is the risk that no feasible solution is found because of the violation of constraints. The nonlinear state space model is implemented in Matlab and Simulink, applying a PD controller. For modeling, the HYPSO, a smallsatellite at NTNU, is used as a case study. The performance of the original model is compared with the model using a specific control allocation method. The cascaded generalized inverses method introduced as a computationally efficient method in the literature is applied to the spacecraft model. For the attitude cases with no full controllability, it is shown through numerical simulations that the spacecraft models applying the cascaded generalized inverses control allocation method minimize the control error compared to the original spacecraft model.

Acknowledgment

This master's thesis is part of the Erasmus exchange program between the control engineering group at TU Ilmenau and the department of engineering cybernetics at NTNU. Many thanks belong to Professor Reger and Professor Gravdahl, who have encouraged the exchange and regularly provided constructive feedback. In addition, thanks to the employees of the International Offices in Ilmenau and Trondheim, who supported the organization of the exchange semester.
Special thanks belong to the co-supervising Ph.D. research fellow Mariusz E. Grøtte, who supported the implementation and, together with the other members of the HYPSO ADCS team, gave a very extensive project onboarding. Thanks also to the Ph.D. research fellow Bjørn A. Kristiansen for interesting discussions and proofreading.

Nomenclature

$\gamma \in \mathbb{R}$	weight scalar for control allocation [–]
$\boldsymbol{\epsilon}$	Euler parameter (imaginary vector) in $\mathbb{S}^3$ [–]
η	Euler parameter (scalar) in $\mathbb{S}^3$ [–]
$\boldsymbol{\tau}^b_{\mathrm{drag}} \in \mathbb{R}^{\mathrm{n}}$	torque due to aerodynamic drag [Nm]
$\boldsymbol{\tau}^b_{\mathrm{ext}} \in \mathbb{R}^{\mathrm{n}}$	sum of external disturbance torques [Nm]
$\boldsymbol{\tau}^b_{\mathrm{gg}} \in \mathbb{R}^{\mathrm{n}}$	torque due to gravity gradient [Nm]
$\boldsymbol{\tau}^b_{\mathrm{m}} \in \mathbb{R}^{\mathrm{n}}$	torque due to magnetic dipole [Nm]
$\boldsymbol{\tau}^b_{\mathrm{mtq}} \in \mathbb{R}^{\mathrm{n}}$	magnetic control torque [Nm]
$\boldsymbol{\tau}^w_{\mathrm{s}} \in \mathbb{R}^{\mathrm{r}}$	torque produced by reaction wheels [Nm]

$\boldsymbol{\tau}^b_{\mathrm{srp}} \in \mathbb{R}^{\mathrm{n}}$	torque due to solar radiation pressure [Nm]
$\boldsymbol{\tau}^b_{\mathrm{u}} \in \mathbb{R}^{\mathrm{n}}$	control input vector [Nm]
$\Phi = \begin{bmatrix} \phi \\ \theta \\ \psi \end{bmatrix}$	Euler angles (roll, pitch, and yaw) [°] or [rad]
$\boldsymbol{\omega}^a_{ab}$	angular velocity of $\mathcal{F}_b$ relative to $\mathcal{F}_a$, expressed in $\mathcal{F}_a$ [°/s] or [rad/s]
$\boldsymbol{\omega}^w_{\mathrm{s}} \in \mathbb{R}^{\mathrm{r}}$	vector of wheel angular velocities [°/s] or [rad/s]
$\tilde{\boldsymbol{\omega}}^b_{ob} \in \mathbb{R}^{\mathrm{n}}$	angular velocity error vector [°/s] or [rad/s]
$\boldsymbol{\Omega}_{\mathrm{u}}$	set of feasible controls [–]
$\boldsymbol{\Omega}_{\mathrm{v}}$	set of attainable controls [–]
$\mathbf{A} \in \mathbb{R}^{\mathrm{n}\times\mathrm{r}}$	reaction wheel assembly matrix [–]
$\mathbf{B} \in \mathbb{R}^{\mathrm{n}\times\mathrm{r}}$	control effectiveness matrix [–]
$\mathbf{B}^b$	magnetic field vector, expressed in body frame [T]
$\mathbf{h}^b$	total angular momentum, expressed in body frame [Nms]
$\mathbf{I}_{\mathrm{n}\times\mathrm{n}}$	identity matrix [–]

$\mathbf{J} \in \mathbb{R}^{\mathrm{n}\times\mathrm{n}}$	inertia matrix of spacecraft $\left[\mathrm{kgm}^2\right]$
$\mathbf{J}_\mathrm{s} \in \mathbb{R}^{\mathrm{r}\times\mathrm{r}}$	inertia matrix of RWA $\left[\mathrm{kgm}^2\right]$
$\mathbf{m}^b_\mathrm{mtq}$	magnetorquer moment $\left[\mathrm{Am}^2\right]$
$\mathbf{P}_\mathrm{s}$	reaction wheel power [W]
$\mathbf{R}^a_b$	rotation matrix from frame $\mathcal{F}_a$ to frame $\mathcal{F}_b$ [–]
$\mathbb{R}^\mathrm{n}$	n-dimensional space of real scalar numbers [–]
$\mathbb{R}^+$	set of positive, real scalar numbers [–]
$\mathbf{S}(\cdot)$	skew-symmetric operator [–]
$\mathbf{T}(\cdot)$	angular velocity transformation matrix [–]
$\mathbf{u} \in \mathbb{R}^\mathrm{r}$	optimal control vector [Nm]
$\mathbf{v} \in \mathbb{R}^\mathrm{n}$	commanded virtual control vector [Nm]
$\mathbf{W}_\mathrm{u} \in \mathbb{R}^{\mathrm{r}\times\mathrm{r}}$	matrix of weights for $\mathbf{u} \in \mathbb{R}^\mathrm{r}$ [–]
$\mathbf{W}_\mathrm{v} \in \mathbb{R}^{\mathrm{n}\times\mathrm{n}}$	matrix of weights for $\mathbf{v} \in \mathbb{R}^\mathrm{n}$ [–]

Abbreviations

ADCS	attitude determination and control system
CA	control allocation
CGI	cascaded generalized inverse
CL	closed-loop
LFC	Lyapunov function candidate
MTQ	magnetorquer
RMSE	root mean square error
RW	reaction wheel
RWA	reaction wheel assembly
SO(3)	special orthogonal group of order 3

Contents

List of Figures

List of Tables

Chapter 1

Introduction

1.1 Motivation

A satellite needs to be positioned where it needs to be to perform orbit maneuvers. Therefore, the attitude determination and control system (ADCS) needs to control the satellite's angular rotation around three axes.
Since an overactuated mechanical system with a redundant set of actuators is given, a control allocation problem is handled. Control allocation is particularly relevant when handling problems such as the loss of actuators due to saturation or failure. It is necessary to establish proper control allocation where the satellite performs various maneuvers specified in Chapter 1.3.1. The intention is to conclude for which attitude cases specific control allocation methods perform better than the original model.
This master's thesis presents a solution to the problem explained for the case study of the HYPSO. The HYPSO is a smallsatellite developed at NTNU SmallSat Lab. The abbreviation HYPSO stands for hyperspectral imaging smallsatellite for ocean observation. The satellite has a hyperspectral camera onboard, which acquires images while the satellite performs various maneuvers. The satellite images help observe oceanographic phenomena along the coast of Norway to monitor climate change.

1.2 Previous Work

1.2.1 Research at NTNU

Research for attitude control has been done within the last three years, especially on sliding mode control [1], quaternion-based generalized super-twisting algorithm [2], development of a testbed for hardware and software testing and verification [3], and maximum hands-off control [4]. A significant milestone of research by the ADCS team at NTNU SmallSat Lab is the specification of the slew maneuver in the context of the HYPSO mission [5]. Currently, another research focus is on energy-optimal spacecraft attitude control. The implementation results are under development on an internal GitHub project, explained in Chapter 5.2.1.

1.2.2 Literature Review on Control Allocation

Control allocation (CA) is applied on marine systems, aerospace applications, and in the automotive sector [6, p. 1087]. CA problems are typically formulated as optimization problems. There exist various CA methods in the literature reviewed. The literature distinguishes between static and dynamic as well as constrained and unconstrained CA methods. Constraints are, for example, energy or fuel consumption, actuator rate limitations, and other operational constraints. CA methods vary according to the inclusion of actuator constraints and the computational method applied [7, p. 344]. In [6] and [8], a brief overview of commonly used CA methods is presented. In [9], the differences between unconstrained and constrained CA methods are introduced.
The direct CA method is presented in [10], [11], and [12]. In [13], [9], [7], and [14], the dynamic CA method is introduced. The difference between both CA methods is that a static CA provides the same control distribution regardless of the system performing a maneuver or steady-state. When using a dynamic CA algorithm, the results depend not only on the current distribution but also on the previous distribution [9, p. 2].
For CA, the Moore-Penrose inverse is commonly used. The redistributed pseudoinverse method is also called cascaded generalized inverses (CGI) method. This CA method requires only a finite number of iterations but does not always provide an optimal solution. Simple CA schemes using generalized inverse matrices can be designed directly using either a tailored generalized inverse or the "best" generalized inverse [10, p. 725]. The tailored generalized inverse to be found fits exactly the attainable moment subset at particular points on the boundary. In the context of closed-form solutions within sectors,

tailored generalized inverses are useful [12, p. 379]. The "best" generalized inverse is an inverse maximizing the area of attainable moment space without violation of the control constraints [10, p. 723]. Complementary to the Moore-Penrose generalized inverse, [8] introduces a positive-definite and symmetric weighting matrix considering actuator constraints. The concept of a weighted generalized inverse matrix is also introduced in [15] and [16]. Additionally, in [13], the tuning of different CA methods using weight matrices is discussed.
Another CA technique, daisy chaining, is discussed in [10] and [17]. The daisy chaining CA method separates the available controls into at least two groups, and each group generates arbitrary combinations of the moments desired [10, p. 724].
Furthermore, the literature distinguishes between cooperative and non-cooperative CA methods. For example, daisy chaining is a non-cooperative CA method. Cooperative CA methods are those where all available controls are modified simultaneously to fulfill a time-varying command.
An alternative to CA is optimal control. Both CA and optimal control are tools to resolve actuator redundancy [18, p. 142]. In [18], the relationship between optimal control and CA is discussed. CA differs from optimal control in that CA separates the regulation task from the control distribution task [18, p. 137].

1.3 Thesis Objectives and Outline

1.3.1 Thesis Objectives

The objectives of this master's thesis are

1. to review the literature on control allocation briefly,
2. to build a mathematical model of the kinematics and dynamics of a rigid body spacecraft and its actuators, and
3. to determine a torque distribution law for nonlinear control of a time-varying attitude tracking problem where the satellite performs nadir pointing and single-axis slew maneuvers.

1.3.2 Thesis Contributions

For the application to attitude control of a rigid body spacecraft, the following contributions in the master's thesis are:

1. A modeling and simulation framework for the nonlinear attitude control of a rigid body spacecraft actuated by reaction wheels and magnetorquers is built.

2. The cascaded generalized inverses CA method is applied to the spacecraft model and is simulated for different attitude tracking cases, nadir pointing, and single-axis slew maneuver, with and without full controllability.

3. By numerical simulations, the models are compared to evaluate when CA makes sense and when it does not.

1.3.3 Thesis Outline

The introductory Chapter presents the thesis motivation and reviews the literature on control allocation. The second Chapter introduces preliminary mathematical concepts necessary for modeling, including the introduction of different reference frames, rotations between frames, attitude parameterizations, and stability theory. The third Chapter obtains the kinematic and dynamic equations for a rigid body satellite actuated by four reaction wheels and three magnetorquers. Part of this is also the modeling of external disturbance torques. The following Chapter explains different methods for distributing the torque command from the attitude controller to the reaction wheels, considering actuator failure for redundancy. The fifth Chapter presents the numerical simulations with Matlab and Simulink, the simulation setup, including noise on the angular velocity and attitude measurement, and uncertainties in the reaction wheel assembly. In the sixth Chapter, the simulation results are shown, and practical implications of the results are discussed. The final Chapter summarizes the findings of the thesis and outlines future work.

Chapter 2

Preliminaries

2.1 Reference Frames

Coordinate frames or reference frames describe the satellite's position and attitude and specify the components' spatial relationships.

2.1.1 Notation

A frame is denoted by $\mathcal{F}$ with frame-specifying subscripts i, e, o, b, and w. Representing a vector $\mathbf{x}$ in a frame $\mathcal{F}_b$ gives $\mathbf{x}^b$.
Differentiating a vector $\mathbf{x}^b$ with respect to time in the frame $\mathcal{F}_b$ gives

$$\dot{\mathbf{x}}^b = \frac{\mathrm{d}^b}{\mathrm{dt}}\mathbf{x}^b. \tag{2.1}$$

Every frame consists of three orthonormal unit vectors.

$$\hat{\mathbf{x}} = \frac{\mathbf{x}}{|\mathbf{x}|},\ \hat{\mathbf{y}} = \frac{\mathbf{y}}{|\mathbf{y}|},\ \text{and}\ \hat{\mathbf{z}} = \frac{\mathbf{z}}{|\mathbf{z}|} \qquad \text{[10, p. 718]} \tag{2.2}$$

denote unit vectors in the direction x, y, and z.
Calculating the cross-product $\mathbf{x} \times \mathbf{y}$ between vectors in three dimensions, the skew-

symmetric matrix $\mathbf{S}(\mathbf{x})$ is used. The cross-product is defined as $\mathbf{S}(\mathbf{x})\mathbf{y}$, where

$$\mathbf{S}(\mathbf{x}) = \begin{bmatrix} 0 & -\mathrm{x}_3 & \mathrm{x}_2 \\ \mathrm{x}_3 & 0 & -\mathrm{x}_1 \\ -\mathrm{x}_2 & \mathrm{x}_1 & 0 \end{bmatrix}, \ \mathbf{x} = \begin{bmatrix} \mathrm{x}_1 \\ \mathrm{x}_2 \\ \mathrm{x}_3 \end{bmatrix} \in \mathbb{R}^{\mathrm{n}}. \tag{2.3}$$

It has the properties $\mathbf{S}(\mathbf{x})^\top = -\mathbf{S}(\mathbf{x}) = \mathbf{S}(-\mathbf{x})$, and $\mathbf{S}(\mathbf{x})\mathbf{x} = \mathbf{0}$.

2.1.2 Earth Centered Inertial (ECI) Frame

The inertial frame $\mathcal{F}_i$ has its origin $\mathcal{O}_i$ in the center of the Earth, and it is denoted by $\mathcal{F}_i : \{\mathcal{O}_i; \hat{\mathbf{x}}_i, \hat{\mathbf{y}}_i, \hat{\mathbf{z}}_i\}$. The $\hat{\mathbf{x}}_i$-axis is pointing in the vernal equinox direction, the $\hat{\mathbf{y}}_i$-axis points 90°, spanning the equatorial plane together with the $\hat{\mathbf{x}}_i$-axis, and the $\hat{\mathbf{z}}_i$-axis points through the North Pole.

2.1.3 Earth-centered Earth-fixed (ECEF) Frame

The ECEF frame has its origin $\mathcal{O}_e$ fixed to the center of the Earth, and its axes rotate relative to $\mathcal{F}_\mathrm{i}$. The ECEF frame is denoted by $\mathcal{F}_e : \{\mathcal{O}_e; \hat{\mathbf{x}}_e, \hat{\mathbf{y}}_e, \hat{\mathbf{z}}_e\}$, where the $\hat{\mathbf{x}}_e$-axis spans the equatorial plane and is pointing through the prime meridian, the $\hat{\mathbf{y}}_e$-axis spans also the equatorial plane, and the $\hat{\mathbf{z}}_e$-axis points out the North Pole. $\mathcal{F}_e$ is necessary to monitor the objects on the ground.
The term longitude describes an angle that moves from east to west (from 180° in the east, 0° at the prime meridian, and 180° in the west). The term latitude describes a motion of 0° at the equator, extending to 90° at either pole. The angular velocity of $\mathcal{F}_e$ relative to $\mathcal{F}_i$ about the z-axis is $\boldsymbol{\omega}_{ie} = [0 \;\; 0 \;\; 7.2921]^\top \cdot 10^{-5}$ rad/s [19, p. 16].

2.1.4 Body Frame

The body frame has its origin $\mathcal{O}_b$ in the satellite's center of mass and is denoted as $\mathcal{F}_b : \{\mathcal{O}_b; \hat{\mathbf{x}}_b, \hat{\mathbf{y}}_b, \hat{\mathbf{z}}_b\}$, where the $\hat{\mathbf{x}}_b$-axis is the longitudinal axis, the $\hat{\mathbf{y}}_b$-axis is the transversal axis, and the $\hat{\mathbf{z}}_b$-axis is the normal axis. It is a moving coordinate frame that is defined by the principal axes of the satellite's body.
The satellite's inertial position $\mathbf{r}^i_{ib} \in \mathbb{R}^3$, velocity $\mathbf{v}^i_{ib} \in \mathbb{R}^3$, and acceleration $\mathbf{a}^i_{ib} \in \mathbb{R}^3$

are defined as

$$\mathbf{r}_{ib}^{i} = \mathbf{R}_{p}^{i}\mathbf{r}_{p}, \; \mathbf{v}_{ib}^{i} = \mathbf{R}_{p}^{i}\mathbf{v}_{p}, \quad \text{and } \mathbf{a}_{ib}^{i} = \frac{\mu}{\left(\left\|\mathbf{r}_{ib}^{i}\right\|_{2}\right)^{3}} \tag{2.4}$$

where $\mathbf{R}_{p}^{i}$ represents the rotation from the perifocal frame to the inertial frame. Detailed information on the perifocal frame is shown in Appendices B.2.1 and B.2.2.
The satellite's velocity expressed in $\mathcal{F}_{i}$ may be written as

$$\mathbf{v}_{\text{rel}}^{i} = \mathbf{v}_{ib}^{i} + \mathbf{S}\left(\boldsymbol{\omega}_{ie}\right)\mathbf{r}_{ib}^{i}. \tag{2.5}$$

2.1.5 Orbit Frame

The orbit frame follows the satellite's path as it orbits the Earth. It has its origin $\mathcal{O}_{o}$ in the satellite's center of gravity (CG), and it is denoted by $\mathcal{F}_{\text{o}} : \{\mathcal{O}_{o} = \mathcal{O}_{b}; \hat{\mathbf{x}}_{o}, \hat{\mathbf{y}}_{o}, \hat{\mathbf{z}}_{o}\}$, where the $\hat{\mathbf{x}}_{o}$-axis points in the direction of the orbit velocity vector, the $\hat{\mathbf{z}}_{o}$-axis points in the direction of the Earth's center of mass, and the $\hat{\mathbf{y}}_{o}$-axis completes the right-handed coordinate system. $\mathcal{F}_{o}$ is also known as Vehicle Velocity Local Horizontal (VVLH) frame. In [20], different orbit classifications are defined. There is a classification between Low Earth Orbit (LEO), Medium Earth Orbit (MEO), High Earth Orbit (HEO), geosynchronous orbits, sun-synchronous orbits, and critical inclination orbits [20, pp. 89-91]. Earth-observing satellites must be located near the Earth's surface to obtain a high image resolution. The satellite is assumed to orbiting the Earth at a low altitude. In LEO, the altitude is between 160 to 2000 km. When atmospheric drag effects are taken into account, the altitude is often greater than 300 km [20, p. 89].
The mean altitude of the HYPSO in $\mathcal{F}_{o}$ is denoted by h_{o} and given as 500 km. The right-hand unit vectors of the orbit frame $\hat{\mathbf{z}}_{o}$, $\hat{\mathbf{y}}_{o}$, and $\hat{\mathbf{x}}_{o}$ may be written as

$$\hat{\mathbf{z}}_{o} = -\frac{\mathbf{r}_{ib}^{i}}{\left\|\mathbf{r}_{ib}^{i}\right\|_{2}}, \; \hat{\mathbf{y}}_{o} = -\frac{\mathbf{r}_{ib}^{i} \times \mathbf{v}_{ib}^{i}}{\left\|\mathbf{r}_{ib}^{i} \times \mathbf{v}_{ib}^{i}\right\|_{2}}, \text{ and } \hat{\mathbf{x}}_{o} = \hat{\mathbf{y}}_{o} \times \hat{\mathbf{z}}_{o}. \tag{2.6}$$

Applying (2.3) to (2.6) gives $\hat{\mathbf{y}}_{o} = -\frac{\mathbf{S}(\mathbf{r}_{ib}^{i})\mathbf{v}_{ib}^{i}}{\left\|\mathbf{S}(\mathbf{r}_{ib}^{i})\mathbf{v}_{ib}^{i}\right\|_{2}}$, and $\hat{\mathbf{x}}_{o} = \mathbf{S}(\hat{\mathbf{y}}_{o})\hat{\mathbf{z}}_{o}$.
Appendix B.3 introduces the required parameters to calculate orbital mechanics.

Figure 2.1 illustrates the relation between inertial frame, body frame, and desired frame.

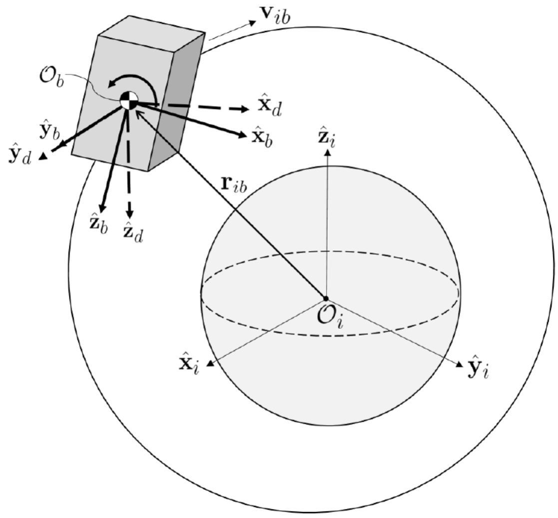

Figure 2.1. – Reference frames for the satellite
[21, p. 148120]

2.1.6 Wheel Frame

The wheel frame is denoted by $\mathcal{F}_w$. Each axis of $\mathcal{F}_w$ is fixed to the rotational axis of each reaction wheel, and the vectors in $\mathcal{F}_w$ have the same length as the number of reaction wheels in the satellite. For modeling, it is assumed that $\mathcal{F}_w$ and $\mathcal{F}_b$ do not rotate relative to each other.

2.2 Attitude Parameterizations

Commonly used sets of parameters for attitude representation are Euler angles, Euler parameters, and quaternions. The latter parameterization is applied for modeling in Chapter 3.

2.2.1 Euler Angles

Two sets of Euler angles are commonly used: the roll-pitch-yaw Euler angles and the classical Euler angles. In general, there exist three Euler angles: ϕ, θ, and ψ.
Figure 2.2 shows that a rotation can be characterized as a sequence of a roll rotation by an angle ϕ about the satellite's longitudinal axis, a pitch rotation by an angle θ about the lateral axis of the satellite, and a yaw rotation by an angle ψ about the satellite's vertical axis.

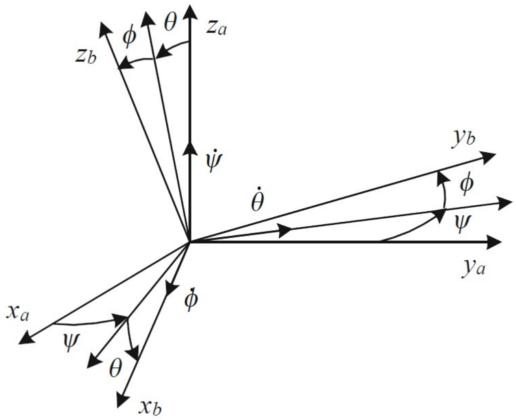

Figure 2.2. – Roll-pitch-yaw Euler angles
[22, p. 225]

The rotation matrix for the roll-pitch-yaw parameters is defined by

$$\mathbf{R}_b^a = \mathbf{R}_z(\psi)\mathbf{R}_y(\theta)\mathbf{R}_x(\phi). \tag{2.7}$$

Expressing the satellite's attitude and desired attitude in Euler angle parameterization gives

$$\mathbf{\Psi} = [\phi, \theta, \psi]^\top \text{ and } \mathbf{\Psi}_\mathrm{d} = [\phi_d, \theta_d, \psi_d]^\top. \tag{2.8}$$

The attitude error, parameterized by Euler angles, is defined as $\tilde{\boldsymbol{\Psi}} = \boldsymbol{\Psi} - \boldsymbol{\Psi}_d$.

2.2.2 Euler Parameters and Quaternions

Compared to the three Euler angles, Euler parameters use four variables to represent the satellite's attitude. This parameterization is more computationally efficient. The Euler parameters, consisting of a scalar part $\eta \in \mathbb{R}$ and a vector part $\boldsymbol{\epsilon} = [\epsilon_x, \epsilon_y, \epsilon_z]^\top \in \mathbb{R}^3$, are defined in terms of the angle-axis parameters by

$$\begin{aligned} \eta &= \cos\frac{\phi}{2} \\ \boldsymbol{\epsilon} &= \mathbf{k}\sin\frac{\phi}{2} \end{aligned} \tag{2.9}$$

where $\mathbf{k}$ is the principal axis and ϕ is the principal angle [23, p. 331].
The unit quaternion $\mathbf{q} \in \mathbb{R}^4$ is a four-dimensional vector which represents a rotation of $\mathcal{F}_b$ relative to $\mathcal{F}_o$. It is denoted by

$$\mathbf{q}_{ob} = \mathbf{q} = [\eta,\ \boldsymbol{\epsilon}^\top]^\top \tag{2.10}$$

satisfying the constraint $\mathbf{q}^\top\mathbf{q} = \eta^2 + \epsilon_x^2 + \epsilon_y^2 + \epsilon_z^2 = 1$ [19, p. 28]. This property is called the unit property, because the quaternion vector is confined to have a unit norm.
The desired quaternion in a reference frame $\mathcal{F}_d$ is defined as

$$\mathbf{q}_d = [\eta, \boldsymbol{\epsilon}_d^\top]^\top \tag{2.11}$$

and it also satisfies the condition $\mathbf{q}_d^\top\mathbf{q}_d = 1$. There always exists an inverse of a unit quaternion, identical to its conjugate [24, p. 49]. An inverse rotation [25, p. 779] can be performed by getting the inverse conjungated of $\mathbf{q}$ used as

$$\bar{\mathbf{q}} = [\eta, -\boldsymbol{\epsilon}^\top]^\top. \tag{2.12}$$

The quaternion inverse of $\mathbf{q}$ is defined as

$$\mathbf{q}^{-1} = \frac{\bar{\mathbf{q}}}{\|\mathbf{q}\|_2}. \tag{2.13}$$

Similarly, the quaternion inverse of $\mathbf{q}_d$ may be calculated as

$$\mathbf{q}_d^{-1} = \frac{[\eta_d,\ -\boldsymbol{\epsilon}_d^\top]^\top}{\|\mathbf{q}_d\|_2}. \tag{2.14}$$

When calculating the quaternion product of two unit quaternions, it gives a unit quaternion

$$\mathbf{q} = \mathbf{q}_1 \otimes \mathbf{q}_2 = \begin{bmatrix} \eta_1\eta_2 - \boldsymbol{\epsilon}_1^\top \boldsymbol{\epsilon}_2 \\ \eta_1\boldsymbol{\epsilon}_2 + \eta_2\boldsymbol{\epsilon}_1 + \mathbf{S}(\boldsymbol{\epsilon}_1)\boldsymbol{\epsilon}_2 \end{bmatrix} \qquad [22, \text{ p. } 234]. \tag{2.15}$$

The quaternion product is similar to a matrix multiplication, where the order of quaternion multiplication equals the order of matrix multiplication [24, p. 47]. The attitude error quaternion may be calculated by the quaternion product as

$$\tilde{\mathbf{q}} = \begin{bmatrix} \tilde{\eta} \\ \tilde{\boldsymbol{\epsilon}} \end{bmatrix} = \mathbf{q}_d^{-1} \otimes \mathbf{q} = \begin{bmatrix} \eta_d\eta + \boldsymbol{\epsilon}_d^\top \boldsymbol{\epsilon} \\ \eta_d\boldsymbol{\epsilon} - \eta\boldsymbol{\epsilon}_d - \mathbf{S}(\boldsymbol{\epsilon}_d)\boldsymbol{\epsilon} \end{bmatrix} \tag{2.16}$$

representing the rotation of $\mathcal{F}_b$ relative to $\mathcal{F}_d$ [26, p. 1150]. The attitude error quaternion also satisfies the condition $\tilde{\mathbf{q}}^\top \tilde{\mathbf{q}} = 1$ (unity property).

Using the four-component quaternion representation for modeling has the advantage that the model does not experience any singularities. The rotation matrix does not need trigonometric functions. Additionally, the model can be easily referenced to the coordinate system following the orbit [27, p. 1185].

Appendix A.3 specifies the transformation from quaternions to Euler angles.

2.3 Transformation between Frames

2.3.1 Rotation Matrix and its Properties

A rotation is simply a coordinate transformation. When determining the satellite's attitude, the rotation matrix, a proper orthogonal matrix that transforms vectors from a reference frame fixed in space to a frame fixed in the satellite's body [24, p. 40], needs to be estimated. The rotation matrix represents the physical attitude of the satellite's rigid body. It is denoted by $\mathbf{R}_a^b$, representing a rotation from a frame $\mathcal{F}_b$ to a frame $\mathcal{F}_a$. The rotation matrix is a 3×3 matrix with nine elements. Rotation matrices are members of the special orthogonal group of order three:

$$\mathbf{R} \in \mathrm{SO}(3),\ \mathrm{SO}(3) = \{\mathbf{R} \mid \mathbf{R} \in \mathbb{R}^{3\times 3}\ ,\ \mathbf{R}\mathbf{R}^\top = \mathbf{R}^\top\mathbf{R} = \mathbf{I} \text{ and } \det \mathbf{R} = 1\}. \quad (2.17)$$

This is called orthogonal property of the rotation matrix. Another property of the rotation matrix is $\mathbf{R}_a^b = \left(\mathbf{R}_b^a\right)^\top$ [22, p. 219].
A rotation matrix can consist of composite rotations. Then it is the product of the single rotation matrices. A rotation from a frame $\mathcal{F}_a$ to a frame $\mathcal{F}_c$ is the product of a rotation from $\mathcal{F}_\mathrm{a}$ to $\mathcal{F}_b$ and a rotation from $\mathcal{F}_b$ to $\mathcal{F}_c$: $\mathbf{R}_c^a = \mathbf{R}_b^a\mathbf{R}_c^b$ [22, p. 221]. In case of three rotations, the total rotation from $\mathcal{F}_a$ to $\mathcal{F}_d$ is represented by the rotation matrix $\mathbf{R}_d^a = \mathbf{R}_b^a\mathbf{R}_c^b\mathbf{R}_d^c$.
The angular velocity $\boldsymbol{\omega}$ represents the satellite's or reaction wheel's rotational motion relative to a fixed point, e.g., the origin of a reference frame. The rotation matrix $\mathbf{R}_a^b$ transforms the coordinate vector in frame $\mathcal{F}_a$ to the coordinate vector in frame $\mathcal{F}_b$ according to

$$\boldsymbol{\omega}_{ab}^b = \mathbf{R}_a^b\boldsymbol{\omega}_{ab}^a \quad (2.18)$$

where the equation $\mathbf{v}^{to} = \mathbf{R}_{from}^{to}\mathbf{v}^{from}$ [19, p. 20] has been applied.
An attitude maneuver transforms an initial attitude $\mathbf{R}_0 \in \mathrm{SO}(3)$ and an initial angular velocity to a terminal attitude $\mathbf{R}_f \in \mathrm{SO}(3)$ and a terminal angular velocity [28, p. 37].

2.3.2 Simple Rotations

A rotation can be described as a sequence of three simple rotations. Simple rotations are described in [22]. According to (2.7), the complete rotation, consisting of composite rotations, may be written as

$$\mathbf{R}_b^a = \mathbf{R}_z(\psi)\mathbf{R}_y(\theta)\mathbf{R}_x(\phi) \tag{2.19}$$

where matrix $\mathbf{R}_b^a$ becomes singular when $\theta = \pm\frac{\pi}{2}$ [29, p. 9]. This rotation matrix, parameterized by Euler angles, is also called direction cosine matrix (DCM). The rotation matrix $\mathbf{R}_b^a$ transforms a vector $\boldsymbol{\omega}_{ab}^b$ to a vector $\boldsymbol{\omega}_{ab}^a$ according to

$$\boldsymbol{\omega}_{ab}^a = \mathbf{R}_b^a \boldsymbol{\omega}_{ab}^b = \mathbf{R}_z(\psi)\mathbf{R}_y(\theta)\mathbf{R}_x(\phi)\boldsymbol{\omega}_{ab}^b. \tag{2.20}$$

First, there is a roll rotation by an angle ϕ about the $\hat{\mathbf{x}}$-axis as shown in Figure 2.3.

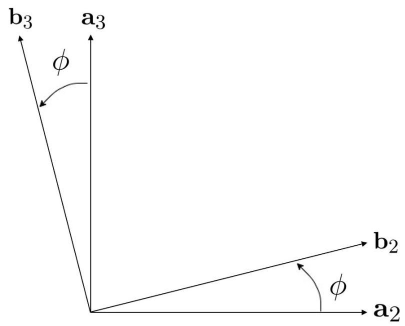

Figure 2.3. – Rotation by angle ϕ around $\mathbf{a}_1$

The rotation from a frame $\mathcal{F}_a$ with a right-handed set of three orthogonal unit vectors $\{\mathbf{a}_1\ \mathbf{a}_2\ \mathbf{a}_3\}$ to a frame $\mathcal{F}_\mathrm{b}$ with a right-handed set of three orthogonal unit vectors $\{\mathbf{b}_1\ \mathbf{b}_2\ \mathbf{b}_3\}$ [20, p. 323] is represented by the matrix calculating the vector products

$$\mathbf{R}_x(\phi) = \begin{bmatrix} \mathbf{a}_1\mathbf{b}_1 & \mathbf{a}_1\mathbf{b}_2 & \mathbf{a}_1\mathbf{b}_3 \\ \mathbf{a}_2\mathbf{b}_1 & \mathbf{a}_2\mathbf{b}_2 & \mathbf{a}_2\mathbf{b}_3 \\ \mathbf{a}_3\mathbf{b}_1 & \mathbf{a}_3\mathbf{b}_2 & \mathbf{a}_3\mathbf{b}_3 \end{bmatrix} = \begin{bmatrix} 1 & 0 & 0 \\ 0 & \cos\phi & -\sin\phi \\ 0 & \sin\phi & \cos\phi \end{bmatrix}.$$

The elements of $\mathbf{R}_y(\theta)$ and $\mathbf{R}_z(\psi)$ can be found in the same way. The second rotation is a pitch rotation by an angle θ about the $\hat{\mathbf{y}}$-axis, represented by the rotation matrix

$$\mathbf{R}_y(\theta) = \begin{bmatrix} \cos\theta & 0 & \sin\theta \\ 0 & 1 & 0 \\ -\sin\theta & 0 & \cos\theta \end{bmatrix}. \tag{2.21}$$

Third, there is a yaw rotation by an angle ψ about the $\hat{\mathbf{z}}$-axis, represented by the rotation matrix

$$\mathbf{R}_z(\psi) = \begin{bmatrix} \cos\psi & -\sin\psi & 0 \\ \sin\psi & \cos\psi & 0 \\ 0 & 0 & 1 \end{bmatrix}. \tag{2.22}$$

2.3.3 Rotation from $\mathcal{F}_b$ to $\mathcal{F}_o$

From the control perspective, the rotation between body frame with respect to the orbit frame is where the most interest arises [30, p. 2]. The rotation between $\mathcal{F}_b$ and $\mathcal{F}_o$ is denoted as

$$\mathbf{R}_o^b = \begin{bmatrix} \mathbf{c}_{o,1}^b & \mathbf{c}_{o,2}^b & \mathbf{c}_{o,3}^b \end{bmatrix}. \tag{2.23}$$

When the $\hat{\mathbf{z}}_b$-axis is aligned with the $\hat{\mathbf{z}}_o$-axis, the column vector $\mathbf{c}_{o,3}^b$ is equal to $[0 \;\; 0 \;\; 1]^\top$ [31, p. 262]. The rotation matrix $\mathbf{R}_o^b$ is defined as

$$\mathbf{R}_o^b = \mathbf{R}(\mathbf{q}) = \mathbf{I}_{3\times3} - 2\eta\mathbf{S}(\boldsymbol{\epsilon}) + \mathbf{S}^2(\boldsymbol{\epsilon}) \qquad [19, \text{ p. } 28] \tag{2.24}$$

$$= \begin{bmatrix} \eta^2 + \epsilon_x^2 - \epsilon_y^2 - \epsilon_z^2 & 2\epsilon_x\epsilon_y - 2\eta\epsilon_z & 2\epsilon_x\epsilon_z + 2\eta\epsilon_y \\ 2\epsilon_x\epsilon_y + 2\eta\epsilon_z & \eta^2 - \epsilon_x^2 + \epsilon_y^2 - \epsilon_z^2 & 2\epsilon_y\epsilon_z - 2\eta\epsilon_x \\ 2\epsilon_x\epsilon_z - 2\eta\epsilon_y & 2\epsilon_y\epsilon_z + 2\eta\epsilon_x & \eta^2 - \epsilon_x^2 - \epsilon_y^2 + \epsilon_z^2 \end{bmatrix}. \tag{2.25}$$

Rewriting (2.25) with respect to the unity property of quaternions gives

$$\mathbf{R}_o^b = \begin{bmatrix} 1 - 2\epsilon_y^2 - 2\epsilon_z^2 & 2\epsilon_x\epsilon_y - 2\eta\epsilon_z & 2\epsilon_x\epsilon_z + 2\eta\epsilon_y \\ 2\epsilon_x\epsilon_y + 2\eta\epsilon_z & 1 - 2\epsilon_x^2 - 2\epsilon_z^2 & 2\epsilon_y\epsilon_z - 2\eta\epsilon_x \\ 2\epsilon_x\epsilon_z - 2\eta\epsilon_y & 2\epsilon_y\epsilon_z + 2\eta\epsilon_x & 1 - 2\epsilon_x^2 - 2\epsilon_y^2 \end{bmatrix} \qquad [19, \text{ p. } 29]. \tag{2.26}$$

$\mathbf{R}_o^b$ is necessary to transform quaternions to Euler angles (see Appendix A.3). The angular velocity of $\mathcal{F}_b$ relative to $\mathcal{F}_o$, expressed in body coordinates, may be written as

$$\boldsymbol{\omega}_{ob}^b = \boldsymbol{\omega}_{ib}^b - \mathbf{R}_o^b\boldsymbol{\omega}_{io}^o \tag{2.27}$$

$$= \boldsymbol{\omega}_{ib}^b - \boldsymbol{\omega}_0\mathrm{c}_{o,1}^b \qquad [31, \text{ p. } 263] \tag{2.28}$$

where $\boldsymbol{\omega}_{io}^o$ is calculated in Appendix B.3 when introducing orbit mechanics and $\boldsymbol{\omega}_{ib}^b$ is obtained by taking the integral of (3.23), specified in Chapter 3.4.1.

2.3.4 Rotation from $\mathcal{F}_o$ to $\mathcal{F}_i$

From (2.6), the rotation matrices

$$\mathbf{R}_o^i = [\hat{\mathbf{x}}_o \; \hat{\mathbf{y}}_o \; \hat{\mathbf{z}}_o] \quad \text{and} \quad \mathbf{R}_i^o = \left(\mathbf{R}_o^i\right)^\top \tag{2.29}$$

result, where the unit vectors of $\mathcal{F}_o$ are defined in (2.6).

2.3.5 Rotation from $\mathcal{F}_b$ to $\mathcal{F}_d$

The rotation matrix in attitude error quaternion representation may be written as

$$\begin{aligned} \mathbf{R}_d^b &= \mathbf{R}(\tilde{\mathbf{q}}) = \mathbf{I}_{3\times3} - 2\tilde{\eta}\mathbf{S}(\tilde{\boldsymbol{\epsilon}}) + \mathbf{S}^2(\tilde{\boldsymbol{\epsilon}}) \\ &= \mathbf{R}(\mathbf{q})\mathbf{R}(\mathbf{q}_d)^\top = \mathbf{R}_o^b(\mathbf{R}_o^d)^\top \end{aligned} \tag{2.30}$$

where the rotation from $\mathcal{F}_o$ to $\mathcal{F}_d$ is given by

$$\mathbf{R}_o^d = \mathbf{R}(\mathbf{q}_d) = \mathbf{I}_{3\times3} - 2\eta_d\mathbf{S}(\boldsymbol{\epsilon}_d) + \mathbf{S}^2(\boldsymbol{\epsilon}_d). \tag{2.31}$$

In addition, the rotation from $\mathcal{F}_b$ to $\mathcal{F}_d$ is considered in the context of the error quaternion, specified in Chapter 3.4.2.
Appendices B.2.2 and B.2.3 introduce other rotations.

Chapter 3

Kinematics and Dynamical System Model

In this master's thesis, only rotational motions are considered. Kinematic and dynamic equations of rotational motion are not as simple as those for translational motion, which only represents the relation between position and velocity [24, p. 67], [29, p. 8]. Here, the system has three degrees of freedom: roll, pitch, and yaw. The spacecraft is equipped with more actuators than axes to control (r > n) [8, p. 1]. Thus, the rigid body is overactuated.

3.1 Kinematics

When setting up kinematic equations, aspects of motion are handled without considering forces and torques. Taking the time derivatives of the quaternion elements η and $\boldsymbol{\epsilon}$ gives

$$\begin{aligned} \dot{\eta} &= -\frac{1}{2}\boldsymbol{\epsilon}^{\top}\boldsymbol{\omega}_{ob}^{b} \\ \dot{\boldsymbol{\epsilon}} &= \frac{1}{2}[\eta\ \mathbf{I}_{3\times 3} + \mathbf{S}(\boldsymbol{\epsilon})]\boldsymbol{\omega}_{ob}^{b} \qquad \text{[29, p. 10].} \end{aligned} \tag{3.1}$$

In quaternion parameterization, the kinematic differential equation is defined as

$$\dot{\mathbf{q}} = \begin{bmatrix} \dot{\eta} \\ \dot{\boldsymbol{\epsilon}} \end{bmatrix} = \frac{1}{2}\mathbf{T}(\mathbf{q})\boldsymbol{\omega}_{ob}^{b} \tag{3.2}$$

where $\mathbf{T}(\mathbf{q})$ is the angular velocity transformation matrix, defined as

$$\mathbf{T}(\mathbf{q}) = \begin{bmatrix} -\boldsymbol{\epsilon}^\top \\ \eta \mathbf{I}_{3\times 3} + \mathbf{S}(\boldsymbol{\epsilon}) \end{bmatrix} \tag{3.3}$$

with the property $\mathbf{T}(\mathbf{q})^\top \mathbf{T}(\mathbf{q}) = \mathbf{I}_{3\times 3}$.
Similarly, the kinematic differential equation in terms of $\mathbf{q}_d$ may be calculated as

$$\dot{\mathbf{q}}_d = \begin{bmatrix} \dot{\eta}_d \\ \dot{\boldsymbol{\epsilon}}_d \end{bmatrix} = \frac{1}{2} \begin{bmatrix} -\boldsymbol{\epsilon}_d^\top \\ \eta_d \mathbf{I}_{3\times 3} + \mathbf{S}(\boldsymbol{\epsilon}_d) \end{bmatrix} \boldsymbol{\omega}_{ob,d}^b \tag{3.4}$$

and the kinematic differential equation in terms of $\tilde{\mathbf{q}}$ may be written as

$$\dot{\tilde{\mathbf{q}}} = \begin{bmatrix} \dot{\tilde{\eta}} \\ \dot{\tilde{\boldsymbol{\epsilon}}} \end{bmatrix} = \frac{1}{2} \begin{bmatrix} -\tilde{\boldsymbol{\epsilon}}^\top \\ \tilde{\eta} \mathbf{I}_{3\times 3} + \mathbf{S}(\tilde{\boldsymbol{\epsilon}}) \end{bmatrix} \tilde{\boldsymbol{\omega}}_{ob}^b \tag{3.5}$$

where $\tilde{\mathbf{q}}$ is the attitude error quaternion, defined in (2.16), and $\tilde{\boldsymbol{\omega}}_{ob}^b$ is the error angular velocity, which is defined as

$$\tilde{\boldsymbol{\omega}}_{ob}^b = \boldsymbol{\omega}_{ob}^b - \boldsymbol{\omega}_{ob,d}^b = \boldsymbol{\omega}_{ib}^b - \mathbf{R}_o^b \boldsymbol{\omega}_{io}^o - \boldsymbol{\omega}_{ob,d}^b. \tag{3.6}$$

Because of the orthogonal property of the rotation matrix, specified in (2.17), the rotational kinematic equation in terms of the rotation matrix may be written as

$$\dot{\mathbf{R}}_a^b = \mathbf{S}\left(\boldsymbol{\omega}_{ab}^a\right) \mathbf{R}_a^b = \mathbf{R}_b^a \mathbf{S}\left(\boldsymbol{\omega}_{ab}^b\right). \tag{3.7}$$

Differentiating the angular velocity $\boldsymbol{\omega}_{ab}^b$ in (2.18) with respect to time gives

$$\dot{\boldsymbol{\omega}}_{ab}^b = \dot{\mathbf{R}}_a^b \boldsymbol{\omega}_{ab}^a + \mathbf{R}_a^b \dot{\boldsymbol{\omega}}_{ab}^a. \tag{3.8}$$

3.2 Characteristics of HYPSO

The HYPSO is based on the CubeSat concept. Therefore, there exist technically challenging restrictions in size and mass. It has a dimension of $0.2 \times 0.1 \times 0.3$ m^3 in width, depth, and height. The satellite's mass is approximately 6.8 kg and has a surface area of 0.06 m^2. The central components of the satellite's ADCS are four reaction wheels, three magnetorquers, fine sun-sensors, a gyroscope, magnetometers, GPS, and star-tracker. The first three components listed are actuators that cause the satellite to rotate around its center of mass as desired. The other components are sensors detecting the current attitude of the satellite.

The non-symmetric inertia matrix of the rigid body $\mathbf{J} \in \mathbb{R}^{\mathrm{n}\times\mathrm{n}}$ is defined as

$$\mathbf{J} = \begin{bmatrix} \mathrm{J}_{xx} & \mathrm{J}_{xy} & \mathrm{J}_{xz} \\ \mathrm{J}_{yx} & \mathrm{J}_{yy} & \mathrm{J}_{yz} \\ \mathrm{J}_{zx} & \mathrm{J}_{zy} & \mathrm{J}_{zz} \end{bmatrix}, \ \mathbf{J} = \mathbf{J}^\top > 0. \tag{3.9}$$

The elements of the $\mathbf{J}$ matrix and other physical parameters of the HYPSO are listed in Table 3.1.

physical parameter	**definition**
max. exposed surface area	$\mathrm{A} = 0.06\ \mathrm{m}^2$
moment of inertia about $\hat{\mathbf{x}}_b$-axis	$\mathrm{J}_{xx} = 0.0775\ \mathrm{kgm}^2$
moment of inertia about $\hat{\mathbf{y}}_b$-axis	$\mathrm{J}_{yy} = 0.1067\ \mathrm{kgm}^2$
moment of inertia about $\hat{\mathbf{z}}_b$-axis	$\mathrm{J}_{zz} = 0.0389\ \mathrm{kgm}^2$
products of inertia	$\mathrm{J}_{xy} = \mathrm{J}_{yx} = -0.0005\ \mathrm{kgm}^2$
	$\mathrm{J}_{yz} = \mathrm{J}_{zy} = -0.0002\ \mathrm{kgm}^2$
	$\mathrm{J}_{zx} = \mathrm{J}_{xz} = 0.0002\ \mathrm{kgm}^2$
drag coefficient	$\mathrm{C_d} = 2$
residual dipole of the satellite	$\mathrm{m}^b = 0.0125$

Table 3.1. – Physical parameters of the HYPSO

3.3 Environmental Disturbance Model

The satellite's environment and actuators can cause external forces and torques. They act on the satellite as it orbits the Earth. Modeling the perturbations such as orbital dynamics and the Earth and sun disturbances is necessary to obtain the required model accuracy. Orbital perturbations depend on the orbit type and altitude chosen [32, p. 150]. The disturbance torques are typically smaller than the near-maximum reaction wheel torque deployed during rotation [27, p. 1189]. It is assumed that the wheel friction can be neglected.

3.3.1 Gravity Gradient Torque

In a low orbit, the satellite does not experience the same force on all its body parts. The gravitational force makes the satellite rotate towards the Earth with respect to the principal axis of inertia [25, p. 780]. The torque generated due to the gravity gradient $\boldsymbol{\tau}_{\mathrm{gg}}^b \in \mathbb{R}^{\mathrm{n}}$ is defined as

$$\begin{aligned} \boldsymbol{\tau}_{\mathrm{gg}}^b &= 3\frac{\mu}{\left(\left\|\mathbf{r}_{ib}^i\right\|_2\right)^3}\mathbf{S}(\mathbf{c}_{o,3}^b)\mathbf{J}\mathbf{c}_{o,3}^b \\ &= 3\left(\boldsymbol{\omega}_0\right)^2\mathbf{S}(\mathbf{c}_{o,3}^b)\mathbf{J}\mathbf{c}_{o,3}^b \end{aligned} \tag{3.10}$$

where $\mathbf{c}_{o,3}^b = \mathbf{R}_o^b[0 \quad 0 \quad 1]^\top$ and $\mathbf{J}$ is the non-symmetric inertia matrix of the rigid body as given in (3.9).

3.3.2 Atmospheric Drag Torque

Aerodynamic forces in near-Earth orbit lead to dragging and thus reducing the altitude over time [25, p. 780]. The force acting on the satellite due to atmospheric drag can be written as

$$\mathbf{f}_{\mathrm{drag}}^b = -\frac{1}{2}\rho_{\mathrm{atm}}\mathrm{A}_{\mathrm{drag}}\left\|\mathbf{v}_{\mathrm{rel}}^b\right\|_2^2\mathrm{C}_{\mathrm{d}} \tag{3.11}$$

where the atmospheric density ρ_{atm} is $1.7741 \cdot 10^{-12}$ kg/m^3, $\mathrm{A}_{\mathrm{drag}}$ is the maximum exposed surface area of the satellite, and C_{d} is the drag coefficient. $\mathbf{v}_{\mathrm{rel}}^b$ is the satellite's velocity expressed in body coordinates and it is defined as

$$\mathbf{v}_{\mathrm{rel}}^b = \mathbf{R}_o^b\mathbf{R}_i^o\mathbf{v}_{\mathrm{rel}}^i \tag{3.12}$$

where $\mathbf{v}^i_{\text{rel}}$ has been specified in (2.5). Thus, the aerodynamic torque $\boldsymbol{\tau}^b_{\text{atm}} \in \mathbb{R}^{\text{n}}$ can be written as

$$\boldsymbol{\tau}^b_{\text{atm}} = \mathbf{f}^b_{\text{drag}}(\mathbf{c}_{\text{pa}} - \mathbf{c}_{\text{g}}) \tag{3.13}$$

where $\mathbf{c}_{\text{g}}$ is the center of gravity, given as

$$\mathbf{c}_{\text{g}} = [-0.0009 \quad 0.0006 \quad -0.0433]^\top$$

and $\mathbf{c}_{\text{pa}}$ is the aerodynamic center of pressure, defined as

$$\mathbf{c}_{\text{pa}} = \begin{bmatrix} \frac{\text{w}}{2} & -\frac{\text{w}}{2} & -0.001 & -0.001 & -0.001 & 0.001 \\ 0.001 & 0.001 & \frac{\text{d}}{2} & -\frac{\text{d}}{2} & 0.001 & -0.001 \\ 0.02 & 0.02 & 0.02 & 0.02 & \frac{\text{h}}{2} & -\frac{\text{h}}{2} \end{bmatrix}$$

where w, d, and h are the spacecraft's dimensions defined in Chapter 3.2.

3.3.3 Magnetic Torque

A residual magnetic dipole that interacts with the Earth's magnetic field is generated by the electronic devices inside the satellite. The torque due to the magnetic dipole, denoted by $\boldsymbol{\tau}^b_{\text{m}} \in \mathbb{R}^{\text{n}}$, is defined as

$$\boldsymbol{\tau}^b_{\text{m}} = \mathbf{D} \times \mathbf{B}^b \tag{3.14}$$

where $\mathbf{D}$ is the residual dipole of the satellite and $\mathbf{B}^b$ is the Earth's magnetic field. $\mathbf{D}$ may be calculated as

$$\mathbf{D} = \text{m}^b \begin{bmatrix} -\frac{0.5}{\sqrt{3}} & \frac{1.4}{\sqrt{3}} & -\frac{2.5}{\sqrt{3}} \end{bmatrix}^\top \tag{3.15}$$

Remark: The Earth's magnetic field, expressed in body coordinates, is modeled using the International Geomagnetic Reference Field (IGRF) model. The Matlab/Simulink implementation shows the detailed calculation. The magnetic field vector is necessary for calculating the external disturbance torque due to the magnetic dipole and the momentum dumping torque in Chapter 3.6.1.

3.3.4 Solar Radiation Torque

The force acting on the satellite due to solar radiation pressure is calculated as

$$\mathbf{f}^b_{\mathrm{srp}} = \frac{\mathrm{F_{srp}}}{\mathrm{c}} \frac{\mathrm{A_{srp}}}{2} (1+\eta) \cos\alpha \begin{bmatrix} \frac{1}{\sqrt{2}} \\ \frac{1}{\sqrt{2}} \\ 0 \end{bmatrix} \tag{3.16}$$

where $\mathrm{F_{srp}}$ is the solar constant, given as 1367 W/m^2, c is the speed of light in vacuum, given as $2.9979 \cdot 10^8$ m/s, and $\mathrm{A_{srp}}$ is the maximum exposed surface area of the satellite. The angle of incidence of the sun is given as $\alpha = 0\,°$ and the emittance η is 0.2. Radiation and particles from the sun generate a perturbation torque $\boldsymbol{\tau}^b_{\mathrm{srp}} \in \mathbb{R}^{\mathrm{n}}$, which is defined as

$$\boldsymbol{\tau}^b_{\mathrm{srp}} = \mathbf{f}^b_{\mathrm{srp}}(\mathbf{c}_{\mathrm{srp}} - \mathbf{c}_{\mathrm{g}}) \tag{3.17}$$

where $\mathbf{c}_{\mathrm{srp}}$ is the center of solar pressure and $\mathbf{c}_{\mathrm{g}}$ is the center of gravity. Both are calculated similarly to (3.13).

3.3.5 Total External Torque Acting on the Satellite

The sum of environmental torques $\boldsymbol{\tau}^b_{\mathrm{ext}} \in \mathbb{R}^{\mathrm{n}}$, expressed in body coordinates, can be written as

$$\boldsymbol{\tau}^b_{\mathrm{ext}} = \boldsymbol{\tau}^b_{\mathrm{m}} + \boldsymbol{\tau}^b_{\mathrm{gg}} + \boldsymbol{\tau}^b_{\mathrm{drag}} + \boldsymbol{\tau}^b_{\mathrm{srp}}(+\boldsymbol{\tau}^b_{\mathrm{noise}}). \tag{3.18}$$

Chapter 5.2.2.1 considers noise on the measurement of the attitude, parameterized by quaternions, and of the angular velocities.
The total external perturbing force acting on the satellite is the sum of the single perturbing forces: $\mathbf{f}^b_{\mathrm{ext}} = \mathbf{f}^b_{\mathrm{drag}} + \mathbf{f}^b_{\mathrm{srp}}$.

3.4 Rigid Body Dynamics and Nonlinear State Space Model

3.4.1 Rigid Body Dynamics

The Newton-Euler equations of motion are applied to build the dynamical model of the satellite. The dynamical model describes the relationship between applied torque and angular momentum in a rigid body. A non-symmetric inertia matrix is used for the dynamic spacecraft model. The inertia matrix of the spacecraft and its reaction wheels may be calculated as

$$\bar{\mathbf{J}} = \mathbf{J} + \mathbf{A}\mathbf{J}_{\mathrm{s}}\mathbf{A}^{\top} \tag{3.19}$$

where $\mathbf{J}$ is defined in (3.9) and $\mathbf{J}_{\mathrm{s}}$ is defined in (3.27). The total angular momentum, expressed in $\mathcal{F}_b$, may be written as

$$\mathbf{h}^b = \mathbf{J}\boldsymbol{\omega}_{ib}^b + \mathbf{h}_{\mathrm{s}}^b \quad [24]. \tag{3.20}$$

The total torque acting on the satellite $\boldsymbol{\tau}^b \in \mathbb{R}^3$ can be described as the sum of actuator torques and disturbance torques. Taking the time derivative of (3.20) gives

$$\frac{\mathrm{d}^b}{\mathrm{dt}}\mathbf{h}^b = \mathbf{S}(\boldsymbol{\omega}_{ib}^b)\bar{\mathbf{J}}\boldsymbol{\omega}_{ib}^b + \mathbf{S}(\boldsymbol{\omega}_{ib}^b)\mathbf{J}_{\mathrm{s}}\boldsymbol{\omega}_{\mathrm{s}}^b + \boldsymbol{\tau}_{\mathrm{ext}}^b \tag{3.21}$$

and

$$\begin{aligned}\mathbf{J}\dot{\boldsymbol{\omega}}_{ib}^b &= -\mathbf{S}(\boldsymbol{\omega}_{ib}^b)\mathbf{J}\boldsymbol{\omega}_{ib}^b + \boldsymbol{\tau}_{\mathrm{act}}^b + \boldsymbol{\tau}_{\mathrm{ext}}^b \\ &= -\mathbf{S}(\boldsymbol{\omega}_{ib}^b)\mathbf{h}^b - \boldsymbol{\tau}_{\mathrm{s}}^b + \boldsymbol{\tau}_{\mathrm{mtq}}^b + \boldsymbol{\tau}_{\mathrm{ext}}^b\end{aligned} \tag{3.22}$$

where

$$\begin{aligned}\dot{\boldsymbol{\omega}}_{ib}^b &= \bar{\mathbf{J}}^{-1}\left[-\mathbf{S}(\boldsymbol{\omega}_{ib}^b)(\bar{\mathbf{J}}\boldsymbol{\omega}_{ib}^b + \mathbf{A}\mathbf{J}_{\mathrm{s}}\boldsymbol{\omega}_{\mathrm{s}}^w) - \boldsymbol{\tau}_{\mathrm{u}}^b + \boldsymbol{\tau}_{\mathrm{mtq}}^b + \boldsymbol{\tau}_{\mathrm{ext}}^b\right] \\ &= \bar{\mathbf{J}}^{-1}\left[-\mathbf{S}(\boldsymbol{\omega}_{ib}^b)(\bar{\mathbf{J}}\boldsymbol{\omega}_{ib}^b + \mathbf{A}\mathbf{J}_{\mathrm{s}}\boldsymbol{\omega}_{\mathrm{s}}^w) - \mathbf{A}\mathbf{J}_{\mathrm{s}}\dot{\boldsymbol{\omega}}_{\mathrm{s}}^w + \boldsymbol{\tau}_{\mathrm{mtq}}^b + \boldsymbol{\tau}_{\mathrm{ext}}^b\right].\end{aligned} \tag{3.23}$$

3.4.2 CL Error Dynamics

Differentiating (3.6) with respect to time gives the angular velocity error dynamics:

$$\begin{aligned}\dot{\tilde{\boldsymbol{\omega}}}_{ob}^b &= \dot{\boldsymbol{\omega}}_{ib}^b - \mathbf{R}_d^b\dot{\boldsymbol{\omega}}_{id}^d - \dot{\mathbf{R}}_d^b\boldsymbol{\omega}_{id}^d \\ &= \dot{\boldsymbol{\omega}}_{ib}^b - \dot{\boldsymbol{\omega}}_{id}^b + \mathbf{S}(\tilde{\boldsymbol{\omega}}_{ob}^b)\boldsymbol{\omega}_{id}^b\end{aligned} \tag{3.24}$$

where

$$\dot{\boldsymbol{\omega}}_{id}^{b} = \mathbf{R}_{d}^{b}\dot{\boldsymbol{\omega}}_{ob}^{d} + \mathbf{R}_{o}^{b}\dot{\boldsymbol{\omega}}_{io}^{o} - \mathbf{S}(\boldsymbol{\omega}_{od}^{b})\mathbf{R}_{o}^{b}\boldsymbol{\omega}_{io}^{o}. \tag{3.25}$$

There is a comparison between the two vectors representing the current attitude and the desired attitude. The attitude error represents the difference between attitude estimation and the true value [23, p. 331]. The attitude error quaternion is calculated in (2.16).

In [33], the choice of equilibrium points for attitude stabilization is specified. The attitude error quaternion has the two equilibrium points

1. positive equilibrium point: $\tilde{\mathbf{q}}_{+} = [+1 \;\; 0 \;\; 0 \;\; 0]^{\top}$ is chosen if $\tilde{\eta} \geq 0$, and
2. negative equilibrium point: $\tilde{\mathbf{q}}_{-} = [-1 \;\; 0 \;\; 0 \;\; 0]^{\top}$ is chosen if $\tilde{\eta} < 0$ [34, p. 2785].

The vector $\tilde{\mathbf{q}}_{+}$ corresponds to the rotation $\tilde{\Phi} = 0\,^{\circ}$ around one arbitrary axis and $\tilde{\mathbf{q}}_{-}$ corresponds to the rotation $\tilde{\Phi} = 360\,^{\circ}$ around one arbitrary axis. The physical attitude of $\mathbf{q}_{+}$ and $\mathbf{q}_{-}$ is the same, but it is mathematically different because of a rotation of 2π around one arbitrary axis [33, p. 3].

The equilibrium points are taken into account when investigating stability properties in Chapter 3.8.1.

3.4.3 Nonlinear State Space Model

The nonlinear state space model can be written as

$$\dot{\mathbf{x}} = \begin{bmatrix} \dot{\eta} \\ \dot{\boldsymbol{\epsilon}} \\ \dot{\boldsymbol{\omega}}_{ib}^{b} \\ \dot{\boldsymbol{\omega}}_{\mathrm{s}}^{w} \end{bmatrix} = \begin{bmatrix} -\frac{1}{2}\boldsymbol{\epsilon}^{\top}\boldsymbol{\omega}_{ib}^{b} \\ \frac{1}{2}\left[\eta\mathbf{I}_{3\times 3} + \mathbf{S}(\epsilon)\right] \\ \bar{\mathbf{J}}^{-1}\left[\mathbf{S}(\boldsymbol{\omega}_{ib}^{b})\bar{\mathbf{J}}\boldsymbol{\omega}_{ib}^{b} + \mathbf{S}(\boldsymbol{\omega}_{ib}^{b})\mathbf{A}\mathbf{J}_{\mathrm{s}}\boldsymbol{\omega}_{\mathrm{s}}^{w} - \mathbf{A}\mathbf{J}_{\mathrm{s}}\dot{\boldsymbol{\omega}}_{\mathrm{s}}^{w} + \boldsymbol{\tau}_{\mathrm{mtq}}^{b} + \boldsymbol{\tau}_{\mathrm{ext}}^{b}\right] \\ \mathbf{J}_{\mathrm{s}}^{-1}\left[\boldsymbol{\tau}_{\mathrm{s}}^{w} - \mathbf{J}_{\mathrm{s}}\mathbf{A}^{\top}\dot{\boldsymbol{\omega}}_{ib}^{b}\right] \end{bmatrix} \tag{3.26}$$

by combining the differential equations derived in Chapters 3.1, 3.4.1, and 3.5.4.

3.5 Reaction Wheel Characteristics and Dynamics

3.5.1 Reaction Wheel Characteristics

The satellite consists of a rigid structure and has spinning reaction wheels inside. A rigid body combined with rotating wheels is commonly denoted as a gyrostat. Wheels complete with motor and drive electronics are often referred to as reaction wheel assemblies (RWAs). The satellite's attitude can be varied by adjusting the speed or orientation of its internal gyrostats [35, p. 544]. Reaction wheels must maintain the desired attitude of the satellite. For modeling, identical reaction wheels are assumed. Reaction wheels operate by accelerating a wheel in one direction, forcing the satellite to rotate in the other direction [25, p. 778]. Reaction wheels are spinning about a fixed axis of inertial symmetry, such that the total amount of inertia can be assumed constant in $\mathcal{F}_b$ [29, p. 11]. A reaction wheel can be described as a torque providing motor with relatively high rotor inertia. The HYPSO is equipped with reaction wheels from the manufacturer NanoAvionics. The physical parameters of the RWA are listed in Table 3.2.

physical parameter	**definition**
motor inductance	$\mathrm{L_a} = 0.0005$ H
motor resistivity	$\mathrm{R_a} = 6.67\ \Omega$
motor torque constant	$\mathrm{K_t} = 0.00588$
back electromotive constant	$\mathrm{K_e} = 0.00589$ Vs/rad
constant DC Voltage of RW	$\mathrm{V_a} = 5$ V
Motor viscous friction coefficient	$\mathrm{b_{motor}} = 6 \cdot 10^{-7}$ Nms/rad
moment of inertia of the motor	$\mathrm{I_s} = 2.2984 \cdot 10^{-5}$ kgm^2

Table 3.2. – Physical parameters of the RWA

The axial reaction wheel inertia matrix $\mathbf{J}_\mathrm{s} \in \mathbb{R}^{\mathrm{r}\times\mathrm{r}}$ is defined as a diagonal matrix containing the wheel axial inertias. It may be written as

$$\mathbf{J}_\mathrm{s} = \mathrm{I_s}\mathbf{I}_{4\times4},\ \mathbf{J}_\mathrm{s} = \mathrm{I_{s,j}} \text{ for } \mathrm{j} = \{1,2,3,4\} \tag{3.27}$$

This actuator is often also referred to as momentum wheel. The amount of torque provided depends on the size of the rotor and motor, usually in a range from 0.01 Nm to 1 Nm [36, p. 3283]. The range for the maximum angular momentum produced by the reaction wheel is between 2 to 250 Nms and for the maximum rotational speeds between $1,000$ to $6,000$ rpm [24, p. 148]. The reaction wheel characteristics, including the saturation bounds defined by the manufacturer, can be found in Table 3.3.

criteria	**definition**
single reaction wheel	
dimensions	$43.5 \times 43.5 \times 24$ mm^3
weight	137 g
moment of inertia	$\mathrm{I_s} = 2.29 \cdot 10^{-5}$ kgm^2
jitter variance	$3.1657 \cdot 10^{-4}$ rad/s
max. acceleration	$\dot{\boldsymbol{\omega}}^w_{\mathrm{s,max}} = 4500$ rad/s^2
max. speed	$\boldsymbol{\omega}^w_{\mathrm{s,max}} = 6500$ rpm
steady state	$\boldsymbol{\omega}^w_{\mathrm{s}} = 1000$ rpm each RW
max. torque	$\boldsymbol{\tau}^w_{\mathrm{s,max}} = 3.2 \cdot 10^{-3}$ Nm
max. momentum storage	$\mathrm{h}^w_{\mathrm{s,max}} = 20 \cdot 10^{-3}$ Nms
power consumption (idle)	$\mathrm{P_s} = 45 \cdot 10^{-3}$ W
power consumption (steady-state)	$\mathrm{P_s} = 150 \cdot 10^{-3}$ W
reaction wheel assembly (RWA)	
dimensions	$92.5 \times 92.5 \times 51.3$ mm^3
weight	760 g
max. torque around $\hat{\mathbf{x}}_b$-axis	$\boldsymbol{\tau}^w_{\mathrm{s,max_x}} = 5.9 \cdot 10^{-3}$ Nm
max. torque around $\hat{\mathbf{y}}_b$-axis	$\boldsymbol{\tau}^w_{\mathrm{s,max_y}} = 5.9 \cdot 10^{-3}$ Nm
max. torque around $\hat{\mathbf{z}}_b$-axis	$\boldsymbol{\tau}^w_{\mathrm{s,max_z}} = 2.5 \cdot 10^{-3}$ Nm
max. momentum storage around $\hat{\mathbf{x}}_b$-axis	$\mathbf{h}^w_{\mathrm{s,max_x}} = 37 \cdot 10^{-3}$ Nms
max. momentum storage around $\hat{\mathbf{y}}_b$-axis	$\mathbf{h}^w_{\mathrm{s,max_y}} = 37 \cdot 10^{-3}$ Nms
max. momentum storage around $\hat{\mathbf{z}}_b$-axis	$\mathbf{h}^w_{\mathrm{s,max_z}} = 15.6 \cdot 10^{-3}$ Nms
power consumption (idle)	$\mathrm{P_s} = 180 \cdot 10^{-3}$ W
power consumption (steady-state)	$\mathrm{P_s} = 600 \cdot 10^{-3}$ W

Table 3.3. – Reaction wheel specifications given by the manufacturer NanoAvionics

3.5.2 RWA Distribution Matrix

The reaction wheel assembly distribution matrix $\mathbf{A} \in \mathbb{R}^{\mathrm{n}\times\mathrm{r}}$, $\mathbf{A} : \mathbb{R}^{\mathrm{r}} \to \mathbb{R}^{\mathrm{n}}$ represents the transformation from $\mathcal{F}_w$ to $\mathcal{F}_b$. The matrix $\mathbf{A}$ may be written as

$$\mathbf{A} = [\mathbf{a}_1 \; \mathbf{a}_2 \; \dots \; \mathbf{a}_\mathrm{r}] \tag{3.28}$$

where the column vectors $\mathbf{a}_\mathrm{j} \in \mathbb{R}^\mathrm{n}$ for $\mathrm{j} = \{1, 2, \dots, \mathrm{r}\}$ specify the direction of the wheel's rotation axes. The number of columns in the RWA distribution matrix is equal to the number of reaction wheels.
Three reaction wheels along each axis are required to ensure full three-axis control. RWAs usually consist of more than three wheels for redundancy and performance [36, p. 3283]. One possible reaction wheel configuration is the tetrahedron structure, as shown in Figure 3.1.

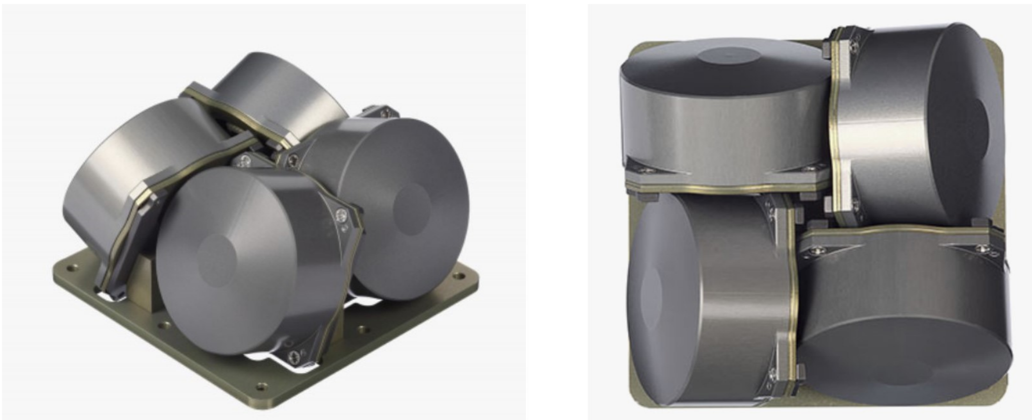

Figure 3.1. – Four reaction wheels in a tetrahedron configuration (NanoAvionics)

For the tetrahedron configuration, the matrix $\mathbf{A}$ is defined as

$$\mathbf{A} = \begin{bmatrix} \mathrm{a} & -\mathrm{a} & 0 & 0 \\ \mathrm{b} & \mathrm{b} & \mathrm{c} & \mathrm{c} \\ 0 & 0 & \mathrm{d} & -\mathrm{d} \end{bmatrix}, \text{ where } \mathrm{a}^2 + \mathrm{b}^2 = \mathrm{c}^2 + \mathrm{d}^2 = 1 \quad [24, \text{p. } 154]. \tag{3.29}$$

Because of the RWA configuration described, the matrix elements are $\mathrm{a} = \mathrm{c} = \sqrt{\frac{2}{3}}$ and $\mathrm{b} = \mathrm{d} = \sqrt{\frac{1}{3}}$.

Due to space limitations, a different RWA configuration is applied to the HYPSO as shown in Figure 3.2. The RWA configuration consists of three orthogonally placed reaction wheels with respect to each $\mathcal{F}_b$-axis, and a fourth reaction wheel has the spin axis inclined 54.7 ° with respect to each $\mathcal{F}_b$-axis [21, p. 14823].

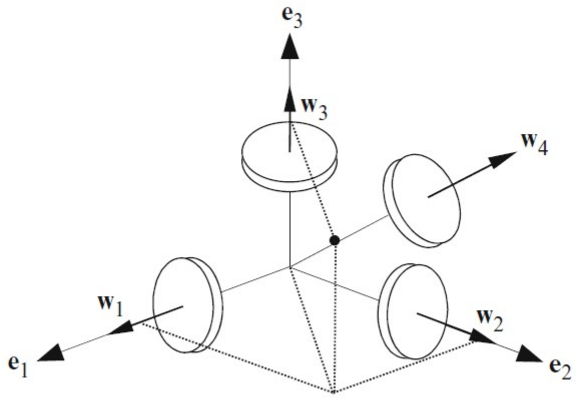

Figure 3.2. – NASA standard RWA configuration [24, p. 155]

The matrix $\mathbf{A}$ is defined as

$$\mathbf{A} = \begin{bmatrix} 1 & 0 & 0 & \alpha \\ 0 & 1 & 0 & \beta \\ 0 & 0 & 1 & \gamma \end{bmatrix}, \text{ where } \alpha^2 + \beta^2 + \gamma^2 = 1 \quad [24, \text{pp. 154-155}] \tag{3.30}$$

for the RWA configuration applied to the HYPSO. Due to the RWA configuration described, the matrix elements are $\alpha = \beta = \gamma = \dfrac{1}{\sqrt{3}}$.

3.5.3 Pseudoinverse Matrix for Different RWA Configurations

The pseudoinverse matrix for the tetrahedron RWA configuration (3.29) is defined by

$$\mathbf{A}^{+} = \frac{1}{2}\begin{bmatrix} \frac{1}{\mathrm{a}} & \frac{\mathrm{b}}{(\mathrm{b}^2+\mathrm{c}^2)} & 0 \\ -\frac{1}{\mathrm{a}} & \frac{\mathrm{b}}{(\mathrm{b}^2+\mathrm{c}^2)} & 0 \\ 0 & \frac{\mathrm{c}}{(\mathrm{b}^2+\mathrm{c}^2)} & \frac{1}{\mathrm{d}} \\ 0 & \frac{\mathrm{c}}{(\mathrm{b}^2+\mathrm{c}^2)} & -\frac{1}{\mathrm{d}} \end{bmatrix} \quad [24,\ \text{p. } 156]. \tag{3.31}$$

The pseudoinverse matrix is defined as

$$\mathbf{A}^{+} = \frac{1}{2}\begin{bmatrix} 1+\beta^2+\gamma^2 & -\alpha\beta & -\alpha\gamma \\ -\alpha\beta & 1+\alpha^2+\gamma^2 & -\beta\gamma \\ -\alpha\gamma & -\beta\gamma & 1+\alpha^2+\beta^2 \\ \alpha & \beta & \gamma \end{bmatrix} \quad [24,\ \text{p. } 157] \tag{3.32}$$

for the NASA standard RWA configuration applied to the HYPSO (3.30).

Remark: The pseudoinverse matrices (3.31) and (3.32) are very specific for the RWA configurations described. Chapter 4.4.2 introduces the generalized inverse matrix used for control allocation.

3.5.4 Reaction Wheel Dynamics

When setting up dynamic equations, variables like angular momentum and torque are of particular interest. The axial angular momentum vector of the reaction wheels $\mathbf{h}_{\mathrm{s}}^{b} \in \mathbb{R}^{\mathrm{r}}$ is defined as

$$\begin{aligned} \mathbf{h}_{\mathrm{s}}^{b} &= \mathbf{A}\mathbf{J}_{\mathrm{s}}\boldsymbol{\omega}_{\mathrm{s}}^{w} + \mathbf{J}_{\mathrm{s}}\mathbf{A}^{\top}\boldsymbol{\omega}_{ib}^{b} \\ &= \mathbf{J}_{\mathrm{s}}\boldsymbol{\omega}_{\mathrm{s}}^{b} + \mathbf{J}_{\mathrm{s}}\mathbf{A}^{\top}\boldsymbol{\omega}_{ib}^{b}. \end{aligned} \tag{3.33}$$

The error in the RWA's angular momentum is defined as

$$\tilde{\mathbf{h}}_{\mathrm{s}}^{b} = \mathbf{A}\mathbf{J}_{\mathrm{s}}\left(\boldsymbol{\omega}_{\mathrm{s}}^{w} - \boldsymbol{\omega}_{\mathrm{s},d}^{w}\right) = \mathbf{J}_{\mathrm{s}}\left(\boldsymbol{\omega}_{\mathrm{s}}^{b} - \boldsymbol{\omega}_{\mathrm{s},d}^{b}\right). \tag{3.34}$$

The axial acceleration of the RWA is defined as

$$\dot{\boldsymbol{\omega}}_{\mathrm{s}}^{w} = \mathbf{J}_{\mathrm{s}}^{-1}\mathbf{A}^{+}\boldsymbol{\tau}_{\mathrm{u}}^{b} - \mathbf{A}^{\top}\dot{\boldsymbol{\omega}}_{ib}^{b} \tag{3.35}$$

where $\mathbf{J}_{\mathrm{s}}^{-1} \in \mathbb{R}^{\mathrm{r}\times\mathrm{r}}$ is the inverse of the reaction wheel inertia matrix defined in (3.27), $\boldsymbol{\tau}_{\mathrm{u}}^{b}$ is the control input vector generated by the PD feedback controller defined in (3.46), and $\dot{\boldsymbol{\omega}}_{ib}^{b}$ is defined in (3.23).
The torque generated by the reaction wheels is given by

$$\boldsymbol{\tau}_{\mathrm{s}}^{w} = \mathbf{J}_{\mathrm{s}}\dot{\boldsymbol{\omega}}_{\mathrm{s}}^{w}. \tag{3.36}$$

Expressing the RW torque and angular momentum with respect to $\mathcal{F}_b$ gives

$$\boldsymbol{\tau}_{\mathrm{s}}^{w} = \mathbf{A}^{+}\left[\tau_{\mathrm{s},1}^{b}\ \tau_{\mathrm{s},2}^{b}\ \tau_{\mathrm{s},3}^{b}\ \tau_{\mathrm{s},4}^{b}\right]^{\top} + \mathbf{n} \tag{3.37}$$

and

$$\mathbf{h}_{\mathrm{s}}^{w} = \mathbf{A}^{+}\left[\mathrm{h}_{\mathrm{s},1}^{b}\ \mathrm{h}_{\mathrm{s},2}^{b}\ \mathrm{h}_{\mathrm{s},3}^{b}\ \mathrm{h}_{\mathrm{s},4}^{b}\right]^{\top} + \mathbf{n} \tag{3.38}$$

where $\mathbf{n} \in \mathbb{R}^{\mathrm{r}} \mid \mathbf{n} \in \mathcal{N}(\mathbf{A})$ is a vector in the nullspace of the RWA distribution matrix. Rewriting (3.37) gives the $\mathcal{L}_2$-norm

$$\begin{aligned} \|\boldsymbol{\tau}_{\mathrm{s}}^{w}\|_2 &= \left\|\mathbf{A}^{\top}\left(\mathbf{A}\mathbf{A}^{\top}\right)^{-1}\boldsymbol{\tau}_{\mathrm{s}}^{b}\right\|_2 + 2\left(\boldsymbol{\tau}_{\mathrm{s}}^{b}\right)^{\top}\left(\mathbf{A}\mathbf{A}^{\top}\right)^{-1}\mathbf{A}\mathbf{n} + \|\mathbf{n}\|_2 \\ &= \left(\boldsymbol{\tau}_{\mathrm{s}}^{b}\right)^{\top}\left(\mathbf{A}\mathbf{A}^{\top}\right)^{-1}\boldsymbol{\tau}_{\mathrm{s}}^{b} + \|\mathbf{n}\|_2\,. \end{aligned} \tag{3.39}$$

Setting $\mathbf{n} = 0$ minimizes $\|\boldsymbol{\tau}_{\mathrm{s}}^{w}\|_2$. The $\mathcal{L}_2$-norm of the angular momentum can be calculated similarly. The pseudoinverse matrix represents an $\mathcal{L}_2$-algorithm, because the $\mathcal{L}_2$-norm of the vector consisting of the single reaction wheel momenta is minimized [37, p. 1607].

3.6 Magnetorquer Characteristics and Dynamics

3.6.1 Magnetorquer Characteristics

The magnetorquer helps to stabilize the rotational speed of the reaction wheels [38, p. 527]. Magnetorquers are used for momentum unloading and desaturation of the reaction wheel assembly [38, p. 525]. Table 3.4 shows the magnetorquer characteristics, including the saturation bounds defined by the manufacturer NanoAvionics.

criteria	**definition**
mass	31 g
dimensions	R5.5 × 83.9 mm
max. dipole magnetic moment strength	$\mathrm{m}^b = 0.42\ \mathrm{Am}^2$
max. MTQ moment around $\hat{\mathbf{x}}_b$-axis	$\mathrm{m}_x^b = 0.84\ \mathrm{Am}^2$
max. MTQ moment around $\hat{\mathbf{y}}_b$-axis	$\mathrm{m}_x^b = 0.42\ \mathrm{Am}^2$
max. MTQ moment around $\hat{\mathbf{z}}_b$-axis	$\mathrm{m}_x^b = 0.42\ \mathrm{Am}^2$
power consumption	$\mathrm{P}_{\mathrm{mtq}} = 0.86\ \mathrm{W}$

Table 3.4. – Magnetorquer specification given by the manufacturer NanoAvionics

3.6.2 Magnetorquer Dynamics

3.6.2.1 Detumbling Torque

Magnetorquers perform detumbling to slow and stabilize the angular velocity of the satellite while acting on the Earth's magnetic field. The torque generated by the magnetorquer may be calculated as

$$\boldsymbol{\tau}^b_{\mathrm{mtq}} = \mathbf{m}^b \times \mathbf{B}^b \tag{3.40}$$

where $\mathbf{m}^b$ is the magnetic dipole moment generated by coils and $\mathbf{B}^b = [\mathrm{B}^b_x \ \ \mathrm{B}^b_y \ \ \mathrm{B}^b_z]^\top$ is the local geomagnetic field vector. $\mathbf{m}^b$ may be written as

$$\mathbf{m}^b = -\mathrm{k}\dot{\mathbf{B}}^b. \tag{3.41}$$

For simplification, [31] assumes that the time derivative of the magnetic field in $\mathcal{F}_i$ is approximately zero in the polar regions [31, p. 264]. Taking the time derivative of $\mathbf{B}^b$ gives

$$\begin{aligned} \dot{\mathbf{B}}^b &= \dot{\mathbf{R}}_i^b \mathbf{B}^i + \mathbf{R}_i^b \dot{\mathbf{B}}^i \\ &= \mathbf{B}^b \times \boldsymbol{\omega}_{ib}^b + \mathbf{R}_i^b \dot{\mathbf{B}}^i \\ &= -\mathbf{S}(\boldsymbol{\omega}_{ib}^b)\mathbf{B}^b \qquad \text{[31, p. 264].} \end{aligned} \tag{3.42}$$

3.6.2.2 Momentum Dumping Torque

The momentum dumping torque may be calculated as

$$\boldsymbol{\tau}_{\mathrm{md}}^b = \frac{\mathrm{k_m}}{\|\mathbf{B}^b\|_2} \mathbf{S}(\tilde{\mathbf{h}}_{\mathrm{s}}^b) \frac{\mathbf{B}^b}{\|\mathbf{B}^b\|_2} \tag{3.43}$$

where $\tilde{\mathbf{h}}_{\mathrm{s}}^b$ is the error in the angular momentum for the reaction wheels as calculated in (3.34) and $\mathrm{k_m} > 0 \in \mathbb{R}$ is a desaturation control gain.

3.7 Proportional-Derivative Feedback Controller

The attitude maneuver is based on a PD feedback controller (quaternion-based control). Figure 3.3 shows a simplified control loop used in [21]. The PD controller uses feedback from $\tilde{\mathbf{q}}$ and $\tilde{\boldsymbol{\omega}}^b_{ob}$. The trajectory is given by the continuous angular velocity from $\mathcal{F}_d$ to $\mathcal{F}_o$, expressed in body coordinates, denoted by $\boldsymbol{\omega}^b_{od}$.

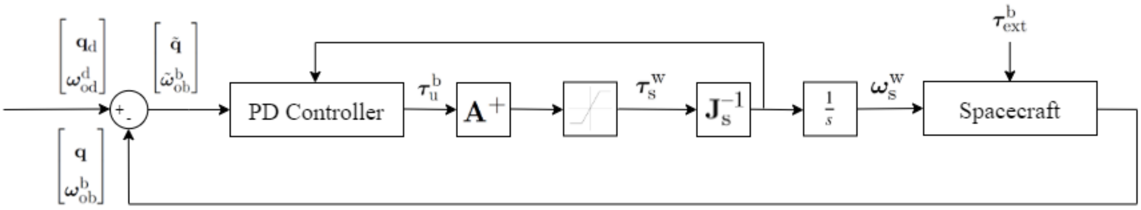

Figure 3.3. – Spacecraft and RWA closed loop control system

The control law is defined by

$$\boldsymbol{\tau}^b_u = -\mathrm{K_p}\mathrm{sgn}(\tilde{\eta})\tilde{\boldsymbol{\epsilon}} - \mathrm{K_d}\tilde{\boldsymbol{\omega}}^b_{ob} \text{ for pointing and} \tag{3.44}$$

$$\boldsymbol{\tau}^b_u = -\mathrm{K_p}\mathrm{sgn}(\tilde{\eta}(\mathrm{t}))\tilde{\boldsymbol{\epsilon}}(\mathrm{t}) - \mathrm{K_p}\tilde{\boldsymbol{\omega}}^b_{ob}(\mathrm{t}) \text{ for slewing, where} \tag{3.45}$$

$$\mathrm{sgn}(\tilde{\eta}(\mathrm{t})) = \begin{cases} 1 \text{ when } \tilde{\eta} \geq 0 \quad \forall\ \mathrm{t} \geq 0 \\ -1 \text{ when } \tilde{\eta} < 0 \quad \forall\ \mathrm{t} \geq 0 \end{cases} \text{ and}$$

$$\mathrm{K_p}, \mathrm{K_d} > 0 \in \mathbb{R} \text{ are the controller gains.}$$

The signum term implies a discontinuous controller. See [2] for an in-depth treatment.

3.8 Concepts of Stability and Convergence

3.8.1 Control Problem

After modeling, it is necessary to validate the model concerning the existence and uniqueness of solutions. It is necessary to check if the model meets the desired system behavior specifications and if the closed-loop (CL) system dynamics behave well. There exist two types of control problems: the regulation problem and the tracking problem. For the regulation problem, the reference state is constant. Here, the origin $\mathbf{x}_{\mathrm{ref}} = \mathbf{x}_0$ is the equilibrium point to be stabilized. The desired CL system behavior is fulfilled if $\mathrm{f}(\mathrm{t}, \mathbf{x}_{\mathrm{ref}}) = 0$, $\lim_{\mathrm{t}\to\infty} \mathbf{x}(\mathrm{t}) = \mathbf{x}_{\mathrm{ref}}$, and the system stays close to the equilibrium point if it starts close to it.
This is an asymptotic stabilization problem, where it is required to find a control law such that $\mathbf{x}_{\mathrm{ref}}$ is an asymptotically stable equilibrium point of $\dot{\mathbf{x}} = \mathbf{f}(\mathrm{t}, \mathbf{x})$. In other words, the origin should be an asymptotically stable equilibrium point of the system written in error coordinates. The state error $\mathbf{e} = \mathbf{x} - \mathbf{x}_{\mathrm{ref}} = 0$ should be an asymptotically stable equilibrium point of the CL error dynamics

$$\begin{aligned} \dot{\mathbf{e}} &= \dot{\mathbf{x}} - \dot{\mathbf{x}}_{\mathrm{ref}} = \dot{\mathbf{x}} = \mathrm{f}(\mathrm{t}, \mathbf{x}) \\ &= \mathbf{f}(\mathrm{t}, \mathrm{e} + \mathbf{x}_{\mathrm{ref}}) \end{aligned} \tag{3.46}$$

For the tracking problem, a time-varying reference state is given and the system state should follow the trajectory. The desired CL system behavior is fulfilled if the system converges to the trajectory. The Lyapunov stability property says that the system stays close to the trajectory if it starts close to the trajectory. It also leads to an asymptotic stabilization problem, where it is required to find a control law such that $\mathbf{e} = \mathbf{x} - \mathbf{x}_{\mathrm{ref}}(\mathrm{t}) = 0$ is an asymptotically stable equilibrium point of the CL error dynamics

$$\begin{aligned} \dot{\mathbf{e}} &= \dot{\mathbf{x}} - \dot{\mathbf{x}}_{\mathrm{ref}}(\mathrm{t}) \\ &= \mathbf{f}(\mathrm{t}, \mathrm{e} + \mathbf{x}_{\mathrm{ref}}, \mathrm{u}) - \dot{\mathbf{x}}_{\mathrm{ref}}(\mathrm{t}) \end{aligned} \tag{3.47}$$

3.8.2 Stability Theory

The characterization of a solution being stable, unstable, attractive, (locally) asymptotically stable, (locally) exponentially stable, globally stable, or globally asymptotically stable is specified in [19, p. 532] and [39, pp. 8-10]. In [40, pp. 16-24], geometrical and

algebraic criteria for stability are introduced.
The stability analysis based on Lyapunov's Theorems concentrates on the stability of critical points [39, p. 6]. When considering time-invariant systems of the form $\dot{\mathbf{x}} = \mathbf{f}(\mathbf{x})$, $\mathbf{f}$ is assumed to be locally Lipschitz. It guarantees a unique solution locally, and not the existence of a unique solution globally. Together with additional conditions in the Lyapunov Theorems, the local Lipschitz condition guarantees the global existence of a unique solution.
Another method to analyze Lyapunov stability properties is Lyapunov's indirect method which is often referred to as Lyapunov's linearization method. Using Lyapunov's indirect method, it is impossible to determine whether $\mathbf{x}_0$ is globally asymptotically or globally exponentially stable.
In [31], the kinetic energy is used for stability studies. A possible Lyapunov function candidate (LFC) is the satellite's kinetic energy. The kinetic energy of the HYPSO may be defined as

$$\mathrm{E}_{\mathrm{kin}} = \frac{1}{2}\left(\boldsymbol{\omega}_{ib}^{b}\right)^{\top}\mathbf{J}\boldsymbol{\omega}_{ib}^{b} + \left(\boldsymbol{\omega}_{ib}^{b}\right)^{\top}\mathbf{A}\mathbf{J}_{\mathrm{s}}\boldsymbol{\omega}_{\mathrm{s}}^{w} + \frac{1}{2}\left(\boldsymbol{\omega}_{\mathrm{s}}^{w}\right)^{\top}\mathbf{J}_{\mathrm{s}}\boldsymbol{\omega}_{\mathrm{s}}^{w}. \tag{3.48}$$

Based on Lyapunov's stability theory, [41] and [42] also discuss details about the stabilization of angular velocity.

Chapter 4

Control Allocation

4.1 Control Allocation Concept

The CA problem is distributing a desired total control effort among a redundant set of actuators. The actuators are referred to as the control surfaces available on the spacecraft. Figure 4.1 shows that CA generates virtual control commands $\mathbf{v}(\mathrm{t})$ and transfers and allocates them to the satellite's control surfaces [7, p. 343]. CA has to calculate a control input $\mathbf{u}(\mathrm{t})$ that ensures that the commanded virtual control commands $\mathbf{v}(\mathrm{t})$ are generated by all actuators cooperatively [7, p. 343]. The CA problem is formulated in terms of $\mathbf{v} \in \mathbb{R}^{\mathrm{n}}$, and the solution is then mapped to $\mathbf{u} \in \mathbb{R}^{\mathrm{r}}$ by CA [18, p. 138].

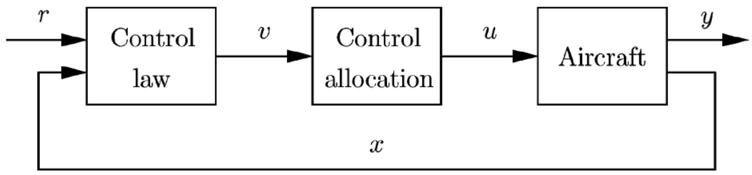

Figure 4.1. – Control allocation scheme
[13, p. 1029]

The constrained linear mapping problem

$$\mathbf{v}(\mathrm{t}) = \mathbf{B}\mathbf{u}(\mathrm{t}) \tag{4.1}$$

represents the CA problem. Matrix $\mathbf{B} \in \mathbb{R}^{\mathrm{n} \times \mathrm{r}}$ is called the control effectiveness matrix, representing the actuator effectiveness in generating moments. It is assumed that the actuators are linear in their effectiveness. For $\mathbf{B}$, the negative RWA distribution matrix $\mathbf{A}$ is used, representing the physical geometry of the reaction wheels. The highest priority is on providing the virtual control command in (4.1).
The main objective of CA is error minimization [11, p. 704]. Defining the virtual control error to be minimized gives

$$\tilde{\mathbf{e}} = \mathbf{B}\mathbf{u}(\mathrm{t}) - \mathbf{v}(\mathrm{t}). \tag{4.2}$$

The control error to be minimized for the original spacecraft model is defined by

$$\tilde{\mathbf{e}} = -\mathbf{A}\boldsymbol{\tau}_{\mathrm{s}}^{w} - \boldsymbol{\tau}_{\mathrm{u}}^{b} \tag{4.3}$$

where $\boldsymbol{\tau}_{\mathrm{u}}^{b} = -\mathbf{A}\boldsymbol{\tau}_{\mathrm{s}}^{w}$ is equivalent to (4.1).

4.2 Control Constraints

Here, a constrained CA problem is handled because control constraints are taken into account.

4.2.1 Definition of Control Constraints

The actual control vector $\mathbf{u}$ has to consider the following position and rate constraints:

$$\mathbf{u}_{\mathrm{min}} \leq \mathbf{u} \leq \mathbf{u}_{\mathrm{max}} \ , \ |\dot{\mathbf{u}}| \leq \mathbf{u}_{\mathrm{rate}} \qquad \text{[9, p. 2].} \tag{4.4}$$

Transforming the rate constraint in (4.4) into position limits gives

$$\underline{\mathbf{u}}(\mathrm{t}) \leq \mathbf{u} \leq \bar{\mathbf{u}}(\mathrm{t}) \qquad \text{[13, p. 1029].} \tag{4.5}$$

Note that (4.4) and (4.5) are meant component-wise.
The upper and lower bounds are defined by

$$\bar{\mathbf{u}}(\mathrm{t}) = \max[\mathbf{u}_{\mathrm{min}} \ , \ \mathbf{u}(\mathrm{t}-\mathrm{T}) - \mathbf{u}_{\mathrm{rate}}\mathrm{T}] \tag{4.6}$$

$$\underline{\mathbf{u}}(\mathrm{t}) = \min[\mathbf{u}_{\mathrm{max}} \ , \ \mathbf{u}(\mathrm{t}-\mathrm{T}) + \mathbf{u}_{\mathrm{rate}}\mathrm{T}] \qquad \text{[9, p. 2]} \tag{4.7}$$

where T is the sampling time.

4.2.2 Attainable, Admissible, and Feasible Controls

As mentioned in Chapter 3, more than three independent actuators are in use. In general, there is an infinite number of solutions to the CA problem. Most of these solutions are not realistic due to control limits resulting from the actuator's physical geometry [43, p. 1].
A set of attainable controls can be generated given the actuator's physical limits. The attainable controls $\mathbf{v} \in \mathbb{R}^{\mathrm{n}}$ are constrained to

$$\boldsymbol{\Omega}_{\mathrm{v}} = \{\mathbf{v} \in \mathbb{R}^{\mathrm{n}} \mid \mathbf{v} = \mathbf{B}\mathbf{u}, \ \mathbf{u} \in \Omega_{\mathrm{u}}\} \subset \mathbb{R}^{\mathrm{n}} \tag{4.8}$$

where $\boldsymbol{\Omega}_{\mathrm{u}}$ is the subset of admissible controls:

$$\mathbf{u} \in \Omega_{\mathrm{u}}, \ \Omega_{\mathrm{u}} = \{\mathbf{u} \in \mathbb{R}^{\mathrm{r}} \mid \mathbf{u}_{\mathrm{min}} \leq \mathbf{u} \leq \mathbf{u}_{\mathrm{max}}\} \subset \mathbb{R}^{\mathrm{r}}. \tag{4.9}$$

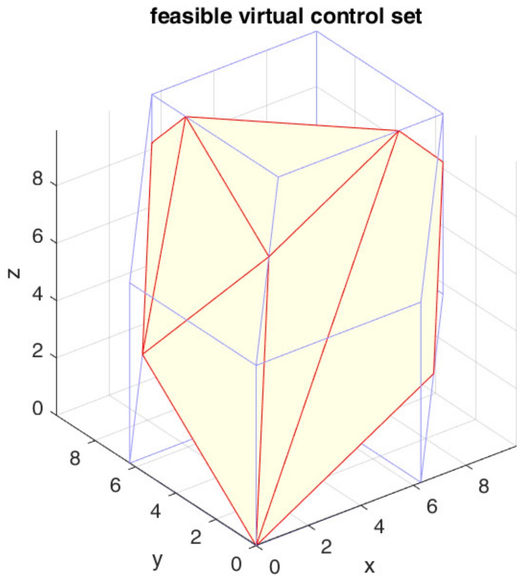

Figure 4.2. – Feasible virtual control set for position limits 0 ° and 360 °

The values of $\mathbf{u} \in \mathbb{R}^{\mathrm{r}}$ satisfying the constraints are feasible. If a feasible solution exists, at least one optimal solution exists. The values of $\mathbf{u} \in \mathbb{R}^{\mathrm{r}}$ that do not satisfy the constraints are referred to as infeasible. For the minimum position limit 0 ° and maximum position limit 360 °, the feasible virtual control set is shown in Figure 4.2, where the red (inner) set is the feasible virtual control set with linear allocation according to (4.8) and the blue (outer) set is the feasible virtual control set with constrained allocation according to (4.9).
Unattainable controls are moments that are impossible to achieve such that no valid solution exists [43, p. 1]. When the control law requests a desired moment outside the attainable moment subset, unattainable moments occur [43, p. 2]. Unattainable moments can lead to inadmissible control solutions [43, p. 5]. Thus, incorporating actuator limits and providing an admissible control solution is required [43, p. 1]. Inadmissible controls occur, especially during fast and aggressive maneuvers where all actuator capabilities are utilized and exceeded. There exist two ways to deal with inadmissible control solutions. On the one hand, scaling the control vector such that no element exceeds the limit is possible. On the other hand, prioritization of primary and secondary objectives is possible.

4.3 Failure of Actuators

4.3.1 Actuator Saturation

In the context of CA, it is important to consider the physical limitations of the reaction wheels like saturation, tear, or wear. In case a reaction wheel is saturated, it may need a higher amount of torque than available [44, p. 3]. Rewriting (4.1) gives

$$\mathbf{v} = \mathbf{B}\ \mathrm{sat}(\mathbf{u}) \tag{4.10}$$

where the saturation function is defined by

$$\mathrm{sat}(\mathbf{u}) = \begin{cases} \mathbf{u} & \text{if } \ |\mathbf{u}| < \mathbf{u}_{\max} \\ \mathrm{sgn}(\mathbf{u}) & \text{if } \ |\mathbf{u}| \geq \mathbf{u}_{\max} \end{cases} \qquad \text{[19, p. 250].} \tag{4.11}$$

As shown in Figure 4.3, the actuator is not able to produce any higher output signal when the control input exceeds the actuator limit, and the current control input is constant, equal to the maximum. Such an input saturation makes the closed-loop system nonlinear.

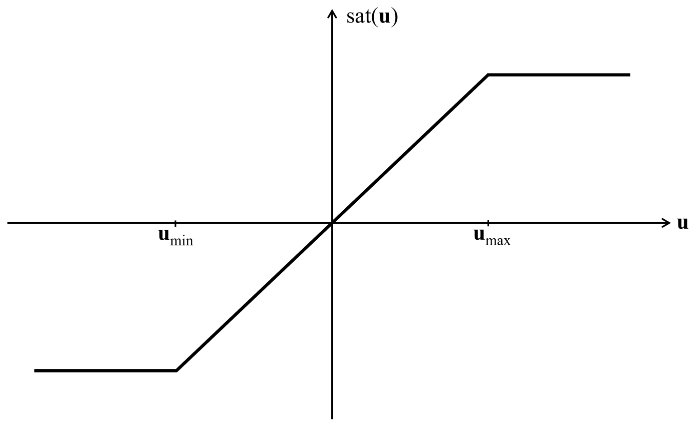

Figure 4.3. – Saturation function for an actuator

The saturation function does not depend on the input's history, so the nonlinearity is memoryless and has no dynamics. A linear system cannot approximate the saturation function because its time derivative is not defined in the two points $\mathbf{u}_{\min}$ and $\mathbf{u}_{\max}$.

Such nonlinearities can generate limit cycles, which are a specific type of oscillation. A limit cycle is a stable periodic solution, and it has the characteristic

$$\exists\ \mathrm{T} > 0 \text{ such that } \mathbf{x}(\mathrm{t}+\mathrm{T}) = \mathbf{x}(\mathrm{t})\ \forall \mathrm{t} \geq 0. \tag{4.12}$$

Another notable characteristic is that limit cycles occur without external periodic input (e.g., compare linear systems perturbed by a sinusoidal input signal).

4.3.2 Fault-Tolerant Control

When considering actuator dysfunctions, fault-tolerant control (FTC) also is of importance. A fault can have undesirable effects on the system operation, e.g., degrading the system function. Dysfunctions can be noticed when actuators are not performing their desired function. FTC intends to compensate or eliminate the negative effects of faults on the system and to ensure that the system remains in a safe state under fault conditions. Active FTC needs to maintain minimum stability requirements when actuators experience loss of control effectiveness. A particular type of fault is lock-in-place. This type of fault usually occurs, for example, due to a structural blockage that prevents the actuator from moving. The lock-in-place fault results in unwanted negative moments that deflect the aircraft from its desired trajectory [7, p. 343].

4.4 Controllability

4.4.1 Generalized Inverse Matrix

Appendix A.1.2 introduces the invertibility feature of a matrix. In CA, the generalized inverse of the control effectiveness matrix $\mathbf{B}$ needs to be calculated. If matrix $\mathbf{B}$ is right invertible, the right inverse of $\mathbf{B}$ is

$$\mathbf{B}^{+} = \mathbf{B}^{\top}\left(\mathbf{B}\mathbf{B}^{\top}\right)^{-1} \qquad \text{[45, p. 398]} \tag{4.13}$$

and if matrix $\mathbf{B}$ is left invertible, the left inverse is

$$\mathbf{B}^{+} = \left(\mathbf{B}^{\top}\mathbf{B}\right)^{-1}\mathbf{B}^{\top} \qquad \text{[45, p. 398].} \tag{4.14}$$

The matrix $\mathbf{B}^{+}$ is often referred to as Moore-Penrose inverse matrix [46, p. 1]. In the context of CA, the matrix $\mathbf{B}^{+}$ is calculated as in (4.13) when $\mathrm{rk}(\mathbf{B}) = \mathrm{n}$.
According to [45, p. 397], the matrix $\mathbf{B}$ satisfies the following conditions:

- $\mathbf{B}\mathbf{B}^{+}\mathbf{B} = \mathbf{B}$,
- $\mathbf{B}^{+}\mathbf{B}\mathbf{B}^{+} = \mathbf{B}^{+}$,
- $\left(\mathbf{B}\mathbf{B}^{+}\right)^{\top} = \mathbf{B}\mathbf{B}^{+}$, and
- $\left(\mathbf{B}^{+}\mathbf{B}\right)^{\top} = \mathbf{B}^{+}\mathbf{B}$.

Another type of generalized inverse beyond the Moore-Penrose inverse is the Drazin generalized inverse [45, pp. 401-403]. This type of matrix is not a common one in the literature reviewed on CA in Chapter 1.2.2.

4.4.2 Full Controllability and No Full Controllability

A differentiation is made between the cases with full controllability and no full controllability for the simulation of different attitude cases. The difference is particularly the rank of the system, as defined in Appendix A.1.1. In the case of full controllability, control effectiveness matrix $\mathbf{B}$ has a full rank and affects all three axes. Full controllability is given when the system is fully controllable since it is rank n. If there is no full controllability, not all three axes can be affected by matrix $\mathbf{B}$.

4.5 Dynamic Control Allocation

4.5.1 Formulation of the CA Problem

Given a set of feasible control inputs

$$\Omega_{\mathrm{u}} = \underset{\underline{\mathrm{u}}(\mathrm{t}) \leq \mathrm{u}(\mathrm{t}) \leq \bar{\mathrm{u}}(\mathrm{t})}{\operatorname{argmin}} \{ \| \mathbf{W}_{\mathrm{v}} \left[\mathbf{B}\mathbf{u}(\mathrm{t}) - \mathbf{v}(\mathrm{t}) \right] \|_2 \} \qquad [13, \text{ p. } 1029] \tag{4.15}$$

which minimizes the virtual control error $\mathbf{Bu}(\mathrm{t}) - \mathbf{v}(\mathrm{t})$, weighted by $\mathbf{W}_{\mathrm{v}}$, pick the control input which minimizes the cost function

$$\mathbf{u}(\mathrm{t}) = \underset{\mathbf{u}(\mathrm{t})}{\operatorname{argmin}} \{ \| \mathbf{W}_1 (\mathbf{u}(\mathrm{t}) - \mathbf{u}_d(\mathrm{t})) \|_2^2 + \| \mathbf{W}_2 (\mathbf{u}(\mathrm{t}) - \mathbf{u}(\mathrm{t} - \mathrm{T})) \|_2^2 \} \tag{4.16}$$

and it has to be solved under the equality constraint (4.1).
$\mathbf{W}_{\mathrm{v}} \in \mathbb{R}^{\mathrm{n} \times \mathrm{n}}$ is a weight matrix, affecting the prioritization among $\mathbf{v}(\mathrm{t})$. $\mathbf{W}_1 \in \mathbb{R}^{\mathrm{r} \times \mathrm{r}}$ and $\mathbf{W}_2 \in \mathbb{R}^{\mathrm{r} \times \mathrm{r}}$ are referred to as control position and control rate weighting matrices. $\mathbf{W}_1$ and $\mathbf{W}_2$ are assumed to be symmetric [13, p. 1029]. Thus, the combined weight matrix

$$\mathbf{W} = \left(\mathbf{W}_1^2 + \mathbf{W}_2^2 \right)^{\frac{1}{2}} \tag{4.17}$$

is non-singular [13, p. 1029]. The matrix $\mathbf{W}$ determines which actuators should be used primarily. The tradeoff between $\mathbf{W}_1$ and $\mathbf{W}_2$ is characterized by having a large $\mathbf{W}_1$ that induces fast convergence to desired actuator positions and a large $\mathbf{W}_2$ that prevents actuators from moving too fast [13, p. 1029].

4.5.2 Solution of the CA Problem

According to the first Theorem in [13], the explicit solution of the problem specified in (4.16) is given by

$$\mathbf{u}(\mathrm{t}) = \mathbf{E}\mathbf{u}_d(\mathrm{t}) + \underbrace{\mathbf{F}\mathbf{u}(\mathrm{t} - \mathrm{T})}_{\text{dynamic part}} + \mathbf{G}\mathbf{v}(\mathrm{t}) \qquad [13, \text{ p. } 1030] \tag{4.18}$$

where

$$
\begin{aligned}
\mathbf{G} &= \mathbf{W}^{-1}\left(\mathbf{B}\mathbf{W}^{-1}\right)^{+}\ ,\ \mathbf{G} \in \mathbb{R}^{\mathrm{r}\times\mathrm{n}} && (4.19)\\
\mathbf{E} &= (\mathbf{I}_{\mathrm{r}\times\mathrm{r}} - \mathbf{G}\mathbf{B})\mathbf{W}^{-2}\mathbf{W}_1^2\ ,\ \mathbf{E} \in \mathbb{R}^{\mathrm{r}\times\mathrm{r}} && (4.20)\\
\mathbf{F} &= (\mathbf{I}_{\mathrm{r}\times\mathrm{r}} - \mathbf{G}\mathbf{B})\mathbf{W}^{-2}\mathbf{W}_2^2\ ,\ \mathbf{F} \in \mathbb{R}^{\mathrm{r}\times\mathrm{r}}. && (4.21)
\end{aligned}
$$

It is important to note that $\mathbf{W}_2$ is not a $\mathbf{0}_{\mathrm{r}\times\mathrm{r}}$ matrix when calculating $\mathbf{F}$. Otherwise, a static control distribution is determined by omitting the dynamic part in (4.18). According to the second Theorem in [13], all eigenvalues of $\mathbf{F}$, $\lambda(\mathbf{F})$, satisfy

$$0 \leq \lambda(\mathbf{F}) < 1 \tag{4.22}$$

if $\mathbf{W}_1$ is non-singular. Note that the number of non-zero $\lambda(\mathbf{F})$ equals the dimension of $\mathcal{N}(\mathbf{B})$ [13, p. 1033].

4.5.3 Steady-State Properties

If $\mathbf{u}_\mathrm{d}$ satisfies $\mathbf{B}\mathbf{u}_d = \mathbf{v}_d$, the steady-state control distribution of (4.18) is given by

$$\lim_{\mathrm{t}\to\infty} \mathbf{u}(\mathrm{t}) = \mathbf{u}_d \tag{4.23}$$

according to the third Theorem in [13].

4.6 Redistributed Pseudoinverse Control Allocation Method

4.6.1 Formulation of the CA Problem

The CGI control allocation method intends to approximately solve the bounded sequential least-squares problem

$$\min_{\mathrm{u(t)} \,\in\, \Omega_{\mathrm{u}}} \{\|\mathbf{W}_{\mathrm{u}}\ (\mathbf{u} - \mathbf{u}_d)\|_2\} \tag{4.24}$$

where Ω_{u} is the set of control signals solving (4.15), and Ω_{u} minimizes the virtual control error, weighted by matrix $\mathbf{W}_{\mathrm{v}}$.

4.6.2 Solution of the CA Problem

The optimal control vector is defined by

$$\mathbf{u} = \mathbf{B}^{+}\mathbf{v} \tag{4.25}$$

Applying the weighted generalized inverse

$$\mathbf{B}^{+} = \mathbf{W}_{\mathrm{u}}^{-1}\mathbf{B}^{\top}\left(\mathbf{B}\mathbf{W}_{\mathrm{u}}^{-1}\mathbf{B}^{\top}\right)^{-1} \qquad \text{[16, p. 452]} \tag{4.26}$$

and rewriting (4.25) gives

$$\mathbf{u} = \mathbf{W}_{\mathrm{u}}^{-1}\mathbf{B}^{\top}\left(\mathbf{B}\mathbf{W}_{\mathrm{u}}^{-1}\mathbf{B}^{\top}\right)^{-1}\mathbf{v}. \tag{4.27}$$

The algorithm stops if the solution determined does not violate the constraints. If elements of the control vector $\mathbf{u}$ exceed the limits, the matrix $\mathbf{B}$ is changed by zeroing out the column corresponding to the reaction wheel saturating or failing [11, p. 705].

4.6.3 Tailoring of the Generalized Inverse

An alternative to the calculation of the generalized inverse is tailoring. Theorems 1 and 2 in [10] are used to calculate the tailored generalized inverse in the context of control allocation.

Interpretation of Theorem 1: $\mathbf{B}^{+}$ must satisfy

$$\mathbf{u}' = \mathbf{B}^{+}\mathbf{B}\mathbf{u}' \Leftrightarrow [\mathbf{B}^{+}\mathbf{B} - \mathbf{I}_{\mathrm{n}\times\mathrm{n}}]\mathbf{u}' = \mathbf{0} \quad \forall\ \mathbf{u}' \in \mathbb{R}^{\mathrm{r}} \tag{4.28}$$

where the constrained control vectors mapping to the boundary of Ω_v, $\delta(\Omega_v)$, are denoted by

$$\mathbf{u}' = \{\mathbf{u} \in \Omega_u \ \cap \ \mathcal{N}[\mathbf{B}^+\mathbf{B} - \mathbf{I}_{n\times n}] \ \mid \mathbf{B}\mathbf{u} \in \Omega_v\}. \tag{4.29}$$

Checking if there exists any $\mathbf{B}^+$ that satisfies all points in Ω_v without violation of the control constraints gives

$$\exists \ ? \ \mathbf{B}^+ \mid \mathbf{u} = \mathbf{B}^+\mathbf{v}^* \ , \ \mathbf{u} \in \Omega_u, \ \forall \ \mathbf{v}^* \tag{4.30}$$

where the subset of $\mathbf{v}$ lying on the boundary of Ω_v, $\delta(\Omega_v)$, is denoted by $\mathbf{v}^*$. Similarly, the subset of $\mathbf{u}$ lying on the boundary of Ω_u, $\delta(\Omega_u)$, is denoted by $\mathbf{u}^*$. From Theorem 1, it follows that the controls $\mathbf{u}'$ span $\mathbb{R}^r$. Thus, not all $\mathbf{u}'$ can lie in $\mathcal{N}[\mathbf{B}^+\mathbf{B} - \mathbf{I}_{n\times n}]$. The conclusion is that there exists no generalized inverse of $\mathbf{B}$ providing solutions everywhere on the boundary [10, p. 721].

Interpretation of Theorem 2: For no more than $(r - n)n$ arbitrary values of $\mathbf{v}$, equation $\mathbf{u} = \mathbf{B}^+\mathbf{v}$ is satisfied exactly. This Theorem implies that the generalized inverse cannot be "anchored" at more than $(r - n)n$ points on the boundary [10, p. 721]. The idea is to calculate a tailored generalized inverse for each sector, and the inverses yield the unique solution exactly at the points of intersection with the boundary of Ω_v. According to [10], a partition of $\mathbf{B}$ and $\mathbf{B}^+$ is possible as follows:

$$\begin{aligned} \mathbf{B} &= [\mathbf{B}_1 \,\vdots\, \mathbf{B}_2], \ \mathbf{B}_1 \in \mathbb{R}^{n\times n}, \ |\mathbf{B}_1| \neq 0, \ \mathbf{B}_2 \in \mathbb{R}^{n\times(r-n)} && (4.31) \\ \mathbf{B}^+ &= \begin{bmatrix} \mathbf{B}_1^+ \\ \cdots \\ \mathbf{B}_2^+ \end{bmatrix}, \ \mathbf{B}_1^+ \in \mathbb{R}^{n\times n}, \ \mathbf{B}_2^+ \in \mathbb{R}^{(r-n)\times n} \quad [10, \text{p. } 721]. && (4.32) \end{aligned}$$

Thus, the relationship between $\mathbf{B}$ and $\mathbf{B}^+$ may be described as

$$\begin{aligned} \mathbf{B}\mathbf{B}^+ &= \mathbf{I}_{n\times n} \\ \Leftrightarrow \mathbf{B}_1\mathbf{B}_1^+ + \mathbf{B}_2\mathbf{B}_2^+ &= \mathbf{I}_{n\times n} \\ \Leftrightarrow \mathbf{B}_1^+ &= (\mathbf{B}_1)^{-1} - (\mathbf{B}_1)^{-1}\mathbf{B}_2\mathbf{B}_2^+ \quad [10, \text{p. } 721] \end{aligned} \tag{4.33}$$

(4.33) implies that any choice of $\mathbf{B}_2^+$ ultimately determines $\mathbf{B}^+$ [10, p. 721].
Similarly, the admissible control vector $\mathbf{u}^*$ may be partioned into

$$\mathbf{u}^* = \begin{bmatrix} \mathbf{u}_1^* \\ \mathbf{u}_2^* \end{bmatrix}, \ \mathbf{u}_1^* \in \mathbb{R}^{n\times 1}, \ \mathbf{u}_2^* \in \mathbb{R}^{(r-n)\times 1} \qquad [10, \text{p. } 722] \tag{4.34}$$

where $\mathbf{u}_1^* = [\mathbf{u}_{1,1}^* \quad \mathbf{u}_{1,2}^*]^\top$ and $\mathbf{u}_2^* = [\mathbf{u}_{2,1}^* \quad \mathbf{u}_{2,2}^*]^\top$. According to [10], it is required to solve only $\mathbf{B}_2^+\mathbf{v}^* = \mathbf{u}^*$, where $\mathbf{v}^*$ denotes the attainable controls. Thus, calculating $\mathbf{B}_2^+ \in \mathbb{R}^{(\mathrm{r-n})\times \mathrm{n}}$ gives

$$
\begin{aligned}
\mathbf{B}_2^+\mathbf{v}_1^* &= (\mathbf{v}_1^*)^\top \left(\mathbf{B}_2^+\right)^\top = \left(\mathbf{u}_{1,2}^*\right)^\top \\
\mathbf{B}_2^+\mathbf{v}_2^* &= (\mathbf{v}_2^*)^\top \left(\mathbf{B}_2^+\right)^\top = \left(\mathbf{u}_{2,2}^*\right)^\top \\
\Leftrightarrow \begin{bmatrix} (\mathbf{v}_1^*)^\top \\ (\mathbf{v}_2^*)^\top \end{bmatrix} \left(\mathbf{B}_2^+\right)^\top &= \begin{bmatrix} \mathbf{u}_{1,2}^* \\ \mathbf{u}_{2,2}^* \end{bmatrix}^\top \\
\Leftrightarrow \left(\mathbf{B}_2^+\right)^\top &= \begin{bmatrix} (\mathbf{v}_1^*)^\top \\ (\mathbf{v}_2^*)^\top \end{bmatrix}^{-1} \begin{bmatrix} \mathbf{u}_{1,2}^* \\ \mathbf{u}_{2,2}^* \end{bmatrix}^\top \quad \text{[10, p. 722].}
\end{aligned}
\tag{4.35}
$$

Finally, the single inverses (4.33) and (4.35) may be merged to the tailored generalized inverse according to (4.32).

Chapter 5

Simulation of Spacecraft Model and Control Allocation

5.1 Satellite Mission

Table 5.1 gives a list of the ADCS target types of interest. When detumbling, magnetorquers have to slow down and stabilize the spin rates of the satellite while acting on the Earth's magnetic field.
Pointing is characterized by the vector that points or is aligned. When pointing, the satellite points the remote-sensing instruments to a certain point for scientific observations. This means, e.g., nadir (straight down) or fixed-target pointing. At nadir, the desired Euler angles for roll, pitch, and yaw are defined to as $\Phi_d = [0 \;\; 0 \;\; 0]^\top$ and the corresponding quaternion parameterization is the vector $\mathbf{q}_d = [1 \;\; 0 \;\; 0 \;\; 0]^\top$. During nadir pointing, the spacecraft's $\hat{\mathbf{z}}_b$-axis points along the position vector towards the Earth's center, perpendicular to the Earth's surface. As the satellite points to nadir, the hyperspectral camera captures data in a push-broom fashion when moving over the ground. The satellite must rotate once per orbit around the pitch axis with a rotation rate that varies due to the orbit being non-circular to remain the satellite pointing at nadir. From this, an angular velocity about the satellite's center of mass is required. Having momentum bias in the $\hat{\mathbf{z}}_b$-axis of the satellite naturally tends to orient it at nadir. During fixed-target pointing (ECEF tracking), the satellite points towards a reference point or performs target tracking on the Earth's surface or space. The hyperspectral camera does not scan the ground in push-broom fashion while in this mode but instead stacking several frames with a limited field of view in-track.

ADCS target types	description	actuators used	sensors used	SC face
detumbling	SC uses magnetorquers to despin and stabilize during EPS safe mode and critical mode	MTQs	magnetometers, sun-sensors, and gyroscopes	all SC faces
nadir pointing	SC points the $\hat{\mathbf{z}}_b$-face at nadir	MTQs and RWs	magnetometers, sun-sensors, gyroscopes (or IMU), and star-tracker	$\hat{\mathbf{z}}_b$-face
velocity vector pointing	SC points arbitrary face towards velocity vector	MTQs and RWs	magnetometers, sun-sensors, and gyroscopes	arbitrary
slew maneuver	SC performs slew maneuver for HSI imaging	MTQs and RWs	IMU and star-tracker	$\hat{\mathbf{z}}_b$-face

Table 5.1. – Target types for ADCS

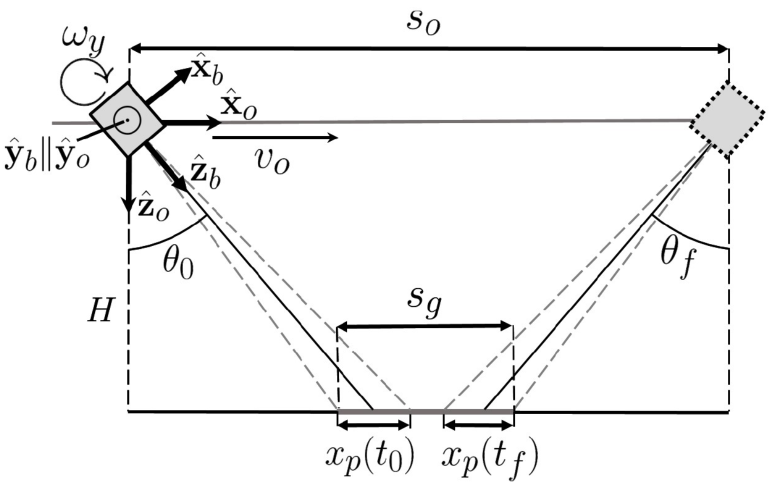

Figure 5.1. – Satellite performing a single-axis slew maneuver [5, p. 7]

As shown in Figure 5.1, the single-axis slew maneuver is composed of the sequences slew preparation, start imaging at an angle θ_0, image acquisition at a constant angular velocity $\omega^b_{ob,y}$, end imaging at an angle θ_f, data processing, and downlink. In Figure 5.1, the orbital distance is denoted by s_o, and the ground distance is denoted by s_g.

The starting and final along-track footprint are denoted by $x_p(t_0)$ and $x_p(t_f)$.
During slew preparation, the satellite must maneuver to the reference viewing angle θ_0 by actuating its reaction wheels to generate momentum along the in-track direction. Once the sensing axis hits the reference angle, the spacecraft actuates again with momentum in the opposite direction, and the slew rate is held as constant as possible.
Slewing shall happen about the $\hat{\mathbf{y}}_b$-axis with the lowest inertia (I_{xx}). From this, it follows that the star-tracker must be positioned with at least initial points, at best at all times towards space. The satellite must slew at a constant angular rate along 1-axis to have a consistent set of frames mapping the ground. To avoid disturbances and random noise from several sensors, only the gyroscopes/IMU and reaction wheels are assumed to operate in this mode.

5.2 Setup

5.2.1 Matlab/Simulink Implementation

The implementation that is part of this master's thesis is available on the internal GitHub page of the NTNU SmallSat Lab [47]. In addition, the implementations of other research projects listed in Chapter 1.2.1 are also available there.
Figure 5.2 shows the implementation scheme. There exist two Simulink models for the simulation of a single attitude case: one for the original spacecraft model (`Simulink`), and one for the model applying a specific CA method (e.g., `Simulink_CGI`). Some functions of the Simulink models base on the m-functions for kinematics from professor Thor I. Fossen's marine systems simulator (MSS) toolbox [48].
The spacecraft model performing pointing does not require a kinematic equation $\dot{\mathbf{q}}_d$ to determine the attitude error variables $\tilde{\eta}$ and $\tilde{\boldsymbol{\epsilon}}$ for the PD controller. To run the Simulink models, it is necessary to define simulation parameters beforehand, such as the initial and desired states $\mathbf{x}_0 = [\mathbf{q}_0 \;\; \boldsymbol{\omega}^b_{ob,0} \;\; \boldsymbol{\omega}^w_{\mathrm{s},0}]^\top$, and $\mathbf{x}_d = [\mathbf{q}_d \;\; \boldsymbol{\omega}^b_{ob,d} \;\; \boldsymbol{\omega}^w_{\mathrm{s},d}]^\top$. This task is done in the m-file `main`. The simulation starts for all cases at time $\mathrm{t}_0 = 0$ s and ends at time $\mathrm{t}_f = 200$ s. The magnetorquer mode is set to momentum dumping for all attitude cases and the detumbling torque is zero. After a successful simulation of the models, the variables of interest are saved in a the data files `Simulation_Data`, and `Simulation_Data_CGI`. From this, the plots for the simulation of the two models are generated using the m-files `Plots` and `Plots_CGI`.
An author who published several papers on constrained CA, Ola Härkegård, provides a Quadratic Programming Control Allocation Toolbox (QCAT) with implementation suggestions of various CA methods [49]. The m-functions applied are `vview` and `vview_demo` to view the attainable virtual control set according to the definitions in Chapter 4.2. To perform the CGI control allocation method, the m-functions `cgi_alloc`, and `pinv_sol` are applied. To perform the CGI control allocation script provided by the toolbox, the following input parameters are required: the control effectiveness matrix $\mathbf{B} \in \mathbb{R}^{\mathrm{n}\times\mathrm{r}}$, commanded virtual control $\mathbf{v} \in \mathbb{R}^{\mathrm{n}\times 1}$, lower position limits $\mathbf{u}_{\mathrm{min}} \in \mathbb{R}^{\mathrm{r}\times 1}$, upper position limits $\mathbf{u}_{\mathrm{max}} \in \mathbb{R}^{\mathrm{r}\times 1}$, desired control $\mathbf{u}_d \in \mathbb{R}^{\mathrm{r}\times 1}$, virtual control weighting matrix $\mathbf{W}_{\mathrm{v}} \in \mathbb{R}^{\mathrm{n}\times\mathrm{n}}$, control weighting matrix $\mathbf{W}_{\mathrm{u}} \in \mathbb{R}^{\mathrm{r}\times\mathrm{r}}$, and the maximum number of iterations. Chapter 5.5 describes the tuning of the CA parameters, depending on if an attitude case with full controllability is given or not.

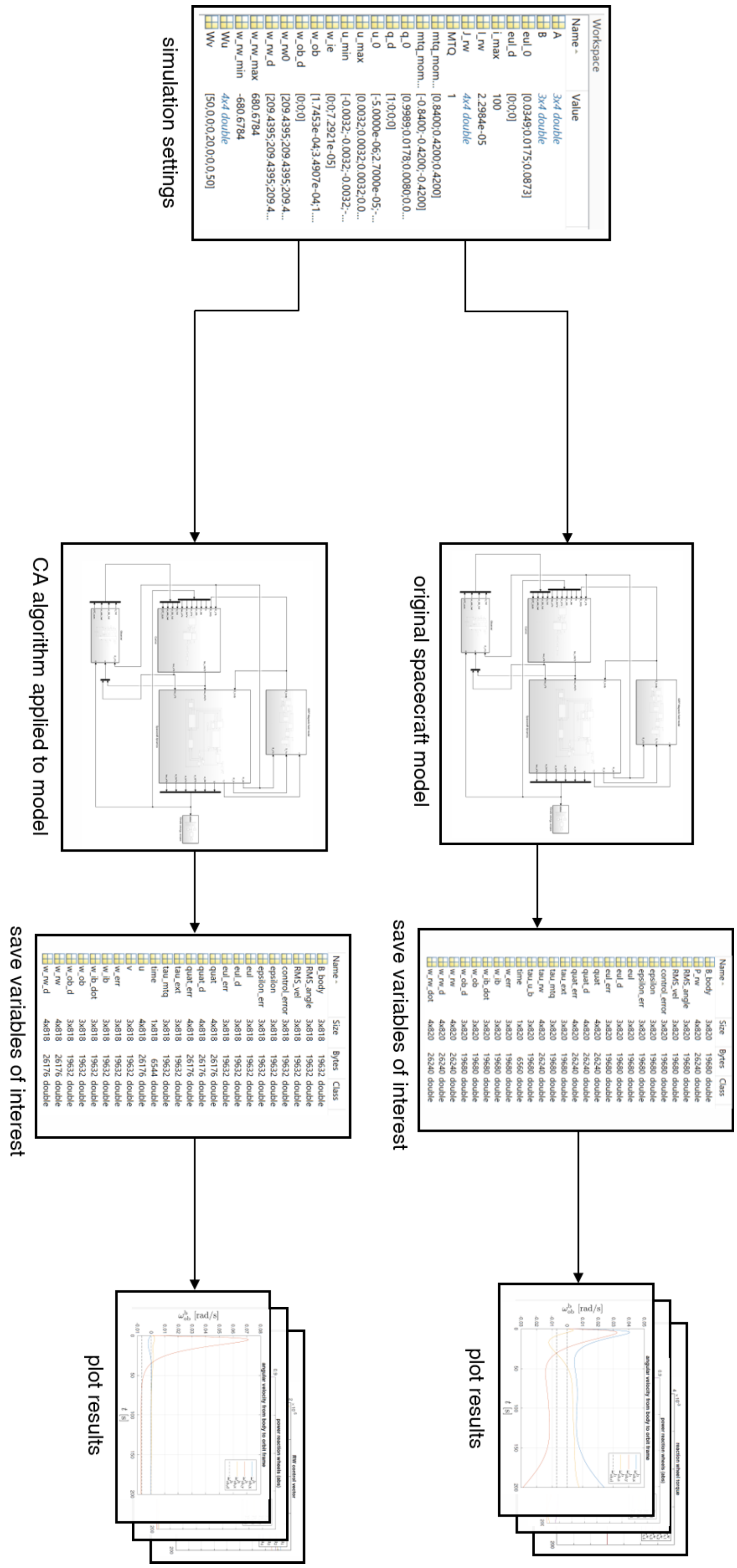

Figure 5.2. – Implementation scheme

The output of the CA algorithms of the toolbox is the (approximately) optimal solution $\mathbf{u} \in \mathbb{R}^{\mathrm{r}}$, compared to the RW torque $\boldsymbol{\tau}_{\mathrm{s}}^{w}$ provided by the original spacecraft model. Furthermore, the number of iterations, or the number of pseudoinverse solutions, is computed. The number of iterations is a suitable criterion to evaluate computational effectiveness.
Further details on the implementation are provided in Appendix D.

5.2.2 Noise and RWA Uncertainties

5.2.2.1 Noise

Noise is added to the system on three variables:

1. The standard deviation of the noise on $\boldsymbol{\omega}_{\mathrm{s}}^{w}$ is set to $2\dfrac{\pi}{30}$ rad/s, representing jittering on the reaction wheels (vibrations).

2. The standard deviation of the noise on $\boldsymbol{\omega}_{ib}^{b}$ is set to $1 \cdot 10^{-6}$ rad/s, representing the measurement noise on the inertial measurement unit (IMU).

3. The mean of the noise on the attitude $\mathbf{q}$ is set to $0.01°$, representing noise on the startracker measurement (misalignment).

5.2.2.2 RWA Uncertainties

A small value perturbs the nominal RWA distribution matrix on each column before it is normalized [1, p. 48]. The perturbed RWA distribution matrix

$$\mathbf{A} = \begin{bmatrix} 0.9879 & 0.0902 & -0.1098 & 0.5442 \\ -0.1098 & 0.9918 & -0.1098 & 0.6385 \\ -0.1098 & 0.0902 & 0.9879 & 0.5442 \end{bmatrix} \qquad [1, \text{p. } 153] \tag{5.1}$$

represents the real RWA placement. Adding the uncertainties to the model may be done by setting the variable `UNCERTAIN_WHEELS` to one in the m-file `main`.

5.3 Simulation of Pointing with Different Angles to Attain

The PD controller gains are set to $\mathrm{K_p} = 0.005$ and $\mathrm{K_d} = 0.03$ for all pointing cases. For all pointing cases, the initial angular velocity of the spacecraft is defined as $\boldsymbol{\omega}^b_{ob,0} = [0.01 \;\; 0.02 \;\; 0.01]^\top \;{}^\circ/\mathrm{s}$, and for the desired state it is defined as $\boldsymbol{\omega}^b_{ob,d} = [0 \;\; 0 \;\; 0]^\top \;{}^\circ/\mathrm{s}$.

5.3.1 Pointing With Full Controllability

Tables 5.2 and 5.3 show the simulation parameters for the pointing cases one to eleven, where full controllability is given.

criteria	**definition**
Pointing - Case 1: $\theta_d = 0\ ^\circ$	
initial state	$\boldsymbol{\Phi}_0 = [2 \;\; 1 \;\; 5]^\top\ ^\circ$
desired state	$\boldsymbol{\Phi}_d = [0 \;\; 0 \;\; 0]^\top\ ^\circ$
Pointing - Case 2: $\theta_d = 20\ ^\circ$	
initial state	$\boldsymbol{\Phi}_0 = [2 \;\; 24 \;\; 5]^\top\ ^\circ$
desired state	$\boldsymbol{\Phi}_d = [0 \;\; 20 \;\; 0]^\top\ ^\circ$
Pointing - Case 3: $\theta_d = 40\ ^\circ$	
initial state	$\boldsymbol{\Phi}_0 = [2 \;\; 45 \;\; 5]^\top\ ^\circ$
desired state	$\boldsymbol{\Phi}_d = [0 \;\; 40 \;\; 0]^\top\ ^\circ$

Table 5.2. – Simulation parameters for the first three pointing cases

For the first three pointing cases, the initial RW angular velocity is defined as $\boldsymbol{\omega}^w_{\mathrm{s},0} = [2000 \;\; 2000 \;\; 2000 \;\; -\sqrt{3}\ 2000]^\top$ rpm, and the desired state is defined as $\boldsymbol{\omega}^w_{\mathrm{s},d} = [2000 \;\; 2000 \;\; 2000 \;\; -\sqrt{3}\ 2000]^\top$ rpm. In the pointing cases four to thirteen, the initial attitude is defined as $\boldsymbol{\Phi}_0 = [2 \;\; 24 \;\; 5]^\top\ ^\circ$, and the desired attitude is defined as $\boldsymbol{\Phi}_d = [0 \;\; 20 \;\; 0]^\top\ ^\circ$. Table 5.3 shows the settings for the pointing cases four to eleven. When saturation occurs, the RWA distribution matrix does not change. When a failure occurs, the column of the malfunctioning reaction wheel is equal to zero. In the pointing cases one to eleven, the RWA distribution matrix $\mathbf{A}$ has full rank. So these attitude cases are referred to as cases with full controllability.

criteria	**definition**
Pointing - Case 4: $\theta_d = 20\ ^\circ$, saturation of RW 1	
initial state desired state	$\boldsymbol{\omega}_{\mathrm{s},0}^{w} = [6589\ \ 2000\ \ 2000\ \ -\sqrt{3}\ 2000]^\top$ rpm $\boldsymbol{\omega}_{\mathrm{s},d}^{w} = [2000\ \ 2000\ \ 2000\ \ -\sqrt{3}\ 2000]^\top$ rpm
Pointing - Case 5: $\theta_d = 20\ ^\circ$, saturation of RW 2	
initial state desired state	$\boldsymbol{\omega}_{\mathrm{s},0}^{w} = [2000\ \ 6589\ \ 2000\ \ -\sqrt{3}\ 2000]^\top$ rpm $\boldsymbol{\omega}_{\mathrm{s},d}^{w} = [2000\ \ 2000\ \ 2000\ \ -\sqrt{3}\ 2000]^\top$ rpm
Pointing - Case 6: $\theta_d = 20\ ^\circ$, saturation of RW 3	
initial state desired state	$\boldsymbol{\omega}_{\mathrm{s},0}^{w} = [2000\ \ 2000\ \ 6589\ \ -\sqrt{3}\ 2000]^\top$ rpm $\boldsymbol{\omega}_{\mathrm{s},d}^{w} = [2000\ \ 2000\ \ 2000\ \ -\sqrt{3}\ 2000]^\top$ rpm
Pointing - Case 7: $\theta_d = 20\ ^\circ$, saturation of RW 4	
initial state desired state	$\boldsymbol{\omega}_{\mathrm{s},0}^{w} = [2000\ \ 2000\ \ 2000\ \ -6589]^\top$ rpm $\boldsymbol{\omega}_{\mathrm{s},d}^{w} = [2000\ \ 2000\ \ 2000\ \ -\sqrt{3}\ 2000]^\top$ rpm
Pointing - Case 8: $\theta_d = 20\ ^\circ$, failure of RW 1	
initial state desired state	$\boldsymbol{\omega}_{\mathrm{s},0}^{w} = [0\ \ 2000\ \ 2000\ \ -\sqrt{3}\ 2000]^\top$ rpm $\boldsymbol{\omega}_{\mathrm{s},d}^{w} = [0\ \ 2000\ \ 2000\ \ -\sqrt{3}\ 2000]^\top$ rpm
Pointing - Case 9: $\theta_d = 20\ ^\circ$, failure of RW 2	
initial state desired state	$\boldsymbol{\omega}_{\mathrm{s},0}^{w} = [2000\ \ 0\ \ 2000\ \ -\sqrt{3}\ 2000]^\top$ rpm $\boldsymbol{\omega}_{\mathrm{s},d}^{w} = [2000\ \ 0\ \ 2000\ \ -\sqrt{3}\ 2000]^\top$ rpm
Pointing - Case 10: $\theta_d = 20\ ^\circ$, failure of RW 3	
initial state desired state	$\boldsymbol{\omega}_{\mathrm{s},0}^{w} = [2000\ \ 2000\ \ 0\ \ -\sqrt{3}\ 2000]^\top$ rpm $\boldsymbol{\omega}_{\mathrm{s},d}^{w} = [2000\ \ 2000\ \ 0\ \ -\sqrt{3}\ 2000]^\top$ rpm
Pointing - Case 11: $\theta_d = 20\ ^\circ$, failure of RW 4	
initial state desired state	$\boldsymbol{\omega}_{\mathrm{s},0}^{w} = [2000\ \ 2000\ \ 2000\ \ 0]^\top$ rpm $\boldsymbol{\omega}_{\mathrm{s},d}^{w} = [2000\ \ 2000\ \ 2000\ \ 0]^\top$ rpm

Table 5.3. – Simulation parameters for the pointing cases four to eleven

5.3.2 Pointing With No Full Controllability

Table 5.4 shows the settings for the twelfth and thirteenth pointing cases, where two specific reaction wheels fail.

criteria	**definition**
Pointing - Case 12: $\theta_d = 20\ ^\circ$, failure of RWs 1 and 2	
initial state	$\boldsymbol{\omega}^w_{s,0} = [0\ \ 0\ \ 2000\ \ -\sqrt{3}\ 2000]^\top$ rpm
desired state	$\boldsymbol{\omega}^w_{s,d} = [0\ \ 0\ \ 2000\ \ -\sqrt{3}\ 2000]^\top$ rpm
RWA matrix	$\mathbf{A} = \begin{bmatrix} 0 & 0 & 0 & \frac{1}{\sqrt{3}} \\ 0 & 0 & 0 & \frac{1}{\sqrt{3}} \\ 0 & 0 & 1 & \frac{1}{\sqrt{3}} \end{bmatrix}$
Pointing - Case 13: $\theta_d = 20\ ^\circ$, failure of RWs 1 and 4	
initial state	$\boldsymbol{\omega}^w_{s,0} = [0\ \ 2000\ \ 2000\ \ 0]^\top$ rpm
desired state	$\boldsymbol{\omega}^w_{s,d} = [0\ \ 2000\ \ 2000\ \ 0]^\top$ rpm
RWA matrix	$\mathbf{A} = \begin{bmatrix} 0 & 0 & 0 & 0 \\ 0 & 1 & 0 & 0 \\ 0 & 0 & 1 & 0 \end{bmatrix}$

Table 5.4. – Simulation parameters for the twelfth and thirteenth pointing case

In the pointing cases twelfth and thirteen, the RWA distribution matrix $\mathbf{A}$ has a rank of two ($<$ n). So these attitude cases are referred to as cases with no full controllability.

5.4 Simulation of Slewing at Different Angular Velocities

The PD controller gains are set to $K_p = 0.0075$ and $K_d = 0.05$ for all slewing cases. In the slewing cases four to thirteen, the satellite rotates from $\theta_0 = –40\ ^\circ$ to $\theta_f = 40\ ^\circ$ at a constant angular velocity of $\omega^b_{ob,y} = –0.007$ rad/s.

5.4.1 Slewing With Full Controllability

Table 5.5 shows the simulation settings for the first three slewing cases. For the first three slewing cases, the initial and desired RW angular velocity is defined as $\boldsymbol{\omega}^w_{s,0} = [2000\ \ 2000\ \ 2000\ \ -\sqrt{3}\,2000]^\top$ rpm and $\boldsymbol{\omega}^w_{s,d} = [2000\ \ 2000\ \ 2000\ \ -\sqrt{3}\,2000]^\top$ rpm.

criteria	**definition**
Slewing - Case 1: $\omega^b_{ob,y} = –0.0035$ rad/s	
initial state	$\Phi_0 = [–2\ \ -20\ \ -5]^\top\ ^\circ$
	$\boldsymbol{\omega}^b_{ob,0} = [0.01\ \ 0.02\ \ 0.01]^\top\ ^\circ/\mathrm{s}$
desired state	$\Phi_d = [0\ \ 20\ \ 0]^\top\ ^\circ$
	$\boldsymbol{\omega}^b_{ob,d} = [0\ \ -0.2\ \ 0]^\top\ ^\circ/\mathrm{s}$
Slewing - Case 2: $\omega^b_{ob,y} = –0.007$ rad/s	
initial state	$\Phi_0 = [–2\ \ -40\ \ -5]^\top\ ^\circ$
	$\boldsymbol{\omega}^b_{ob,0} = [0.01\ \ 0.02\ \ 0.01]^\top\ ^\circ/\mathrm{s}$
desired state	$\Phi_d = [0\ \ 40\ \ 0]^\top\ ^\circ$
	$\boldsymbol{\omega}^b_{ob,d} = [0\ \ -0.4\ \ 0]^\top\ ^\circ/\mathrm{s}$
Slewing - Case 3: $\omega^b_{ob,y} = –0.0105$ rad/s	
initial state	$\Phi_0 = [–2\ \ -60\ \ -5]^\top\ ^\circ$
	$\boldsymbol{\omega}^b_{ob,0} = [0.01\ \ 0.02\ \ 0.01]^\top\ ^\circ/\mathrm{s}$
desired state	$\Phi_d = [0\ \ 60\ \ 0]^\top\ ^\circ$
	$\boldsymbol{\omega}^b_{ob,d} = [0\ \ -0.6\ \ 0]^\top\ ^\circ/\mathrm{s}$

Table 5.5. – Simulation parameters for the first three slewing cases

Slewing cases one to eleven are characterized by full controllability, as defined in Chapter 5.3.1.

criteria	definition
Slewing - Case 4: $\omega^b_{ob,y} = –0.007$ rad/s, saturation of RW 1	
initial state	$\boldsymbol{\omega}^w_{s,0} = [6589 \;\; 2000 \;\; 2000 \;\; -\sqrt{3}\,2000]^\top$ rpm
desired state	RW dynamics (3.5.4) in $\mathcal{F}_d$
Slewing - Case 5: $\omega^b_{ob,y} = –0.007$ rad/s, saturation of RW 2	
initial state	$\boldsymbol{\omega}^w_{s,0} = [2000 \;\; 6589 \;\; 2000 \;\; -\sqrt{3}\,2000]^\top$ rpm
desired state	RW dynamics (3.5.4) in $\mathcal{F}_d$
Slewing - Case 6: $\omega^b_{ob,y} = –0.007$ rad/s, saturation of RW 3	
initial state	$\boldsymbol{\omega}^w_{s,0} = [2000 \;\; 2000 \;\; 6589 \;\; -\sqrt{3}\,2000]^\top$ rpm
desired state	RW dynamics (3.5.4) in $\mathcal{F}_d$
Slewing - Case 7: $\omega^b_{ob,y} = –0.007$ rad/s, saturation of RW 4	
initial state	$\boldsymbol{\omega}^w_{s,0} = [2000 \;\; 2000 \;\; 2000 \;\; -6589]^\top$ rpm
desired state	RW dynamics (3.5.4) in $\mathcal{F}_d$
Slewing - Case 8: $\omega^b_{ob,y} = –0.007$ rad/s, failure of RW 1	
initial state	$\boldsymbol{\omega}^w_{s,0} = [0 \;\; 2000 \;\; 2000 \;\; -\sqrt{3}\,2000]^\top$ rpm
desired state	$\boldsymbol{\omega}^w_{s,d} = [0 \;\; 2000 \;\; 2000 \;\; -\sqrt{3}\,2000]^\top$ rpm
Slewing - Case 9: $\omega^b_{ob,y} = –0.007$ rad/s, failure of RW 2	
initial state	$\boldsymbol{\omega}^w_{s,0} = [2000 \;\; 0 \;\; 2000 \;\; -\sqrt{3}\,2000]^\top$ rpm
desired state	$\boldsymbol{\omega}^w_{s,d} = [2000 \;\; 0 \;\; 2000 \;\; -\sqrt{3}\,2000]^\top$ rpm
Slewing - Case 10: $\omega^b_{ob,y} = –0.007$ rad/s, failure of RW 3	
initial state	$\boldsymbol{\omega}^w_{s,0} = [2000 \;\; 2000 \;\; 0 \;\; -\sqrt{3}\,2000]^\top$ rpm
desired state	$\boldsymbol{\omega}^w_{s,d} = [2000 \;\; 2000 \;\; 0 \;\; -\sqrt{3}\,2000]^\top$ rpm
Slewing - Case 11: $\omega^b_{ob,y} = –0.007$ rad/s, failure of RW 4	
initial state	$\boldsymbol{\omega}^w_{s,0} = [2000 \;\; 2000 \;\; 2000 \;\; 0]^\top$ rpm
desired state	$\boldsymbol{\omega}^w_{s,d} = [2000 \;\; 2000 \;\; 2000 \;\; 0]^\top$ rpm

Table 5.6. – Simulation parameters for the slewing cases four to eleven

5.4.2 Slewing With No Full Controllability

Table 5.7 shows the settings for the twelfth and thirteenth slewing cases, where two specific reaction wheels fail. Slewing cases twelve and thirteen are characterized by no full controllability, as defined in Chapter 5.3.2.

criteria	**definition**
Slewing - Case 12: $\omega^b_{ob,y} = -0.007$ rad/s, failure of RWs 1 and 2	
initial state	$\boldsymbol{\omega}^w_{s,0} = [0 \;\; 0 \;\; 2000 \;\; -\sqrt{3}\;2000]^\top$ rpm
desired state	$\boldsymbol{\omega}^w_{s,d} = [0 \;\; 0 \;\; 2000 \;\; -\sqrt{3}\;2000]^\top$ rpm
Slewing - Case 13: $\omega^b_{ob,y} = -0.007$ rad/s, failure of RWs 1 and 4	
initial state	$\boldsymbol{\omega}^w_{s,0} = [0 \;\; 2000 \;\; 2000 \;\; 0]^\top$ rpm
desired state	$\boldsymbol{\omega}^w_{s,d} = [0 \;\; 2000 \;\; 2000 \;\; 0]^\top$ rpm

Table 5.7. – Simulation parameters for the twelfth and thirteenth slewing case

5.5 CGI Control Allocation for the Defined Attitude Cases

5.5.1 CGI Control Allocation for all Attitude Cases

Table 5.8 shows the control allocation settings for all attitude control cases, where the maximum and minimum reaction wheel torques have been specified in Chapter 3.5.1. The characteristics of matrix **B**, full controllability or no full controllability, are detailed in Chapters 4.4.2, 5.3.1, and 5.3.2.

criteria	**definition**
Pointing and Slewing - all Cases	
control effectiveness matrix	$\mathbf{B} = -\mathbf{A}$ (spacecraft model)
commanded virtual control	$\mathbf{v} = \boldsymbol{\tau}_\mathrm{u}^b$ (spacecraft model)
lower control limit	$\mathbf{u}_\mathrm{min} = [\tau_\mathrm{s,min}^w \;\; \tau_\mathrm{s,min}^w \;\; \tau_\mathrm{s,min}^w \;\; \tau_\mathrm{s,min}^w]^\top$
upper control limit	$\mathbf{u}_\mathrm{max} = [\tau_\mathrm{s,max}^w \;\; \tau_\mathrm{s,max}^w \;\; \tau_\mathrm{s,max}^w \;\; \tau_\mathrm{s,max}^w]^\top$
desired control vector	$\mathbf{u}_d = \mathbf{B}^+\mathbf{v}$ (spacecraft model)
max. number of iterations	$\mathrm{i}_\mathrm{max} = 100$
sampling time	$\mathrm{T} = 0.25$

Table 5.8. – CGI CA settings for all attitude control cases

5.5.2 CGI Control Allocation for Attitude Cases With Full Controllability

Table 5.9 shows the CGI control allocation settings for all attitude cases (pointing and slewing). Chapter 6.1 presents the simulation results for the attitude cases with full controllability.

Remark: From the later evaluations in Chapter 6.1 and Appendix E, it is evident that the original spacecraft model fulfills the defined requirements very well. Thus, no additional tuning by weight matrices is necessary for the cases with full controllability. Only identity matrices are applied here.

criteria	**definition**
Pointing and Slewing - Cases 1 to 11	
control weighting matrix	$\mathbf{W}_{\mathrm{u}} = \begin{bmatrix} 1 & 0 & 0 & 0 \\ 0 & 1 & 0 & 0 \\ 0 & 0 & 1 & 0 \\ 0 & 0 & 0 & 1 \end{bmatrix}$
virtual control weighting matrix	$\mathbf{W}_{\mathrm{v}} = \begin{bmatrix} 1 & 0 & 0 \\ 0 & 1 & 0 \\ 0 & 0 & 1 \end{bmatrix}$

Table 5.9. – CGI control allocation settings for attitude cases with full controllability

5.5.3 CGI Control Allocation for Attitude Cases With No Full Controllability

Table 5.10 shows the settings for CGI control allocation for all attitude cases with no full controllability. Chapter 6.2 presents the simulation results for the attitude cases with no full controllability.

criteria	**definition**
Pointing and Slewing - Cases 12 and 13	
control weighting matrix	$\mathbf{W}_{\mathrm{u}} = \begin{bmatrix} 50 & 0 & 0 & 0 \\ 0 & 0 & 0 & 0 \\ 0 & 0 & -50 & 0 \\ 0 & 0 & 0 & 20 \end{bmatrix}$
virtual control weighting matrix	$\mathbf{W}_{\mathrm{v}} = \begin{bmatrix} 50 & 0 & 0 \\ 0 & 20 & 0 \\ 0 & 0 & 50 \end{bmatrix}$

Table 5.10. – CGI control allocation settings for attitude cases with no full controllability

Chapter 6

Simulation Results and Discussion

When comparing the variables of the original model with those of the CA model, it is necessary to check whether the results to be compared show stability in the sense of Chapter 3.8. Furthermore, high accuracy in attitude tracking and angular velocity tracking performance is required. The RMS of $\tilde{\Phi}$ and $\tilde{\boldsymbol{\omega}}_{ob}^{b}$ are used for comparison. It is essential to check if the constraints defined in Chapter 4.2 are not violated and if the solution is feasible. The original model is placed on the left and the modified model on the right side for all comparisons.
Practical implications of the results are discussed in Chapter 6.3.

6.1 Simulation Results for Pointing and Slewing Cases With Full Controllability

This chapter presents the comparison for the second and ninth pointing and slewing cases exemplarily. For the attitude tracking cases with full controllability, complementary plots are shown in Appendix E. As expected, the left and right sides behave similarly.

6.1.1 Comparison for the Second Pointing Case

For the second pointing case, Figures 6.1, 6.2, 6.4, 6.5, and 6.7 show that the variables converge to the desired states as defined in Tables 5.2 and 5.8. Figure 6.3 compares the attitude tracking performance (RMSE), and Figure 6.6 compares the absolute power of the reaction wheels. Complementary plots for this case are shown in Appendix E.1.

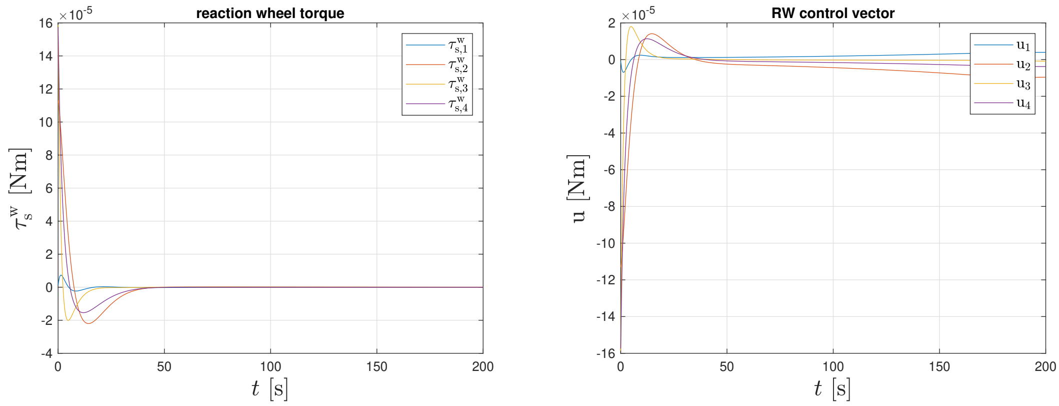

(a) **(b)**

Figure 6.1. – RW torque without / with CGI CA

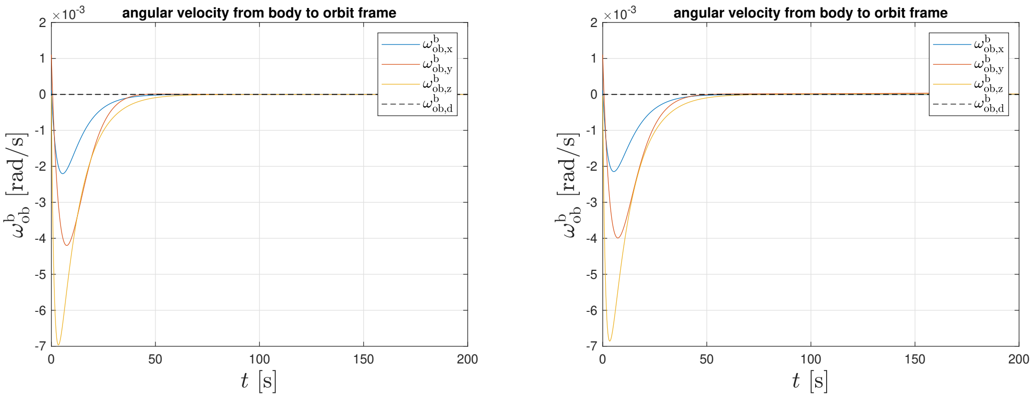

(a) **(b)**

Figure 6.2. – Angular velocity from $\mathcal{F}_b$ to $\mathcal{F}_o$ without / with CGI CA

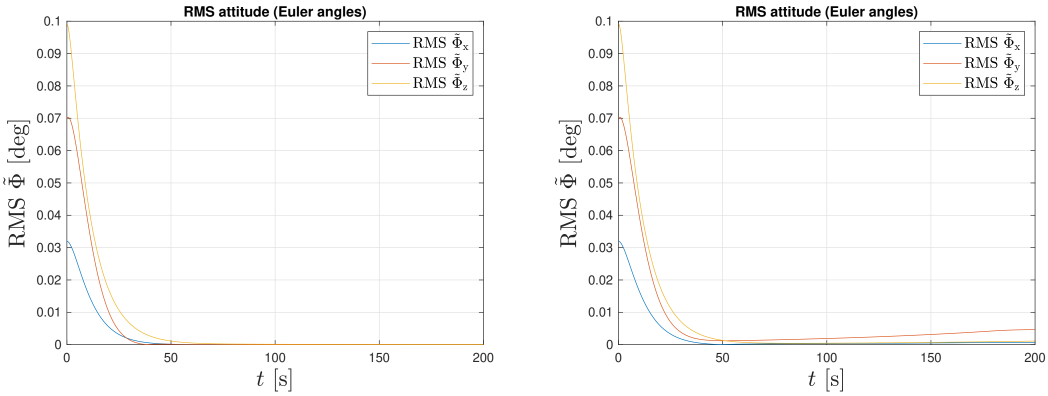

(a) (b)

Figure 6.3. – RMS of attitude in Euler angles without / with CGI CA

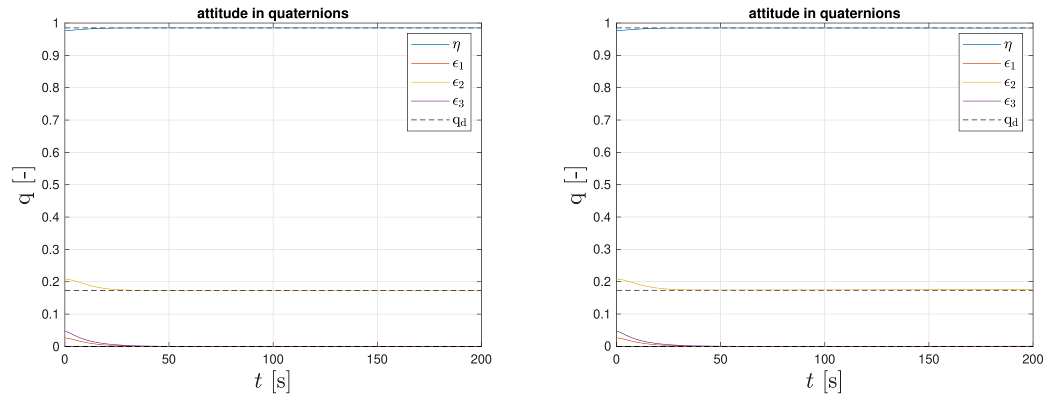

(a) (b)

Figure 6.4. – Attitude (quaternions) without / with CGI CA

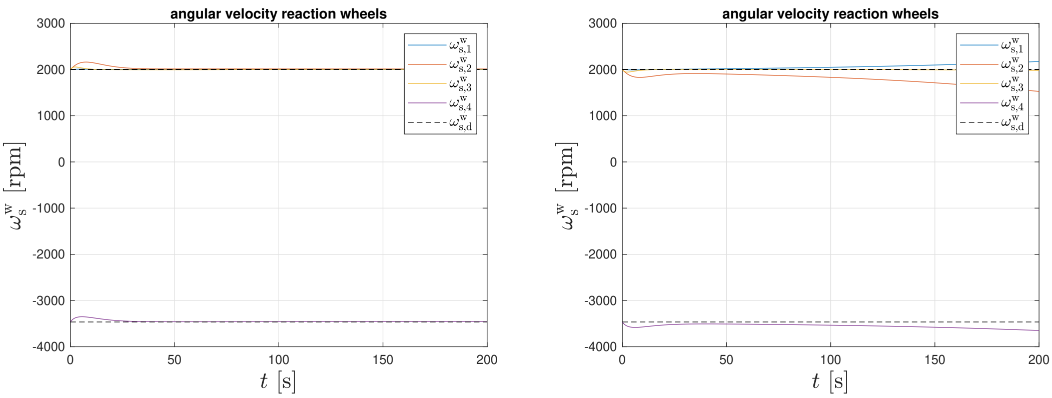

(a) (b)

Figure 6.5. – RW angular velocity without / with CGI CA

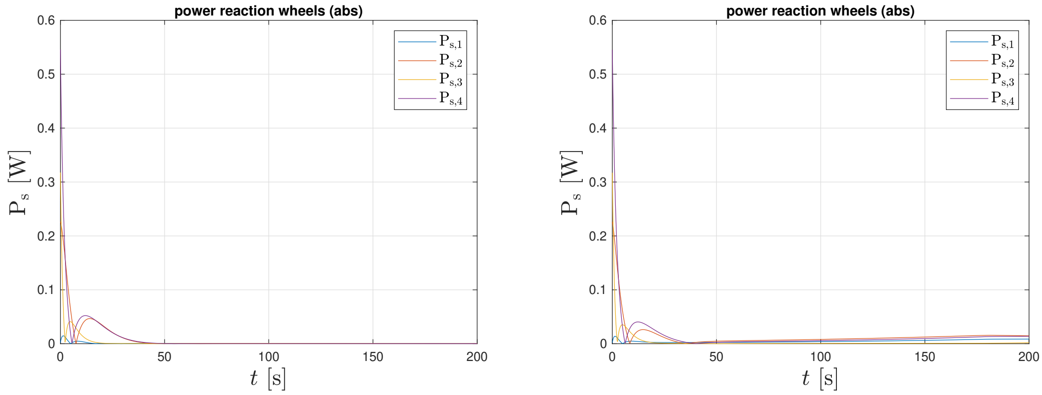

(a) (b)

Figure 6.6. – Power (absolute) without / with CGI CA

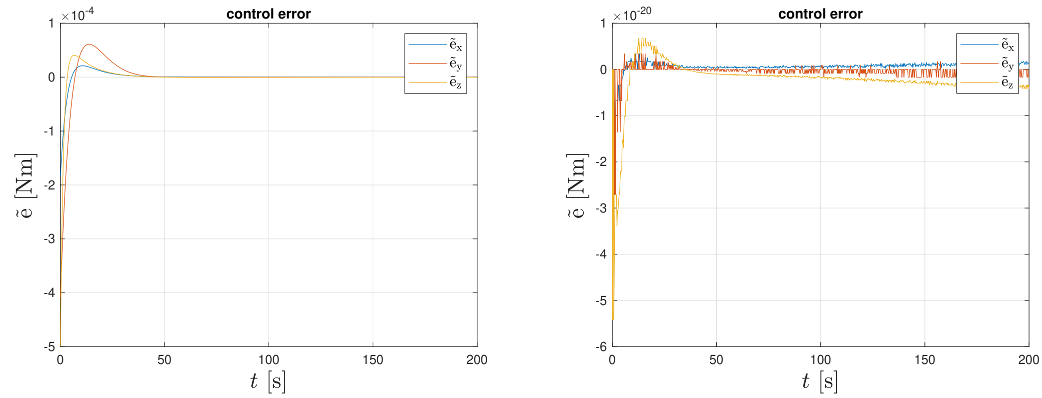

(a) (b)

Figure 6.7. – Control error without / with CGI CA

6.1.2 Comparison for the Second Slewing Case

For the second slewing case, Figures 6.8, 6.9, 6.12, 6.13, and 6.15 show that the variables converge to the desired states as defined in Tables 5.5 and 5.8. Figures 6.10 and 6.11 show the angular velocity and attitude tracking performance (RMSE). Figure 6.14 compares the absolute power of the reaction wheels. Complementary plots for the second slewing case are shown in Appendix E.2.

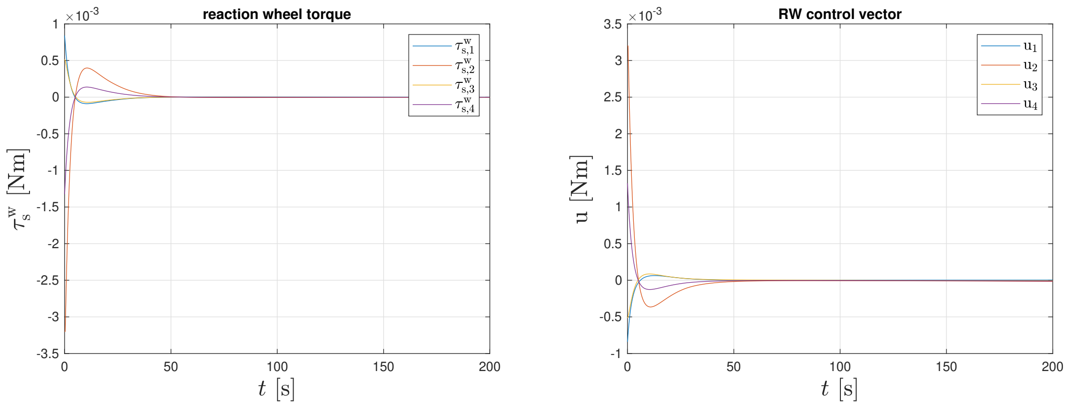

(a) **(b)**

Figure 6.8. – RW torque without / with CGI CA

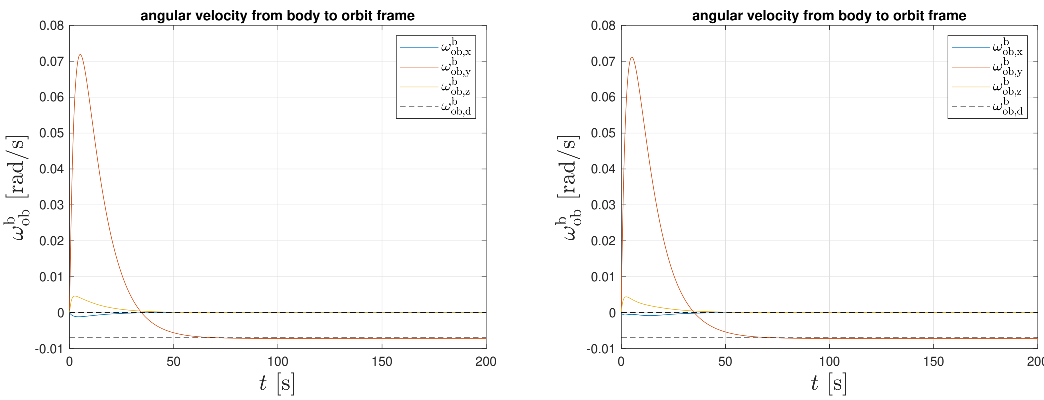

(a) **(b)**

Figure 6.9. – Angular velocity from $\mathcal{F}_b$ to $\mathcal{F}_o$ without / with CGI CA

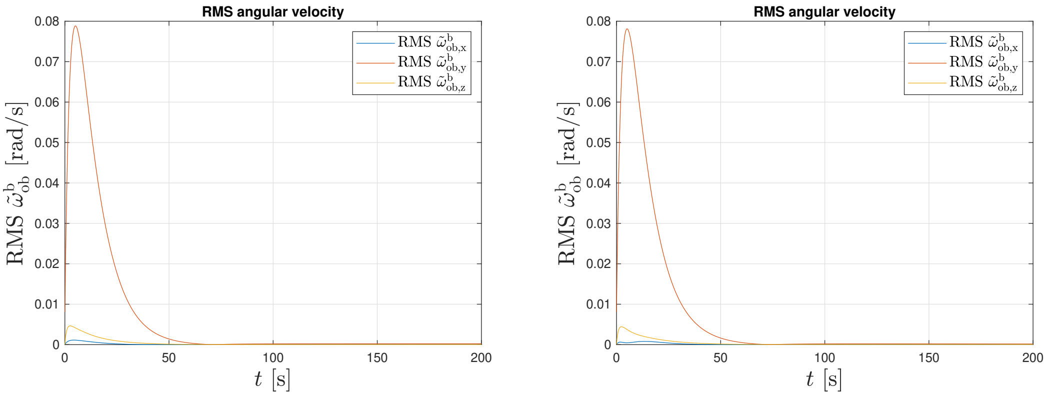

(a) **(b)**

Figure 6.10. – RMS of angular velocity error without / with CGI CA

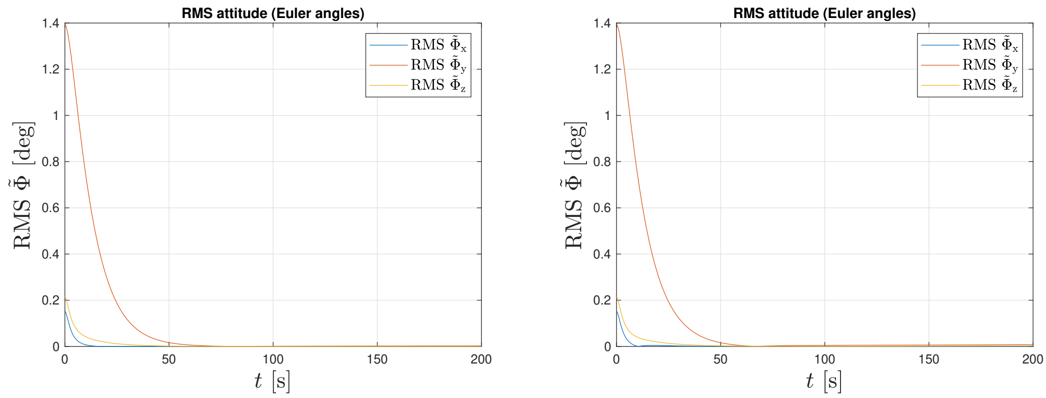

(a) **(b)**

Figure 6.11. – RMS of attitude error in Euler angles without / with CGI CA

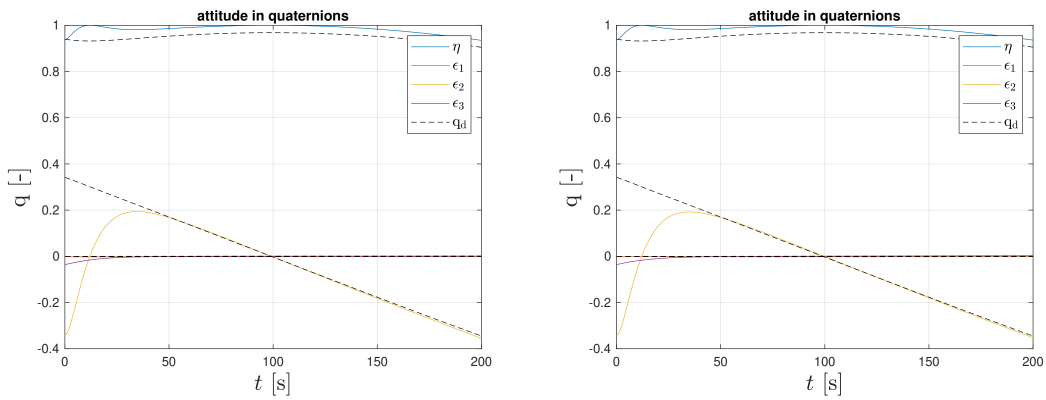

(a) **(b)**

Figure 6.12. – Attitude (quaternions) without / with CGI CA

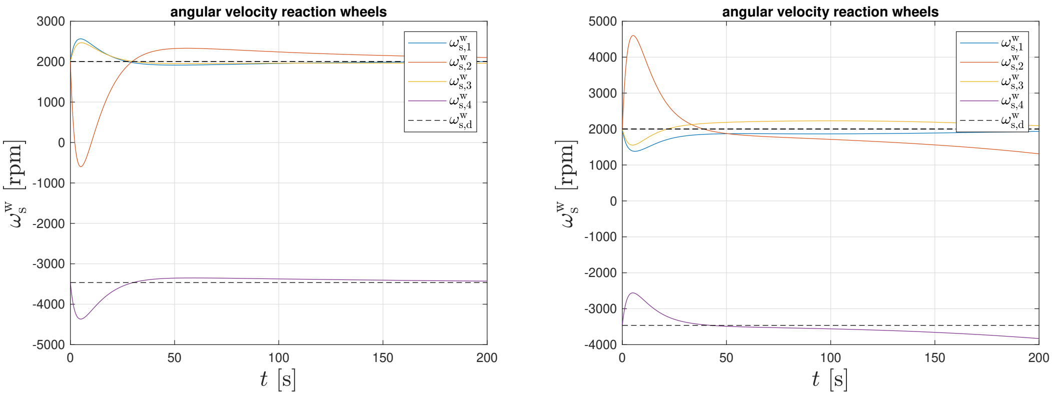

(a) (b)

Figure 6.13. – RW angular velocity without / with CGI CA

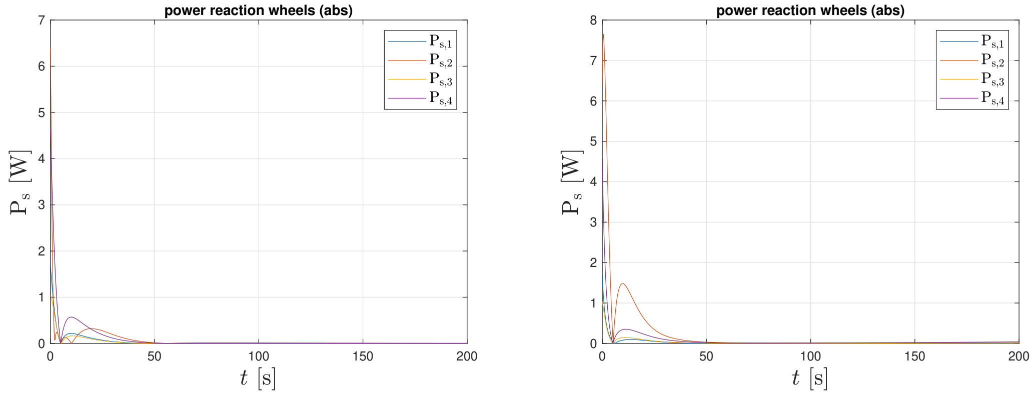

(a) (b)

Figure 6.14. – Power (absolute) without / with CGI CA

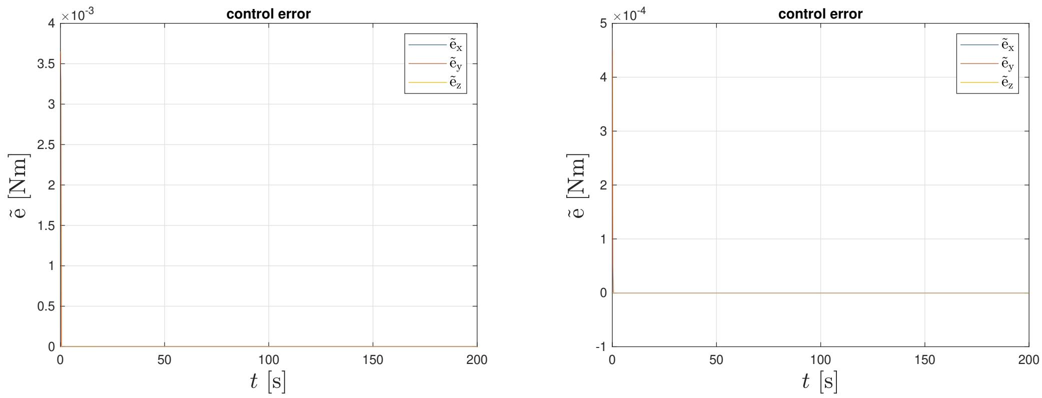

(a) (b)

Figure 6.15. – Control error without / with CGI CA

6.1.3 Comparison for the Ninth Pointing Case

For the ninth pointing case, Figures 6.16, 6.17, 6.19, 6.20, and 6.22 show that the variables converge to the desired states as defined in Tables 5.3 and 5.8. Figure 6.18 compares the attitude tracking performance (RMSE), and Figure 6.21 compares the absolute power of the reaction wheels. Complementary plots for the ninth pointing case are shown in Appendix E.3.

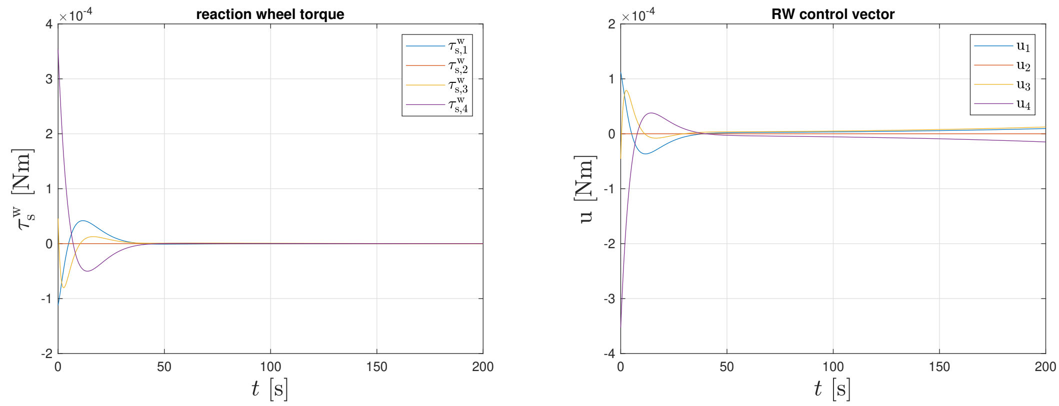

(a) **(b)**

Figure 6.16. – RW torque without / with CGI CA

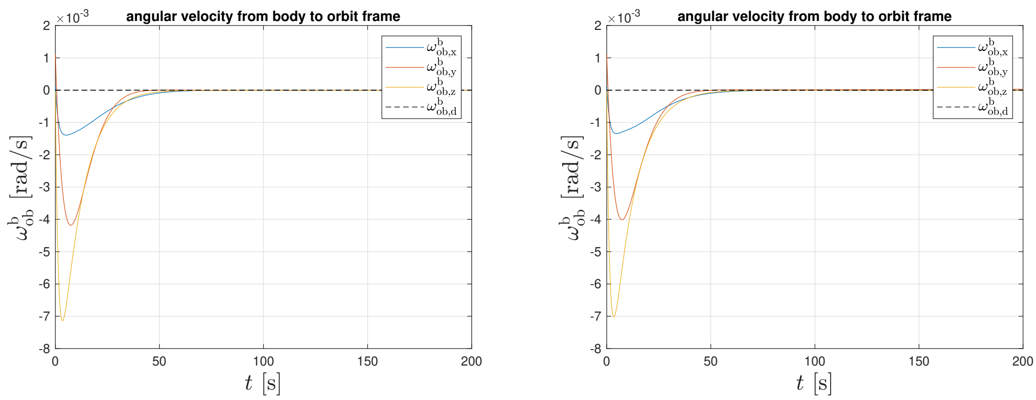

(a) **(b)**

Figure 6.17. – Angular velocity from $\mathcal{F}_b$ to $\mathcal{F}_o$ without / with CGI CA

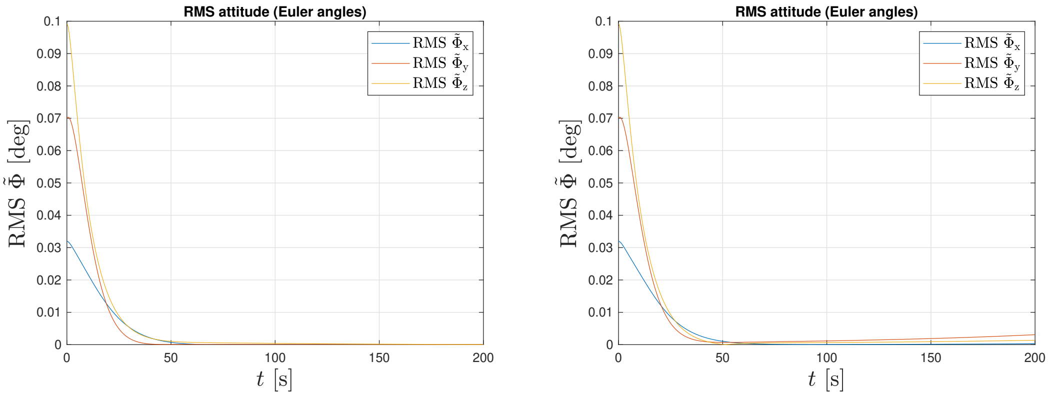

(a) **(b)**

Figure 6.18. – RMS of attitude in Euler angles without / with CGI CA

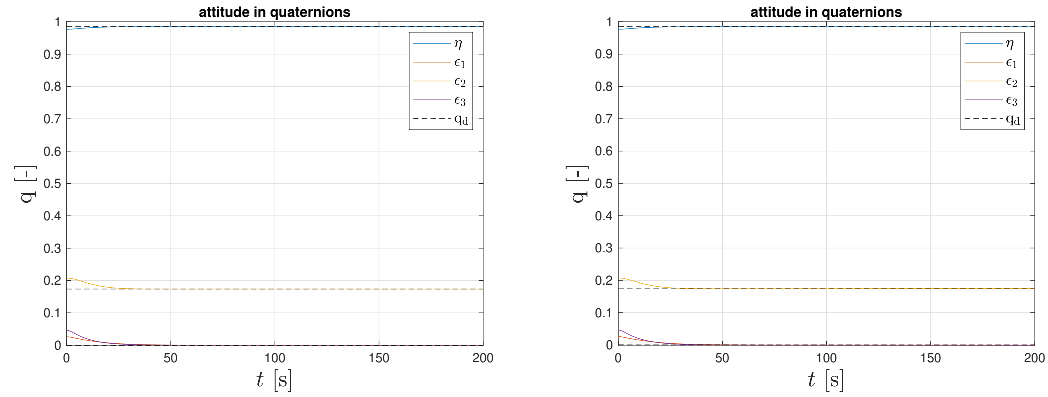

(a) **(b)**

Figure 6.19. – Attitude (quaternions) without / with CGI CA

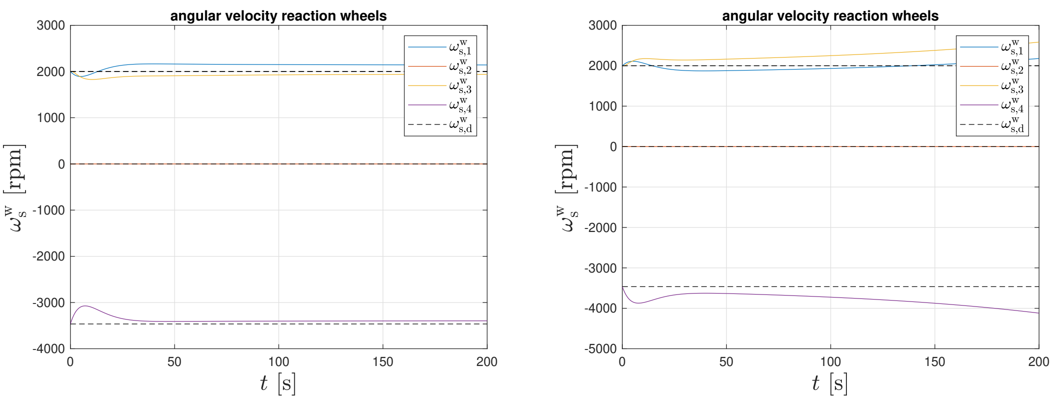

(a) **(b)**

Figure 6.20. – RW angular velocity without / with CGI CA

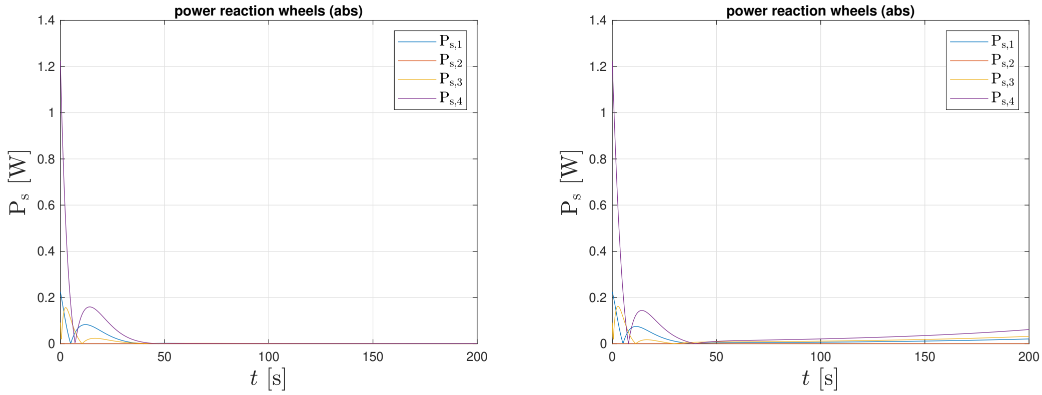

(a) **(b)**

Figure 6.21. – Power (absolute) without / with CGI CA

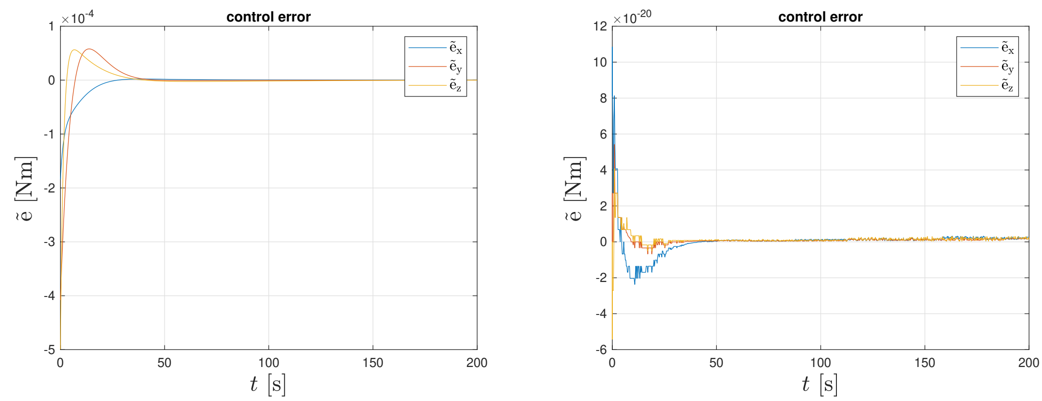

(a) **(b)**

Figure 6.22. – Control error without / with CGI CA

6.1.4 Comparison for the Ninth Slewing Case

For the ninth slewing case, Figures 6.23, 6.24, 6.27, 6.28, and 6.30 show that the variables converge to the desired states as defined in Tables 5.6 and 5.8. Figures 6.25 and 6.26 compare the angular velocity and attitude tracking performance (RMSE). Figure 6.29 compares the absolute power of the reaction wheels. Complementary plots for the ninth slewing case are shown in Appendix E.4.

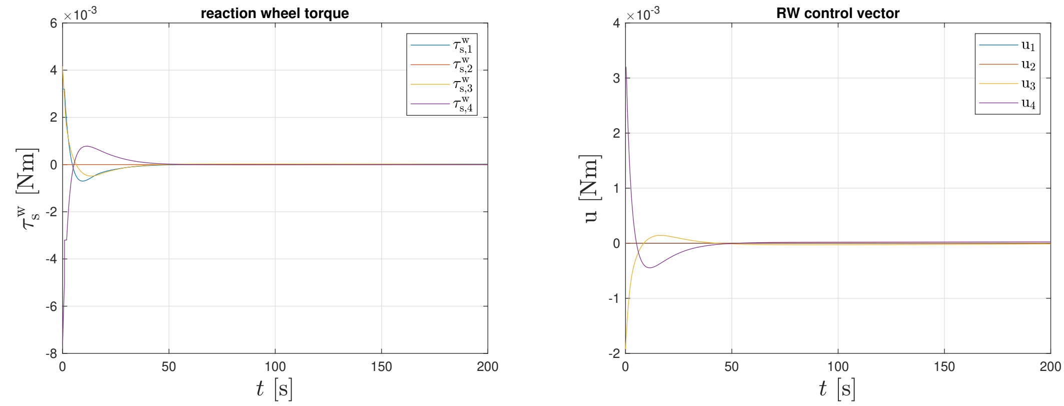

(a) (b)

Figure 6.23. – RW torque without / with CGI CA

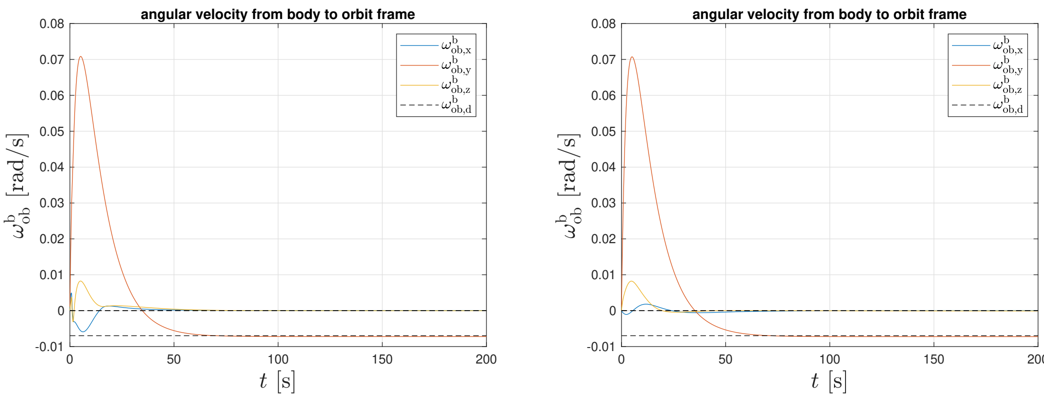

(a) (b)

Figure 6.24. – Angular velocity from $\mathcal{F}_b$ to $\mathcal{F}_o$ without / with CGI CA

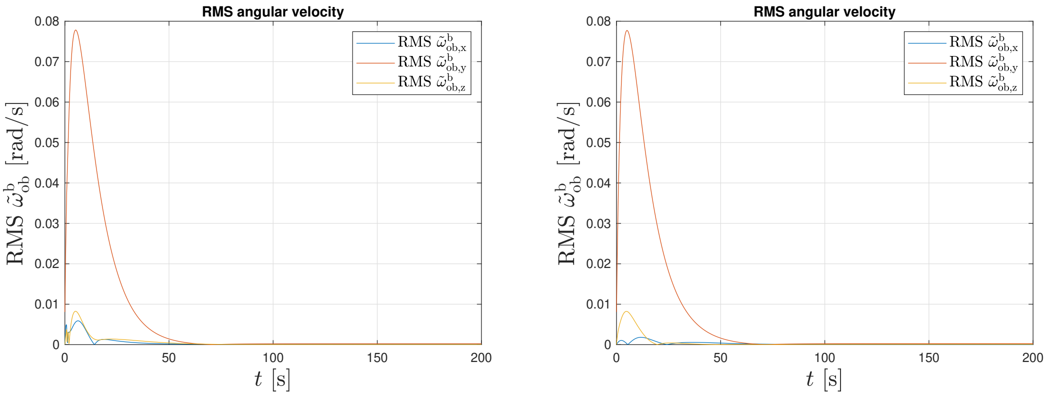

(a) **(b)**

Figure 6.25. – RMS of angular velocity error without / with CGI CA

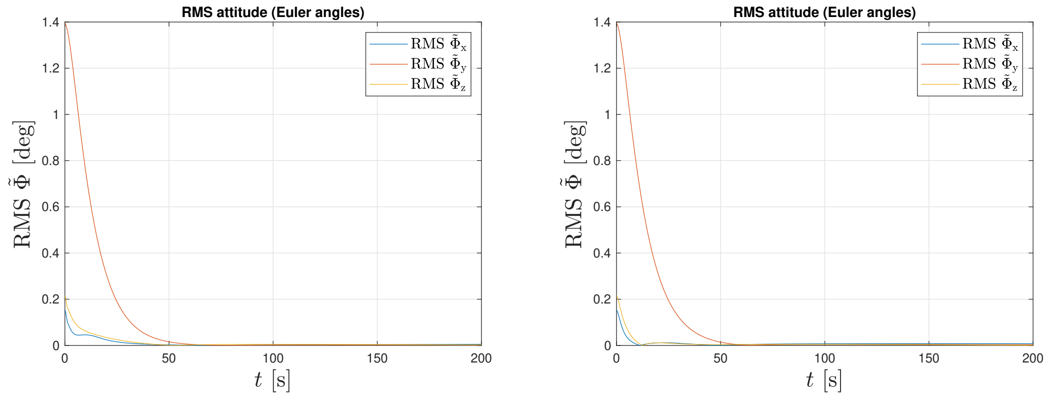

(a) **(b)**

Figure 6.26. – RMS of attitude error in Euler angles without / with CGI CA

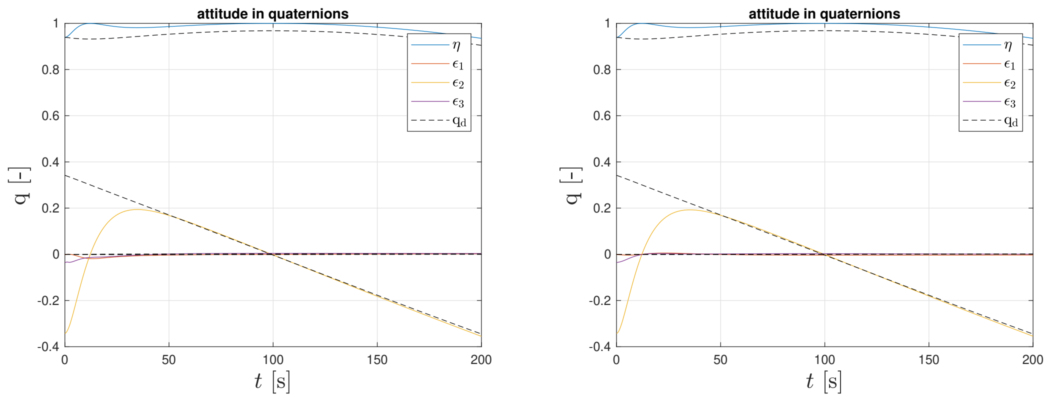

(a) **(b)**

Figure 6.27. – Attitude (quaternions) without / with CGI CA

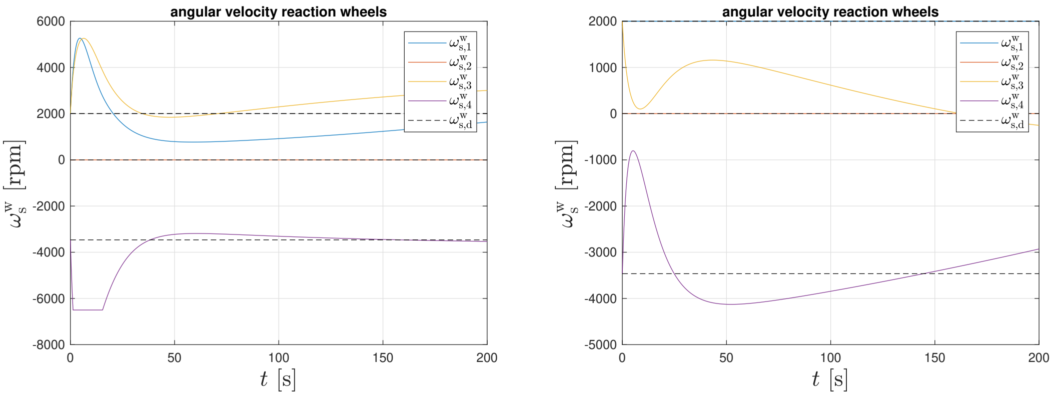

(a) **(b)**

Figure 6.28. – RW angular velocity without / with CGI CA

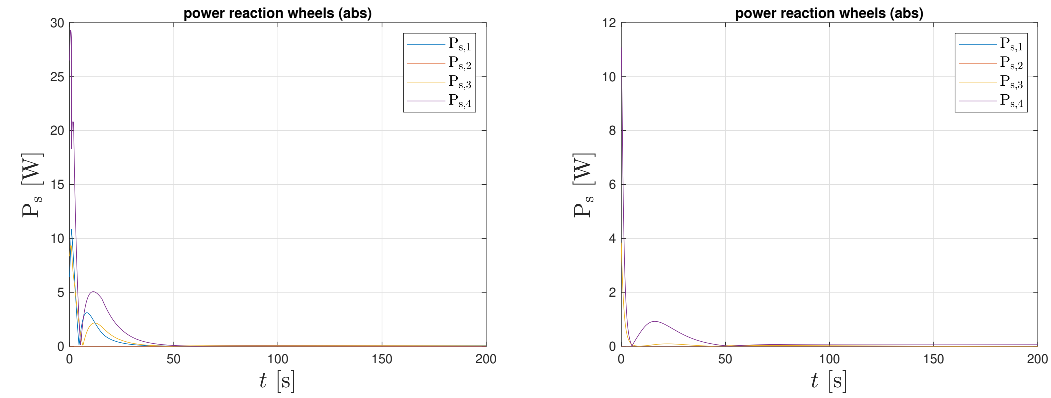

(a) **(b)**

Figure 6.29. – Power (absolute) without / with CGI CA

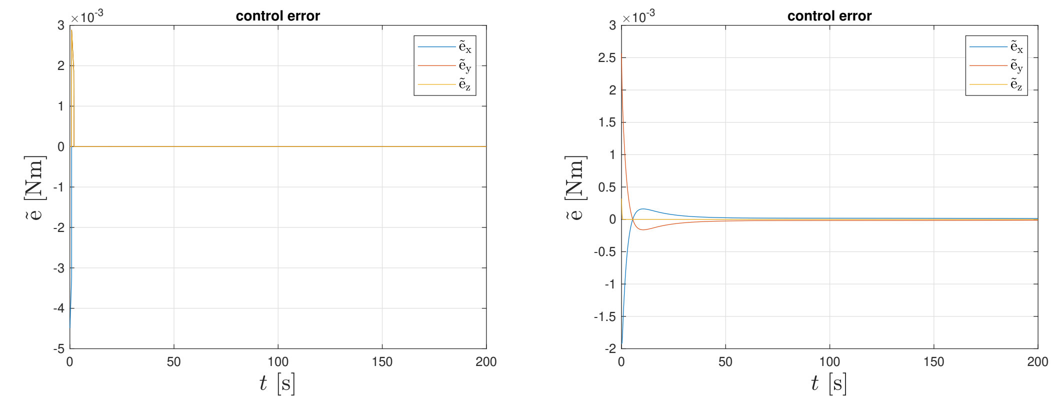

(a) **(b)**

Figure 6.30. – Control error without / with CGI CA

6.2 Simulation Results for Pointing and Slewing Cases With No Full Controllability

6.2.1 Comparison for the Twelfth Pointing Case

For the twelfth pointing case, all plots on the left hand side show chaotic and non-stable properties. Figures 6.31, 6.32, 6.34, 6.35, and 6.37 show that the variables on the right side (modified model) converge to the desired states as defined in Tables 5.4 and 5.8. Figure 6.33 compares the attitude tracking performance (RMSE), and Figure 6.36 compares the absolute power of the reaction wheels. Complementary plots for the twelfth pointing case are shown in Appendix F.1.

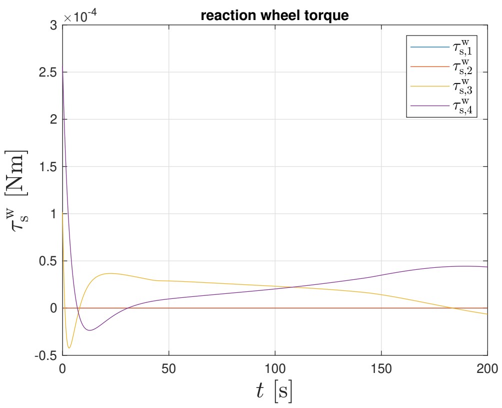

(a)

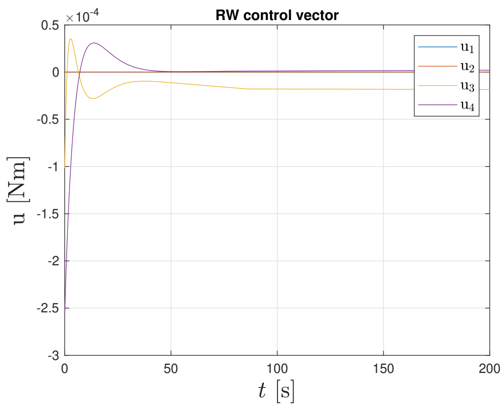

(b)

Figure 6.31. – RW torque without / with CGI CA

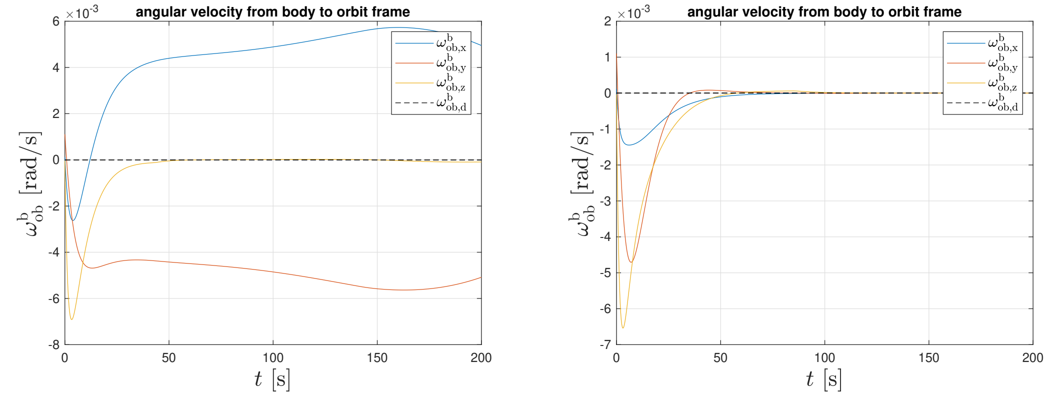

(a) **(b)**

Figure 6.32. – Angular velocity from $\mathcal{F}_b$ to $\mathcal{F}_o$ without / with CGI CA

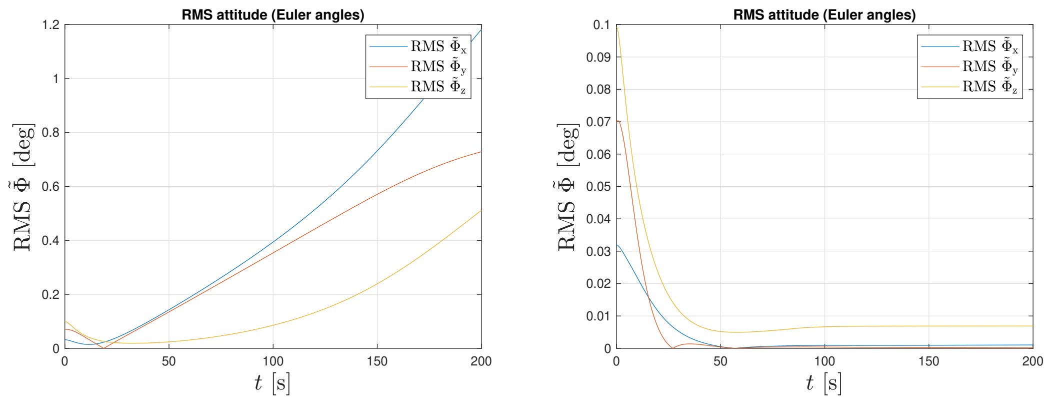

(a) **(b)**

Figure 6.33. – RMS of attitude error in Euler angles without / with CGI CA

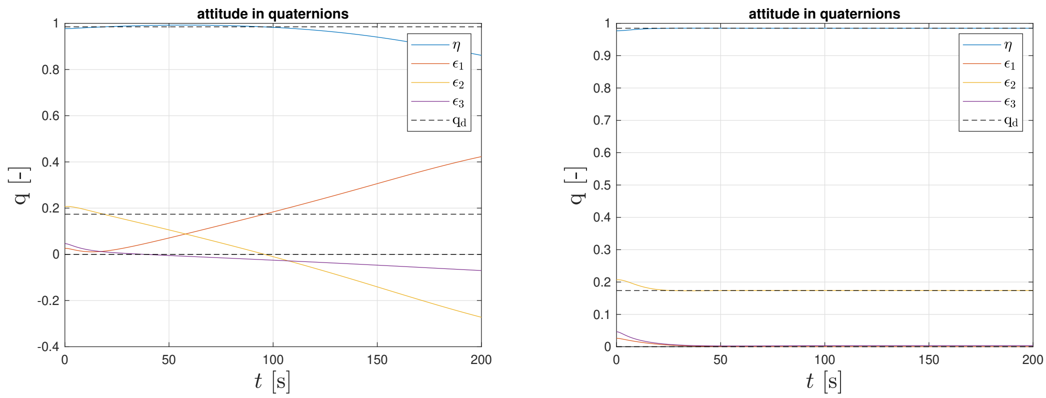

(a) **(b)**

Figure 6.34. – Attitude (quaternions) without / with CGI CA

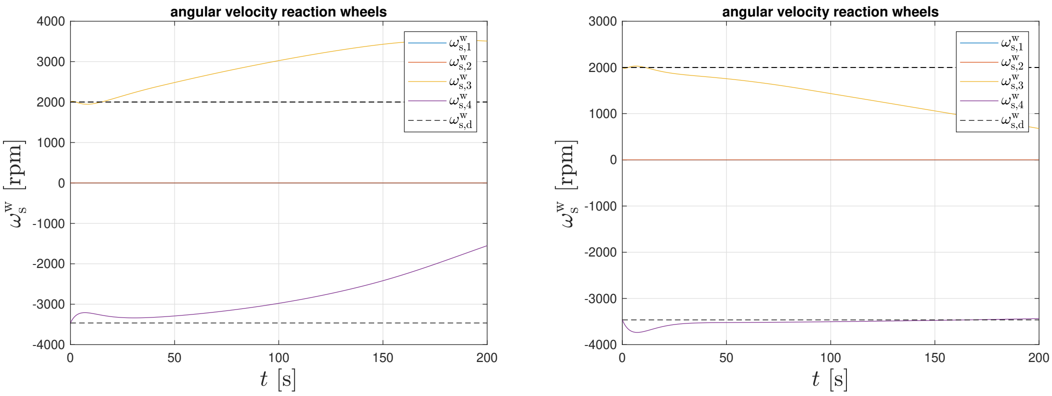

(a) **(b)**

Figure 6.35. – RW angular velocity without / with CGI CA

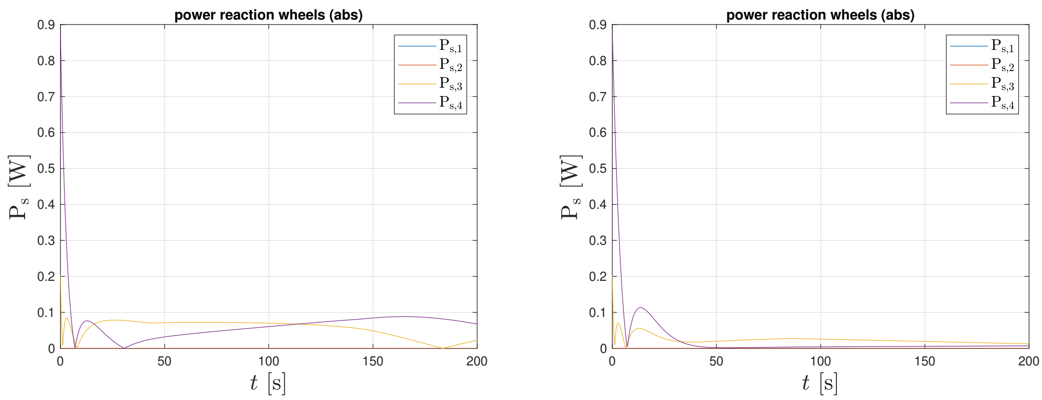

(a) **(b)**

Figure 6.36. – Power (absolute) without / with CGI CA

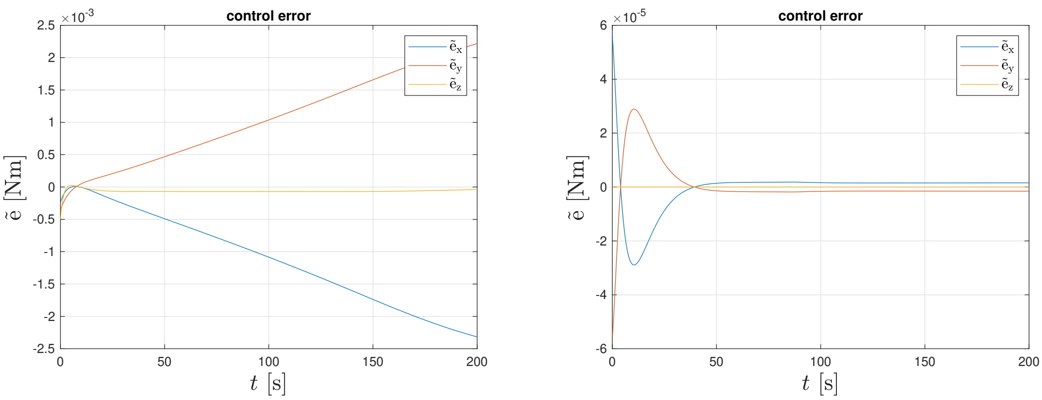

(a) **(b)**

Figure 6.37. – Control error without / with CGI CA

6.2.2 Comparison for the Twelfth Slewing Case

For the twelfth slewing case, all plots on the left hand side show oscillating and non-stable properties. Figures 6.38, 6.39, 6.42, 6.43, and 6.45 show that the variables on the right side converge to the desired states as defined in Tables 5.7 and 5.8. Figures 6.40 and 6.41 compare the angular velocity and attitude tracking performance (RMSE). Figure 6.44 compares the absolute power of the reaction wheels. Complementary plots for the twelfth slewing case are shown in Appendix F.2.

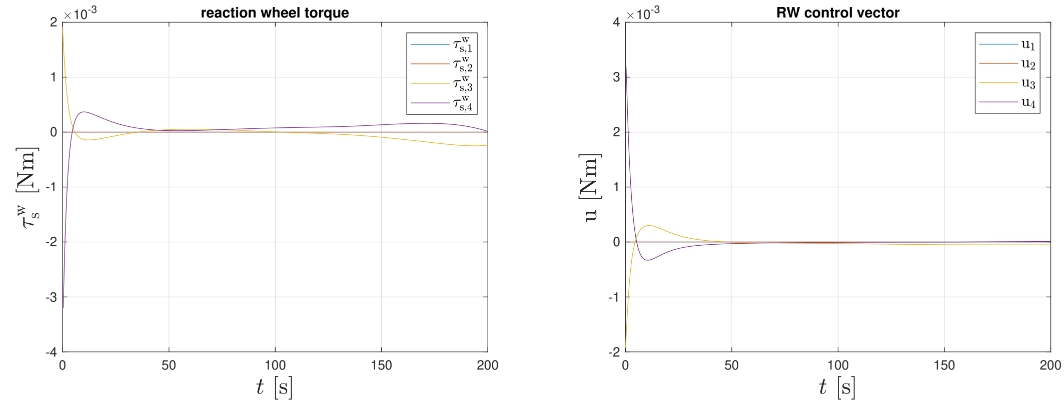

(a) (b)

Figure 6.38. – RW torque without / with CGI CA

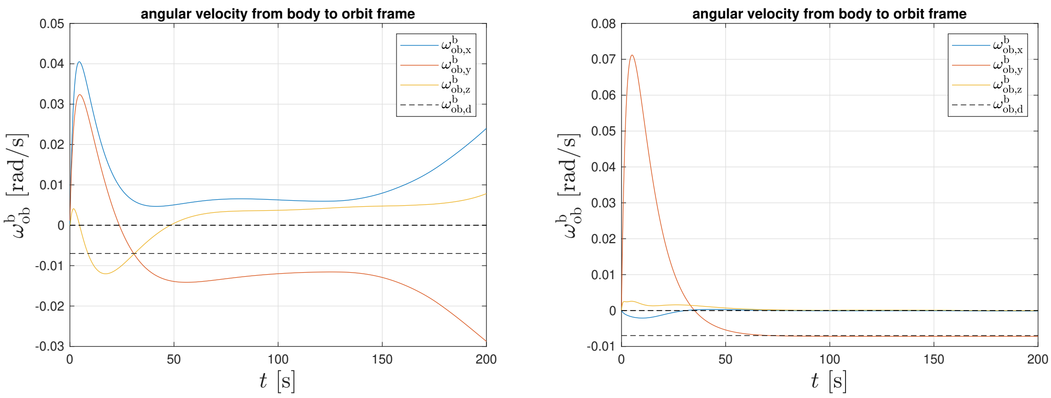

(a) (b)

Figure 6.39. – Angular velocity from $\mathcal{F}_b$ to $\mathcal{F}_o$ without / with CGI CA

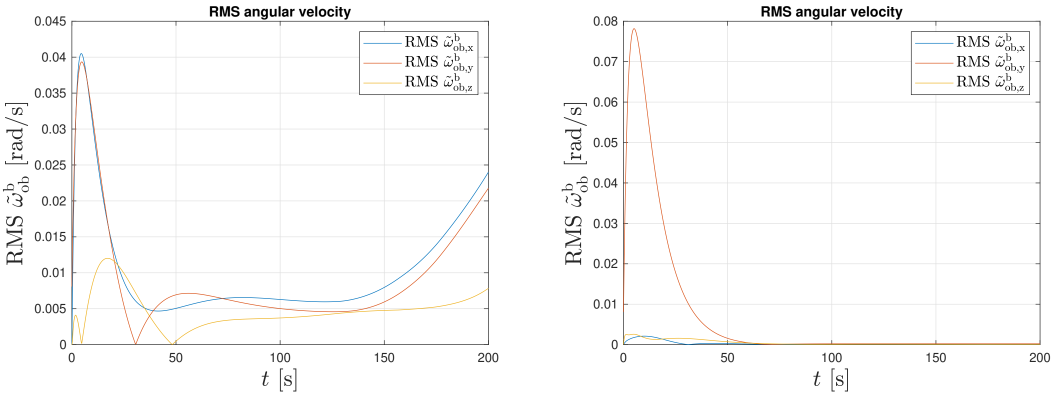

(a) **(b)**

Figure 6.40. – RMS of angular velocity error without / with CGI CA

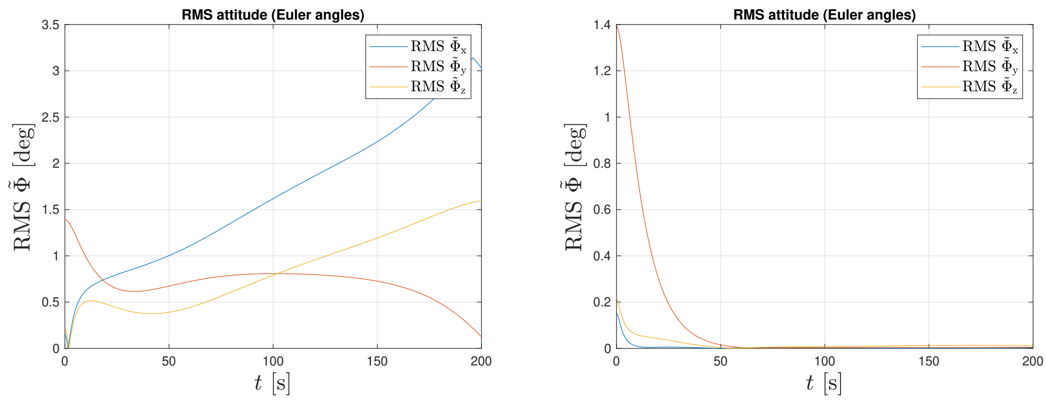

(a) **(b)**

Figure 6.41. – RMS of attitude error in Euler angles without / with CGI CA

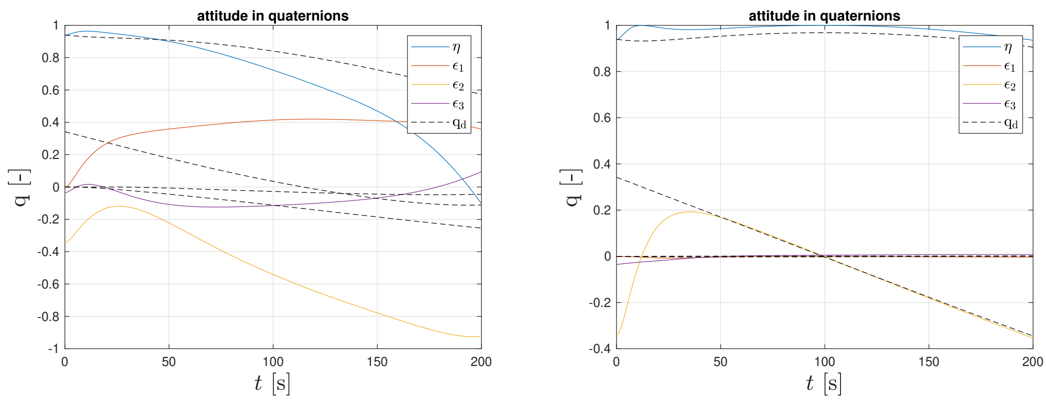

(a) **(b)**

Figure 6.42. – Attitude (quaternions) without / with CGI CA

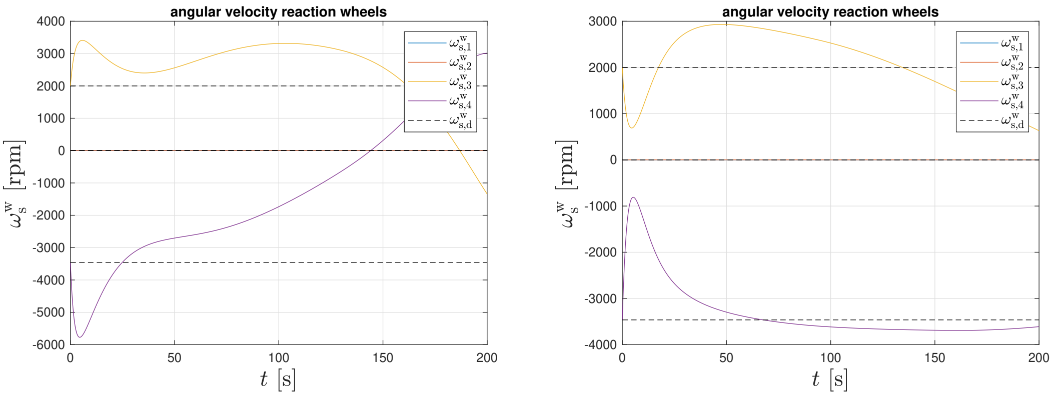

(a) **(b)**

Figure 6.43. – RW angular velocity without / with CGI CA

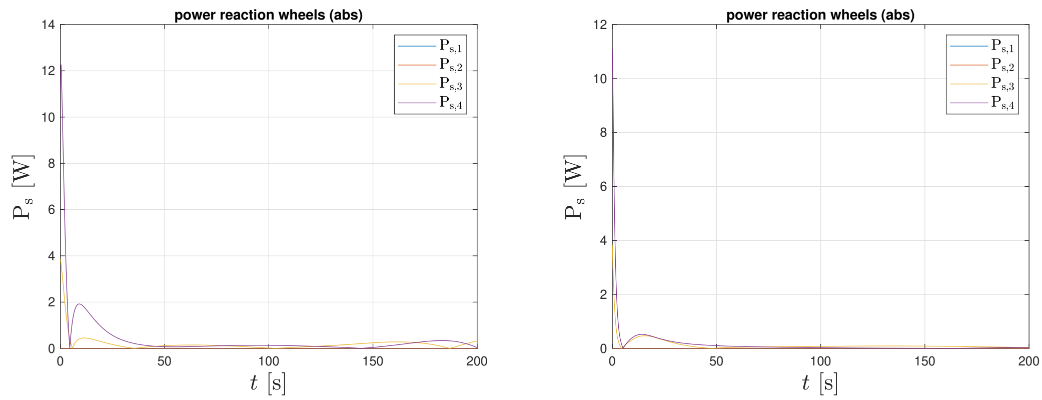

(a) **(b)**

Figure 6.44. – Power (absolute) without / with CGI CA

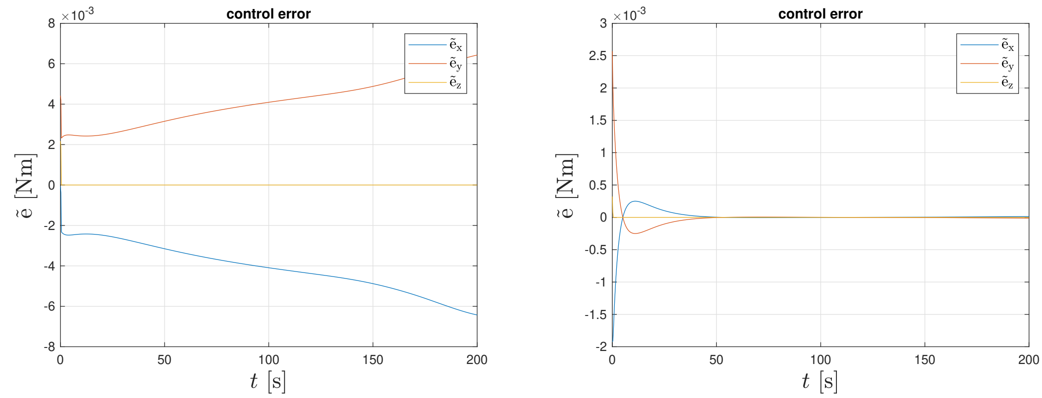

(a) **(b)**

Figure 6.45. – Control error without / with CGI CA

6.2.3 Comparison for the Thirteenth Pointing Case

The plots shown on the left side imply that the system behaves unstable. Figures 6.46, 6.47, 6.49, 6.50, and 6.52 show that the variables on the right side (modified model) converge to the desired states as defined in Tables 5.4 and 5.8. Figure 6.33 compares the attitude tracking performance (RMSE), and Figure 6.51 compares the absolute power of the reaction wheels. Complementary plots for the twelfth slewing case are shown in Appendix F.3.

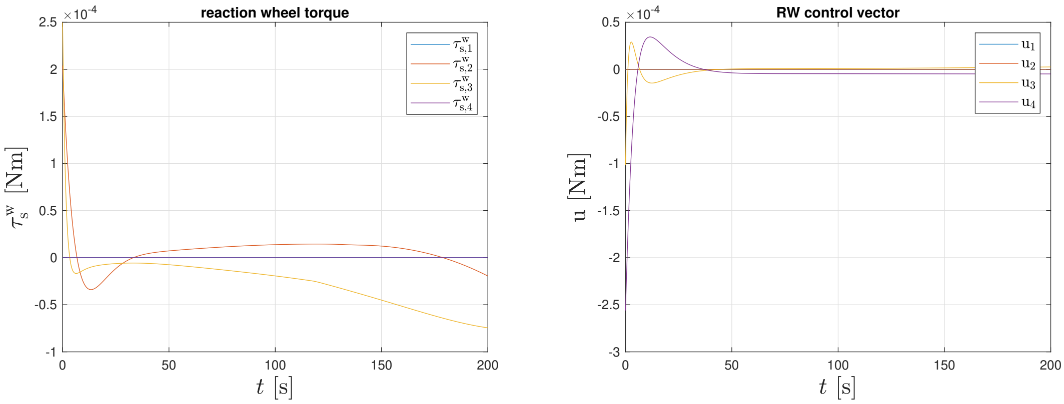

(a) **(b)**

Figure 6.46. – RW torque without / with CGI CA

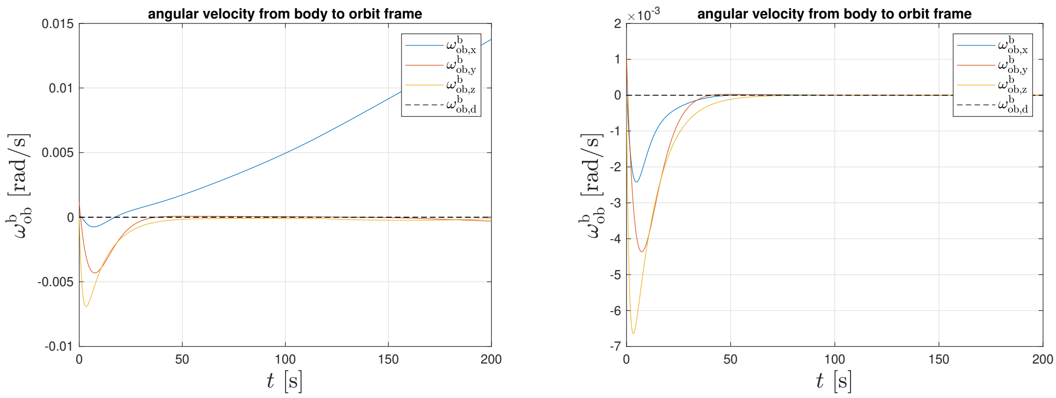

(a) **(b)**

Figure 6.47. – Angular velocity from $\mathcal{F}_b$ to $\mathcal{F}_o$ without / with CGI CA

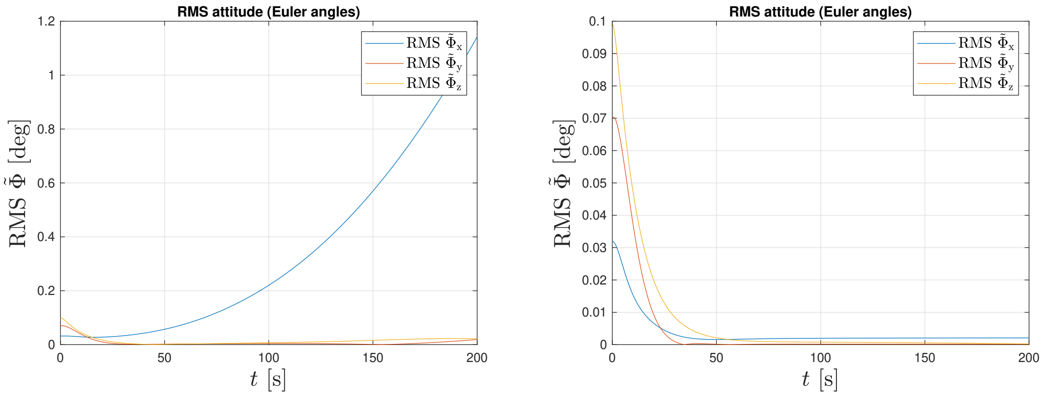

(a) **(b)**

Figure 6.48. – RMS of attitude error in Euler angles without / with CGI CA

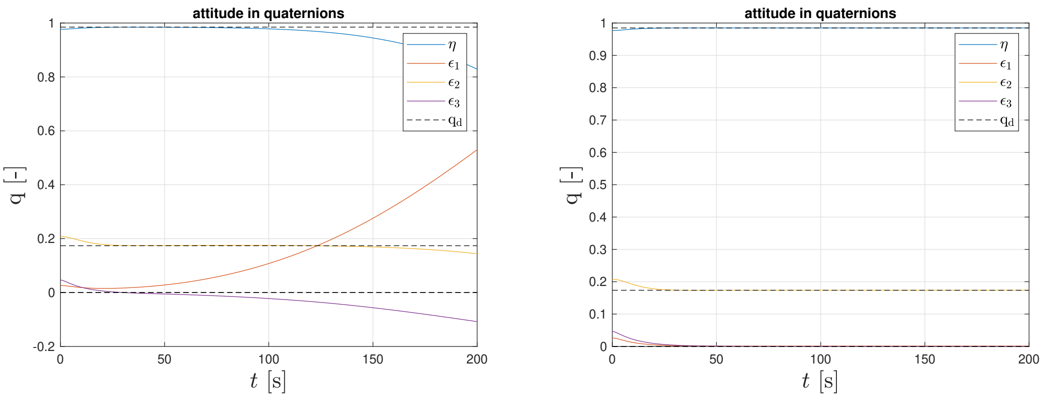

(a) **(b)**

Figure 6.49. – Attitude (quaternions) without / with CGI CA

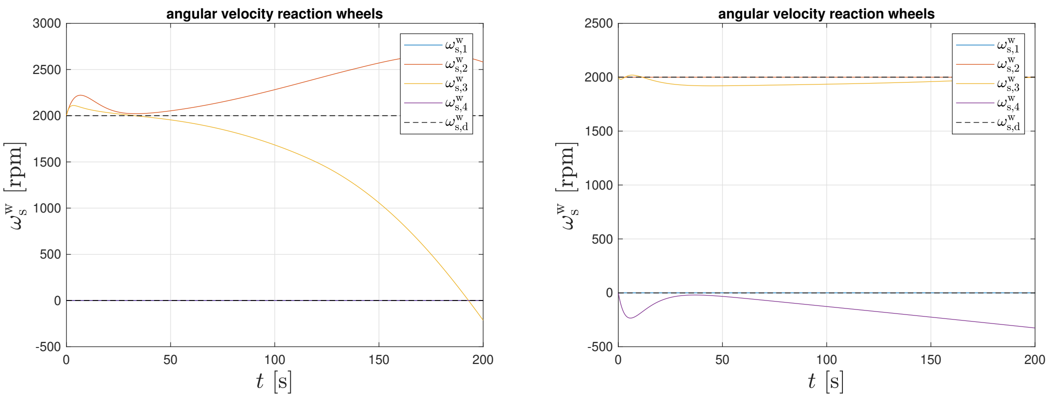

(a) **(b)**

Figure 6.50. – RW angular velocity without / with CGI CA

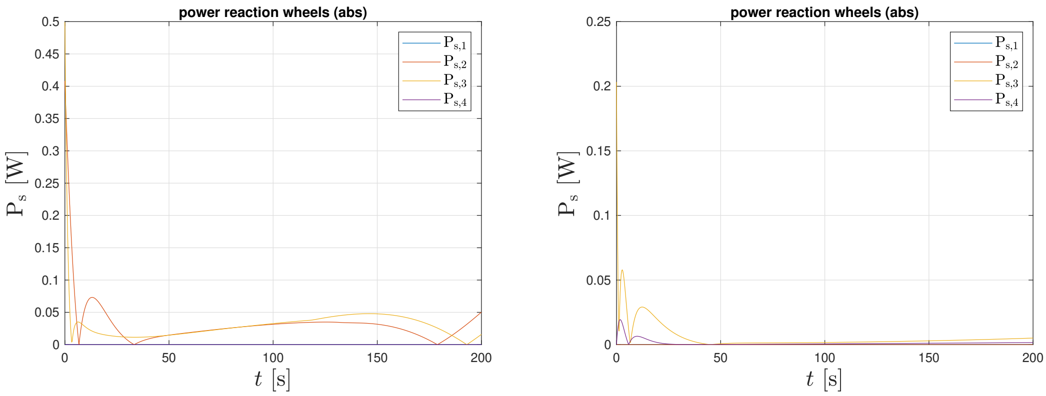

(a) **(b)**

Figure 6.51. – Power (absolute) without / with CGI CA

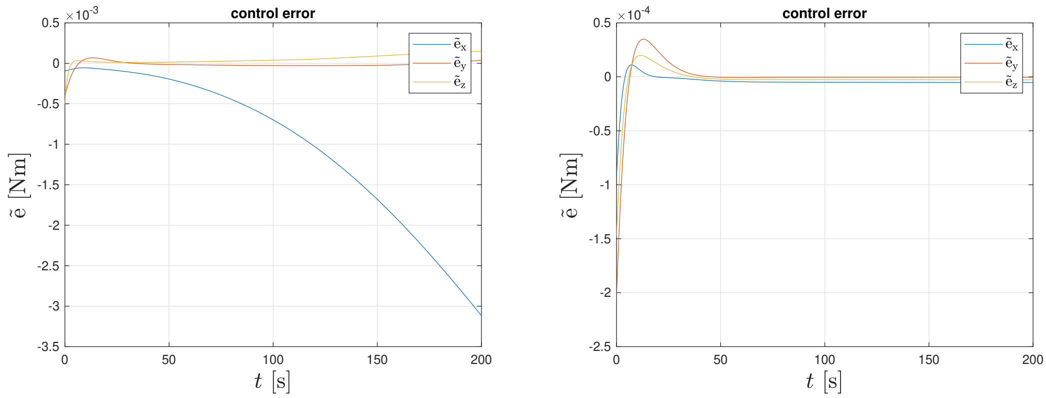

(a) **(b)**

Figure 6.52. – Control error without / with CGI CA
4

6.2.4 Comparison for the Thirteenth Slewing Case

The plots shown on the left side imply that the system behaves unstable. Figures 6.53, 6.54, 6.57, 6.58, and 6.60 show that the variables on the right side converge to the desired states as defined in Tables 5.7 and 5.8. Figures 6.55 and 6.56 compare the angular velocity and attitude tracking performance (RMSE). Figure 6.59 compares the absolute power of the reaction wheels.

Complementary plots for the thirteenth slewing case are shown in Appendix F.4.

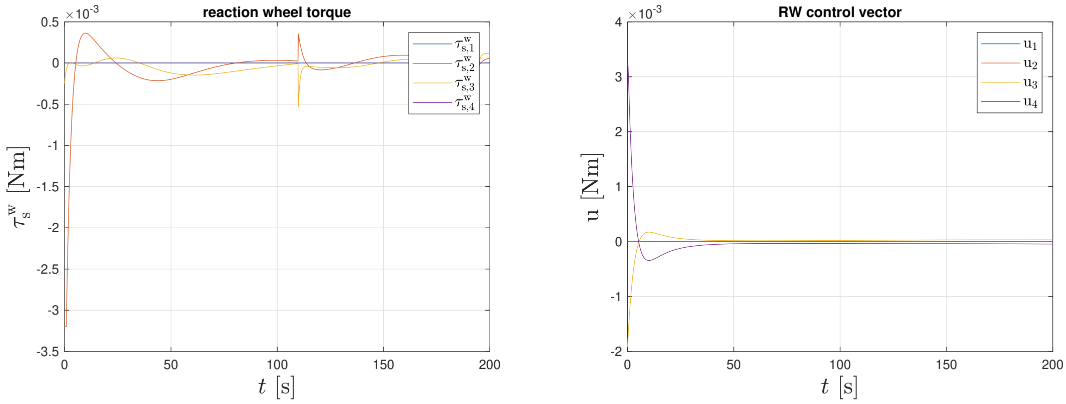

(a) **(b)**

Figure 6.53. – RW torque without / with CGI CA

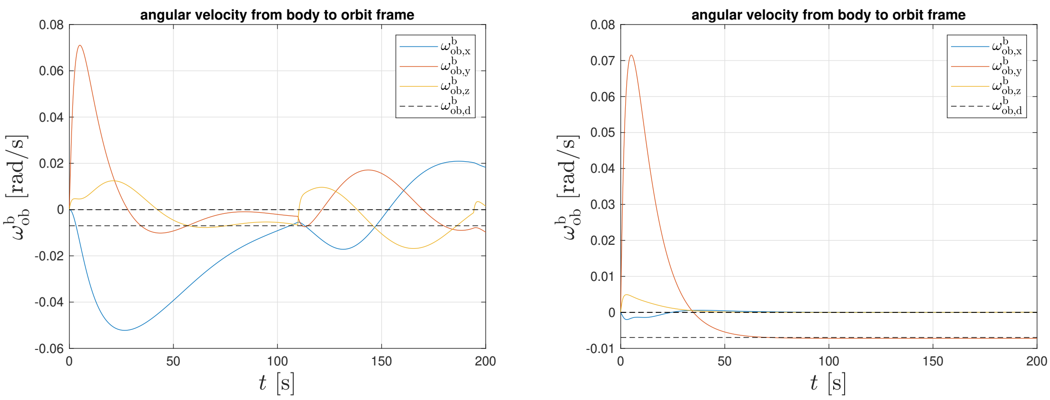

(a) **(b)**

Figure 6.54. – Angular velocity from $\mathcal{F}_b$ to $\mathcal{F}_o$ without / with CGI CA

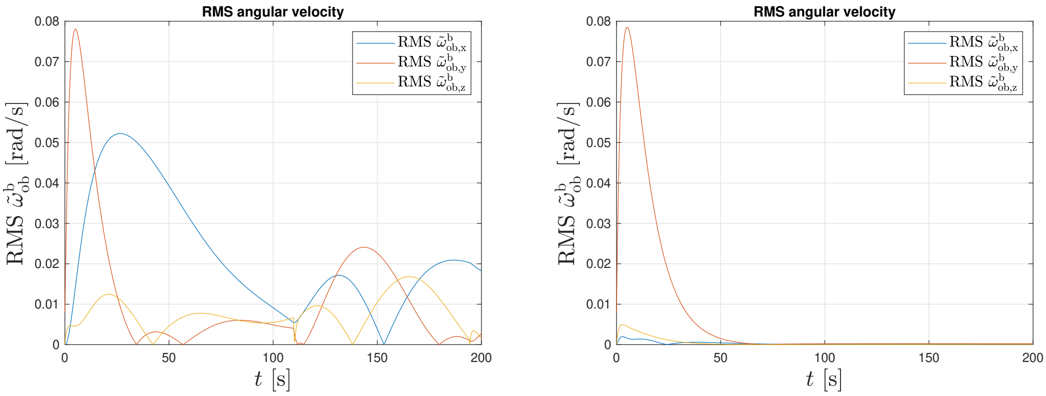

(a) (b)

Figure 6.55. – RMS of angular velocity error without / with CGI CA

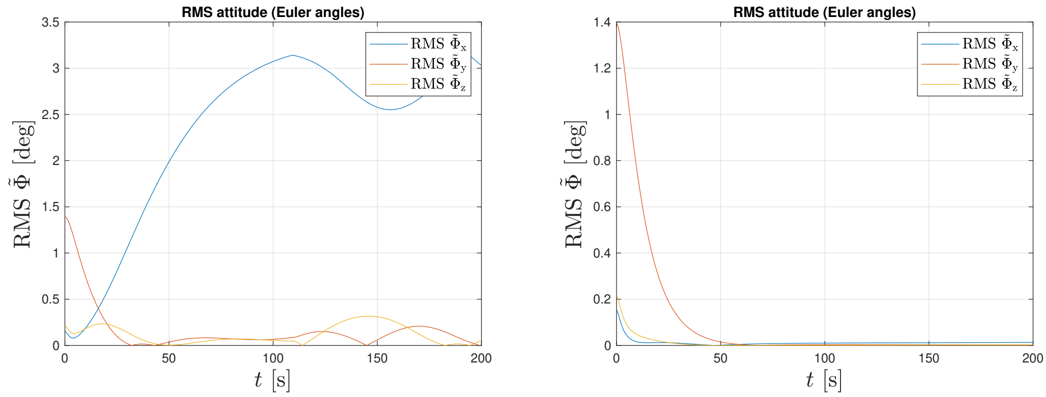

(a) (b)

Figure 6.56. – RMS of attitude error in Euler angles without / with CGI CA

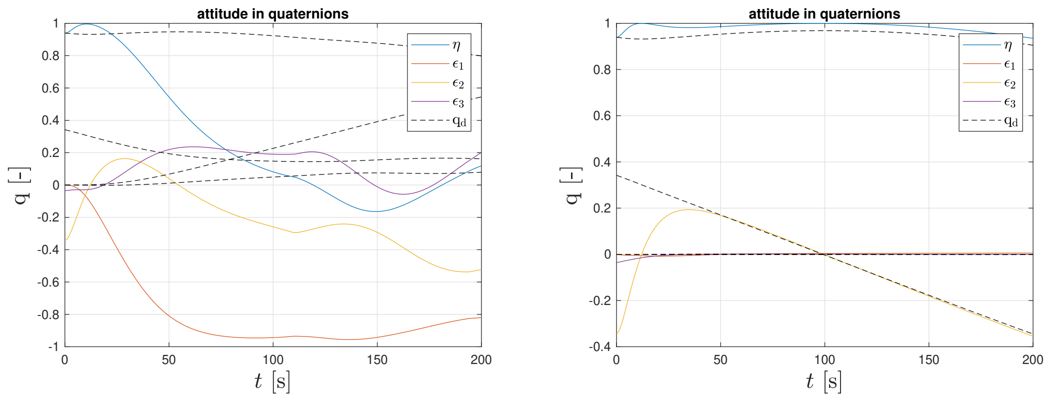

(a) (b)

Figure 6.57. – Attitude (quaternions) without / with CGI CA

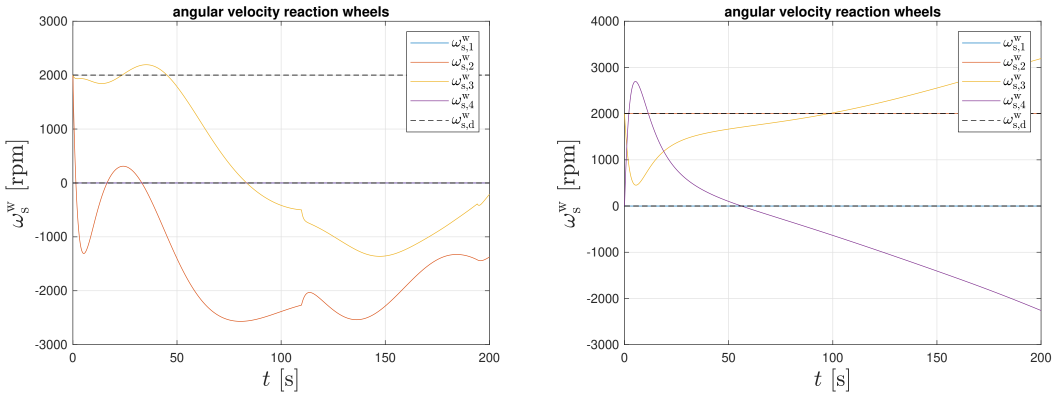

(a) (b)

Figure 6.58. – RW angular velocity without / with CGI CA

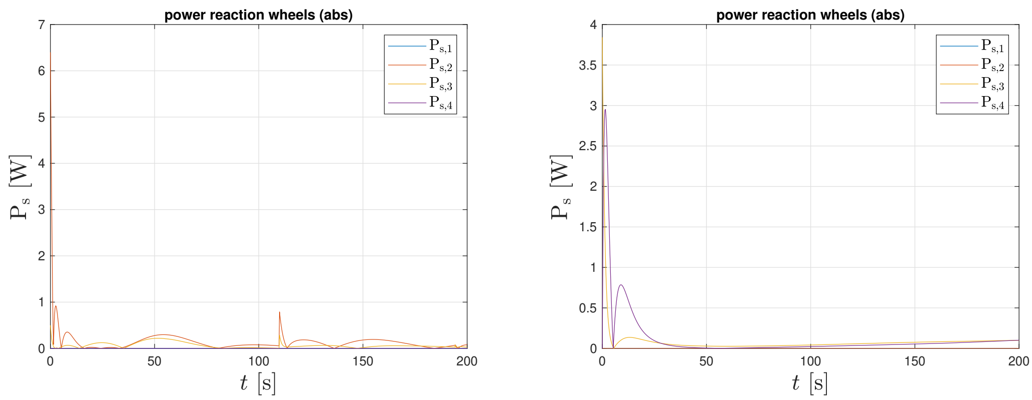

(a) (b)

Figure 6.59. – Power (absolute) without / with CGI CA

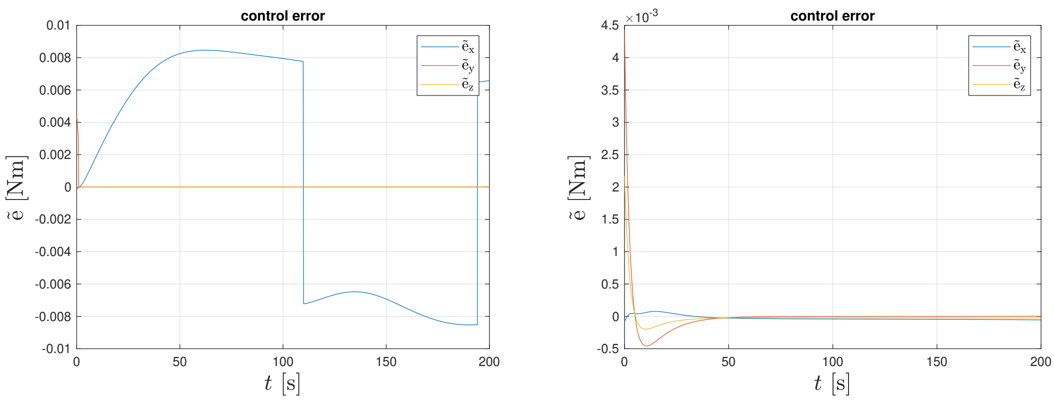

(a) (b)

Figure 6.60. – Control error without / with CGI CA

6.3 Discussion of Results

Here, the results presented in Chapters 6.1 and 6.2 are discussed. For this purpose, tables are created for comparing the performance of both models with respect to $\boldsymbol{\omega}_s^w$, $\boldsymbol{\omega}_{ob}^o$, RMS of $\tilde{\Phi}$, RMS of $\tilde{\boldsymbol{\omega}}_{ob}^b$, $\tilde{\mathbf{e}}$, and the RW power. An "X" marks the model that shows a better performance for the variable of interest. If an "X" is set for both models, then this means that the performance is similarly good.
Table 6.1 shows the evaluation of performance for the second and ninth pointing and slewing cases. It may be concluded that both models perform similarly with respect to the variables of interest. The missing "X" in Table 6.1 may be due to the tuning of the weighting matrices. Table 6.2 shows the evaluation of performance for the attitude cases with no full controllability. Compared to the results in Table 6.1, it can be shown for the attitude cases with no full controllability that the models where CA methods are applied show a significantly better performance with respect to all variables of interest. Deviations can also occur due to not defining an initial state $\mathbf{u}_0$ when using the CGI allocation method. For pointing, the attitude tracking accuracy is strictly smaller than 0.1 °. For slewing, the angular velocity tracking performance is strictly smaller than 0.08 rad/s, and the attitude tracking performance is strictly smaller than 1.4 °. One of the crucial differences lies in minimizing the control error by the CGI allocation method, which converges nicely to zero. Furthermore, it should be mentioned that the number of iterations for all attitude cases for the modified model is one. Thus, the computer had to compute only one generalized inverse until the optimal vector $\mathbf{u} \in \mathbb{R}^{\mathrm{r}}$ was found. Moreover, all solutions calculated by the CGI algorithm are feasible in the sense of Chapter 4.2. It may be assumed that the saturation limit is exceeded on the left side for a longer simulation time, and the solution is no more feasible.
It should be noted that here only cases with a certain degree of controllability are presented. What remains to show are numerical simulations for attitude cases without controllability, e.g., when all but one reaction wheel fail. It remains to be seen whether CA would be suitable for this case since something is being allocated that does not exist.

criteria	original model	CGI CA
	Pointing - Case 2	
$\boldsymbol{\omega}_{\mathrm{s}}^{w}$	X	
$\boldsymbol{\omega}_{ob}^{b}$	X	X
RMS $\tilde{\Phi}$	X	X
$\tilde{\mathbf{e}}$	X	X
RW power	X	
	Slewing - Case 2	
$\boldsymbol{\omega}_{\mathrm{s}}^{w}$	X	
$\boldsymbol{\omega}_{ob}^{b}$	X	X
RMS $\tilde{\Phi}$	X	X
RMS $\tilde{\boldsymbol{\omega}}_{ob}^{b}$	X	X
$\tilde{\mathbf{e}}$	X	X
RW power	X	
	Pointing - Case 9	
$\boldsymbol{\omega}_{\mathrm{s}}^{w}$	X	
$\boldsymbol{\omega}_{ob}^{b}$	X	X
RMS $\tilde{\Phi}$	X	X
$\tilde{\mathbf{e}}$	X	X
RW power	X	
	Slewing - Case 9	
$\boldsymbol{\omega}_{\mathrm{s}}^{w}$	X	
$\boldsymbol{\omega}_{ob}^{b}$	X	X
RMS $\tilde{\Phi}$	X	X
RMS $\tilde{\boldsymbol{\omega}}_{ob}^{b}$	X	X
$\tilde{\mathbf{e}}$	X	X
RW power	X	

Table 6.1. – Discussion for attitude cases with full controllability

criteria	**original model**	**CGI CA**
Pointing - Cases 12 and 13		
$\boldsymbol{\omega}_s^w$		X
$\boldsymbol{\omega}_{ob}^b$		X
RMS $\tilde{\Phi}$		X
$\tilde{\mathbf{e}}$		X
RW power		X
Slewing - Cases 12 and 13		
$\boldsymbol{\omega}_s^w$		X
$\boldsymbol{\omega}_{ob}^b$		X
RMS $\tilde{\Phi}$		X
RMS $\tilde{\boldsymbol{\omega}}_{ob}^b$		X
$\tilde{\mathbf{e}}$		X
RW power		X

Table 6.2. – Discussion for attitude cases with no full controllability

Chapter 7

Conclusions and Future Work

7.1 Findings

For the definition of the CA problem, the reaction wheel torque $\boldsymbol{\tau}_{\mathrm{s}}^{w}$ was applied as the (optimal) control vector $\mathbf{u}$ to be calculated. An $\mathcal{L}_2$-norm is used to determine how good the solution or approximation $\mathbf{u}$ is. By the configuration of weight matrices, the distribution of reaction wheel torques can be affected. It is shown that the CGI allocation method, which is referred to as computationally efficient, performs very well for attitude cases when a reduced rank of the system is given. The primary objective of CA, to minimize the control error $\tilde{\mathbf{e}}$, is fulfilled. It is shown that the CA method applied does not make sense in the attitude cases when the system is characterized by full controllability.

7.2 Future Work

Applying other CA methods for attitude cases with no full controllability is an area of interest for future research. It would be interesting to investigate whether the CGI allocation method also performs well compared to other CA methods. For example, other CA methods could remove some degrees of freedom and render the CL system not being fully controllable. Another field of research in the future could be investigating the composition of the RWA and the particular role of the fourth reaction wheel tilted.

Bibliography

[1] B. A. Kristiansen, "Nonlinear attitude control of a pointing and slewing spacecraft," M.S. thesis, Norwegian University of Science and Technology, 2019.

[2] B. A. Kristiansen, M. E. Grøtte, and J. T. Gravdahl, "Quaternion-based generalized super-twisting algorithm for spacecraft attitude control," 2020, submitted.

[3] J. A. Olsen, "Attitude determination and control system testbed for hardware and software testing and verification for small satellites," M.S. thesis, Norwegian University of Science and Technology, 2021.

[4] S. K. Schanning, "Maximum hands-off control for attitude control of a spacecraft," M.S. thesis, Norwegian University of Science and Technology, 2021.

[5] M. E. Grøtte, R. Birkeland, E. Honoré-Livermore, *et al.*, "Ocean color hyperspectral remote sensing with high resolution and low latency–the hypso-1 cubesat mission," *IEEE Transactions on Geoscience and Remote Sensing*, pp. 1–19, 2021. DOI: `10.1109/TGRS.2021.3080175`.

[6] T. A. Johansen and T. I. Fossen, "Control allocation—a survey," *Automatica*, vol. 49, no. 5, pp. 1087–1103, 2013, ISSN: 0005-1098. DOI: `https://doi.org/10.1016/j.automatica.2013.01.035`.

[7] S. H. Almutairi and N. Aouf, "Reconfigurable dynamic control allocation for aircraft with actuator failures," *The Aeronautical Journal*, vol. 121, no. 1237, pp. 341–371, 2017, ISSN: 0001-9240. DOI: `10.1017/aer.2017.3`.

[8] M. W. Oppenheimer, D. B. Doman, and M. A. Bolender, "Control allocation for over-actuated systems," in *14th Mediterranean Conference on Control and Automation*, 2006, pp. 1–6. DOI: `10.1109/MED.2006.328750`.

[9] H.-D. Wang, J.-Q. Yi, and G.-L. Fan, "Autonomous reconfigurable flight control system design using control allocation," in *2nd International Symposium on Systems and Control in Aerospace and Astronautics*, 2008, pp. 1–6. DOI: `10.1109/ISSCAA.2008.4776188`.

[10] W. C. Durham, "Constrained control allocation," *Journal of Guidance, Control, and Dynamics*, vol. 16, no. 4, pp. 717–725, 1993. DOI: `10.2514/3.21072`.

[11] M. Bodson, "Evaluation of optimization methods for control allocation," *Journal of Guidance, Control, and Dynamics*, vol. 25, no. 4, pp. 703–711, 2002. DOI: `10.2514/2.4937`.

[12] W. C. Durham, "Efficient, near-optimal control allocation," *Journal of Guidance, Control, and Dynamics*, vol. 22, no. 2, pp. 369–372, 1999. DOI: `10.2514/2.4390`.

[13] O. Härkegård, "Dynamic control allocation using constrained quadratic programming," *Journal of Guidance, Control, and Dynamics*, vol. 27, no. 6, pp. 1028–1034, 2004. DOI: `10.2514/1.11607`.

[14] P. Kolaric, V. G. Lopez, and F. L. Lewis, "Optimal dynamic control allocation with guaranteed constraints and online reinforcement learning," *Automatica*, vol. 122, pp. 1–7, 2020, ISSN: 0005-1098. DOI: `https://doi.org/10.1016/j.automatica.2020.109265`.

[15] H. Yang and Q. Hu, "Research and experiment on dynamic weight pseudo-inverse control allocation for spacecraft attitude control system," in *Chinese Control Conference (CCC)*, 2019, pp. 8200–8205. DOI: `10.23919/ChiCC.2019.8865693`.

[16] J. Stephan and W. Fichter, "Fast exact redistributed pseudoinverse method for linear actuation systems," *IEEE Transactions on Control Systems Technology*, vol. 27, no. 1, pp. 451–458, 2019. DOI: `10.1109/TCST.2017.2765622`.

[17] J. M. Buffington and D. F. Enns, "Lyapunov stability analysis of daisy chain control allocation," *Journal of Guidance, Control, and Dynamics*, vol. 19, no. 6, pp. 1226–1230, 1996, ISSN: 0731-5090. DOI: `10.2514/3.21776`.

[18] O. Härkegård and S. T. Glad, "Resolving actuator redundancy—optimal control vs. control allocation," *Automatica*, vol. 41, no. 1, pp. 137–144, 2005, ISSN: 00051098. DOI: `10.1016/j.automatica.2004.09.007`.

[19] T. I. Fossen, *Handbook of Marine Craft Hydrodynamics and Motion Control.* John Wiley & Sons, Ltd, 2011, ISBN: 9781119994138. DOI: `10.1002/9781119994138`.

[20] V. Badescu, *International Handbook of Space Technology.* Springer, 2014, ISBN: 978-3-642-41101-4.

[21] M. E. Grøtte, J. T. Gravdahl, T. A. Johansen, *et al.*, "Spacecraft attitude and angular rate tracking using reaction wheels and magnetorquers," *21st IFAC World Congress*, vol. 53, no. 2, pp. 14 819–14 826, 2020, ISSN: 2405-8963. DOI: `https://doi.org/10.1016/j.ifacol.2020.12.1924`.

[22] O. Egeland and J. T. Gravdahl, *Modeling and simulation for automatic control*, 2nd ed. Marine Cybernetics AS, 2003, ISBN: 8292356010.

[23] A. B. Younes, D. Mortari, J. D. Turner, *et al.*, "Attitude error kinematics," *Journal of Guidance, Control, and Dynamics*, vol. 37, no. 1, pp. 330–336, 2014, ISSN: 0731-5090. DOI: 10.2514/1.60928.

[24] F. L. Markley and J. L. Crassidis, Eds., *Fundamentals of Spacecraft Attitude Determination and Control.* Springer, 2014, ISBN: 978-1-4939-0801-1. DOI: 10.1007/978-1-4939-0802-8.

[25] E. Oland and R. Schlanbusch, "Reaction wheel design for cubesats," in *4th International Conference on Recent Advances in Space Technologies*, 2009, pp. 778–783, ISBN: 978-1-4244-3626-2. DOI: 10.1109/RAST.2009.5158296.

[26] J.-Y. Wen and K. Kreutz-Delgado, "The attitude control problem," *IEEE Transactions on Automatic Control*, vol. 36, no. 10, pp. 1148–1162, 1991, ISSN: 00189286. DOI: 10.1109/9.90228.

[27] W. H. Steyn, "Near-minimum-time eigenaxis rotation maneuvers using reaction wheels," *Journal of Guidance, Control, and Dynamics*, vol. 18, no. 5, pp. 1184–1189, 1995, ISSN: 0731-5090. DOI: 10.2514/3.21523.

[28] N. A. Chaturvedi, A. K. Sanyal and N. H. McClamroch, "Rigid-body attitude control," *IEEE Control Systems*, vol. 31, no. 3, pp. 30–51, 2011, ISSN: 1066-033X. DOI: 10.1109/MCS.2011.940459.

[29] T. R. Krogstad, "Attitude control of satellites in clusters," M.S. thesis, Norwegian University of Science and Technology, 2005.

[30] J. T. Gravdahl, "Three axis attitude determination and control system for a picosatellite: Design and implementation," in *54th International Astronautical Congress of the International Astronautical Federation, the International Academy of Astronautics, and the International Institute of Space Law*, 2003. DOI: 10.2514/6.IAC-03-A.5.07.

[31] J. T. Gravdahl, "Magnetic attitude control for satellites," in *43rd IEEE Conference on Decision and Control*, 2004, pp. 261–266, ISBN: 0-7803-8682-5. DOI: 10.1109/CDC.2004.1428640.

[32] G. Lavezzi, M. E. Grøtte, and M. Ciarcia, "Attitude control strategies for an imaging cubesat," in *IEEE International Conference on Electro Information Technology*, 2019, pp. 149–155, ISBN: 978-1-7281-0927-5. DOI: 10.1109/EIT.2019.8833806.

[33] R. Schlanbusch, R. Kristiansen, and P. J. Nicklasson, "On choosing quaternion equilibrium point in attitude stabilization," in *2010 IEEE Aerospace Conference*, 2010, pp. 1–6. DOI: `10.1109/AERO.2010.5446731`.

[34] S. P. Bhat and D. S. Bernstein, "A topological obstruction to global asymptotic stabilization of rotational motion and the unwinding phenomenon," in *Proceedings of the 1998 American Control Conference. ACC (IEEE Cat. No.98CH36207)*, IEEE, 26.06.1998 - 26.06.1998, 2785–2789 vol.5, ISBN: 0-7803-4530-4. DOI: `10.1109/ACC.1998.688361`.

[35] H. D. Curtis, "Chapter 10 - satellite attitude dynamics," in *Orbital Mechanics for Engineering Students*, 3rd ed., Butterworth-Heinemann, 2014, pp. 543–617, ISBN: 978-0-08-097747-8. DOI: `https://doi.org/10.1016/B978-0-08-097747-8.00010-4`.

[36] T. R. Krogstad, J. T. Gravdahl, and R. Kristiansen, "Coordinated control of satellites: The attitude case," in *Proceedings of the International Astronautical Congress*, 2005, pp. 3282–3290.

[37] F. L. Markley, R. G. Reynolds, F. X. Liu, *et al.*, "Maximum torque and momentum envelopes for reaction wheel arrays," *Journal of Guidance, Control, and Dynamics*, vol. 33, no. 5, pp. 1606–1614, 2010, ISSN: 0731-5090. DOI: `10.2514/1.47235`.

[38] J. Trégouët, D. Arzelier, D. Peaucelle, *et al.*, "Reaction wheels desaturation using magnetorquers and static input allocation," *IEEE Transactions on Control Systems Technology*, vol. 23, no. 2, pp. 525–539, 2015. DOI: `10.1109/TCST.2014.2326037`.

[39] N. Rouche, P. Habets, and M. Laloy, *Stability Theory by Liapunov's Direct Method*, ser. Applied Mathematical Sciences. 1977, vol. 22, ISBN: 978-1-4684-9362-7.

[40] W. Hahn, *Stability of Motion*, ser. Die Grundlehren der mathematischen Wissenschaften, in Einzeldarstellungen mit besonderer Berücksichtigung der Anwendungsgebiete. 1967, vol. 138, ISBN: 978-3-642-50085-5.

[41] V. Andriano, "Global feedback stabilization of the angular velocity of a symmetric rigid body," *Systems & Control Letters*, vol. 20, no. 5, pp. 361–364, 1993, ISSN: 01676911. DOI: `10.1016/0167-6911(93)90014-W`.

[42] D. Aeyels and M. Szafranski, "Comments on the stabilizability of the angular velocity of a rigid body," *Systems & Control Letters*, vol. 10, no. 1, pp. 35–39, 1988, ISSN: 01676911. DOI: `10.1016/0167-6911(88)90037-0`.

[43] M. Nelson and W. Durham, "Comparison of two methods used to deal with saturation of multiple, redundant aircraft control effectors," in *AIAA Atmospheric Flight Mechanics Conference and Exhibit*, American Institute of Aeronautics and Astronautics, 2002, ISBN: 978-1-62410-107-6. DOI: `10.2514/6.2002-4498`.

[44] S. R. Crews, "Increasing slew performance of reaction wheel attitude control systems," M.S. thesis, Naval Postgraduate School, 2013.

[45] D. S. Bernstein, *Matrix Mathematics : Theory, Facts, and Formulas*, 2nd ed. Princeton University Press, 2009, ISBN: 9780691140391.

[46] A. Ben-Israel and T. N. Greville, *Generalized Inverses*, 2nd ed. Springer-Verlag, 2003, ISBN: 0-387-00293-6. DOI: `10.1007/b97366`.

[47] NTNU. (2021). "Ntnu-smallsat-adcs," [Online]. Available: `https://github.com/NTNU-SmallSat-ADCS` (visited on 06/25/2021).

[48] T. I. Fossen. (2018). "Marine systems simulator (mss) toolbox," [Online]. Available: `https://github.com/cybergalactic/MSS/tree/master/GNC` (visited on 05/19/2021).

[49] O. Härkegård. (2004). "Quadratic programming control allocation toolbox for matlab," [Online]. Available: `http://research.harkegard.se/qcat/index.html` (visited on 05/19/2021).

[50] H. D. Curtis, "Appendix a - physical data," in *Orbital Mechanics for Engineering Students*, 3rd ed., Butterworth-Heinemann, 2014, pp. 721–722, ISBN: 978-0-08-097747-8. DOI: `https://doi.org/10.1016/B978-0-08-097747-8.15001-7`.

[51] ——, "Chapter 2 - the two-body problem," in *Orbital Mechanics for Engineering Students*, 3rd ed., Butterworth-Heinemann, pp. 59–144, ISBN: 978-0-08-097747-8. DOI: `https://doi.org/10.1016/B978-0-08-097747-8.00002-5`.

[52] B. O. Sunde and J. T. Gravdahl, "Attitude determination for the student satellite ncube ii," in *56th International Astronautical Congress of the International Astronautical Federation, the International Academy of Astronautics, and the International Institute of Space Law*, Reston, Virigina: American Institute of Aeronautics and Astronautics, 10172005. DOI: `10.2514/6.IAC-05-C1.P.04`.

[53] R. Birkeland and O. Gutteberg, "Overview of the nuts cubesat project," vol. 2, 2014.

[54] T. B. Rinnan, "Development and comparison of estimation methods for attitude determination," M.S. thesis, Norwegian University of Science and Technology, 2012.

Appendices

Appendix A

Matrix Mathematics

A.1 Key Features of a Matrix

A.1.1 Range, Rank, and Null Space

The range of a matrix $\mathbf{A} \in \mathbb{R}^{\mathrm{n}\times\mathrm{r}}$ is denoted by $\mathcal{R}(\mathbf{A})$, and it is defined as

$$\mathcal{R}(\mathbf{A}) = \{\mathbf{Ax}, \mathbf{x} \in \mathbb{R}^{\mathrm{r}}\} \tag{A.1}$$

$\mathcal{R}(\mathbf{A})$ is a subspace of $\mathbb{R}^{\mathrm{n}}$, and

$$\mathcal{R}(\mathbf{A}) = \mathrm{span}\{\mathrm{col}_1(\mathbf{A}), \ldots, \mathrm{col}_{\mathrm{r}}(\mathbf{A})\} \tag{A.2}$$

is valid [45, p. 102]. Expressing matrix $\mathbf{A}$ as a function gives $\mathbf{A} : \mathbb{R}^{\mathrm{r}} \rightarrow \mathbb{R}^{\mathrm{n}}$. From this, it follows that $\mathcal{R}(\mathbf{A}) = \mathbf{A}\mathbb{R}^{\mathrm{r}}$ [45, p. 102]. The null space of a matrix $\mathbf{A} \in \mathbb{R}^{\mathrm{n}\times\mathrm{r}}$ is denoted by $\mathcal{N}(\mathbf{A})$. It is defined as

$$\mathcal{N}(\mathbf{A}) = \{\mathbf{x} \in \mathbb{R}^{\mathrm{r}}, \mathbf{Ax} = 0\} \tag{A.3}$$

$\mathcal{N}(\mathbf{A})$ is a subspace of $\mathbb{R}^{\mathrm{r}}$ and it can be written as

$$\mathcal{N}(\mathbf{A}) = \{[\mathrm{row}_1(\mathbf{A})]^\top, \ldots, [\mathrm{row}_{\mathrm{n}}(\mathbf{A})]^\top\}^\perp \tag{A.4}$$

The rank of a matrix $\mathbf{A} \in \mathbb{R}^{\mathrm{n}\times\mathrm{r}}$ is denoted by rank($\mathbf{A}$). It is defined by

$$\mathrm{rank}(\mathbf{A}) = \dim\mathcal{R}(\mathbf{A}) \tag{A.5}$$

where dim is the dimension of the set. The rank equals the number of linearly independent columns of $\mathbf{A}$ over $\mathbb{R}$ [45, p. 104].

A.1.2 Invertibility

For every non-singular matrix $\mathbf{B}$, exists a unique inverse $\mathbf{B}^{-1}$

$$\mathbf{B}\mathbf{B}^{-1} = \mathbf{B}^{-1}\mathbf{B} = \mathbf{I} \qquad \text{[46, p. 1].} \tag{A.6}$$

For rectangular matrices like the control effectiveness matrix, the generalized inverse is built. A matrix $\mathbf{B}$ is referred to as left invertible if there exists a matrix $\mathbf{B}^{\mathrm{L}} \in \mathbb{R}^{\mathrm{r}\times\mathrm{n}}$ that leads to

$$\mathbf{B}^{\mathrm{L}}\mathbf{B} = \mathbf{I}_{\mathrm{r}\times\mathrm{r}} \qquad \text{[45, p. 106], p. 106.} \tag{A.7}$$

A matrix $\mathbf{B}$ is referred to as right invertible if there exists a matrix $\mathbf{B}^{\mathrm{R}} \in \mathbb{R}^{\mathrm{r}\times\mathrm{n}}$ that leads to

$$\mathbf{B}\mathbf{B}^{\mathrm{R}} = \mathbf{I}_{\mathrm{n}\times\mathrm{n}} \qquad \text{[45, p. 106].} \tag{A.8}$$

A.2 Norms

A real-valued continuous function is denoted by $\mathbf{f}(\cdot)$, where $\mathbf{f} : [\mathrm{a}, \mathrm{b}] \to \mathbb{R}^{\mathrm{n}}$. The real-valued function $\mathbf{f}(\mathrm{t}) : [0, \infty) \to \mathbb{R}^{\mathrm{n}}$, where $0 \leq \mathrm{a} < \mathrm{b} < \infty$, is of particular interest. A norm is a topological structure with the concept of the length or size of the set. Depending on the topological structure (metric, norm, or inner product), a metric space, Banach space, or Hilbert space is defined. A real-valued function $\|\mathbf{x}\|$ is a norm on $\mathbf{X}$ if and only if $\forall \mathbf{x} \in \mathbf{X}$. The length function must satisfy the following conditions:

1. The length of an element must always be larger or equal to zero:

$$\|\mathbf{x}\| \geq 0 \quad \text{(positivity).} \tag{A.9}$$

2. The length of an element being zero is equivalent to this being the zero element in the set. Concerning the first condition, this means that all other elements' length

has to be strictly positive:

$$\|\mathbf{x}\| = 0 \Leftrightarrow \mathbf{x} = 0 \quad \text{(positive definiteness)}. \tag{A.10}$$

3. The sum of two elements cannot be larger than the sum of each element's length:

$$\|\mathbf{x} + \mathbf{y}\| \leq \|\mathbf{x}\| + \|\mathbf{y}\| \quad \text{(triangle inequality)}. \tag{A.11}$$

4. Multiplying an element by an arbitrary scalar $\alpha \in \mathbb{R}$, then the result equals the original element's length scaled by the absolute value of α:

$$\|\alpha\mathbf{x}\| = |\alpha|\,\|\mathbf{x}\| \quad \text{(homogeneity)}. \tag{A.12}$$

A.2.1 p-Norms

For the set of all n-dimensional vectors with real-valued components, the lengths of the vectors may be calculated as

$$\|\mathbf{x}\|_{\mathrm{p}} = \left(\sum_{\mathrm{i}=1}^{\mathrm{n}} |x_{\mathrm{i}}|^{\mathrm{p}}\right)^{\frac{1}{\mathrm{p}}}, \ \mathrm{p} \in [1, \infty]. \tag{A.13}$$

For $\mathrm{p} = 2$, the norm is a Euclidean norm, defined as

$$\|\mathbf{x}\|_2 = \sqrt{|x_1|^2 + \ldots + |x_{\mathrm{n}}|^2}. \tag{A.14}$$

For $\mathrm{p} = \infty$, the norm is a maximum norm, defined as

$$\|\mathbf{x}\|_\infty = \max_{\mathrm{i} \in \{1,\ldots,\mathrm{n}\}} |x_{\mathrm{i}}| \tag{A.15}$$

and it represents the largest absolute value. The Banach space is defined as $\left(\mathbb{R}^{\mathrm{n}}, \|\cdot\|_p\right)$. A property of p-norms is that they are all equivalent. This property is helpful if stability proof requires the use of different norms.

A.2.2 $\mathcal{L}_\mathrm{p}$-Norms

The general $\mathcal{L}_\mathrm{p}$-norm is defined as

$$\|\mathrm{f}\|_{\mathcal{L}_\mathrm{p}} = \left(\int_\mathrm{a}^\mathrm{b} |\mathrm{f}(\tau)|^\mathrm{p}\, \mathrm{d}\tau\right)^{\frac{1}{\mathrm{p}}} < \infty \quad , \ \mathrm{p} \in [1, \infty]. \tag{A.16}$$

Remark: The integral must be finite. For $\mathrm{p} = \infty$, the $\mathcal{L}_\infty$-norm is defined as

$$\|\mathrm{f}\|_{\mathcal{L}_\infty} = \sup_{\mathrm{a} \le t \le \mathrm{b}} |\mathrm{f}(\mathrm{t})| \tag{A.17}$$

where the supremum is used because the maximum does not necessarily exist for all sets. The Banach space is defined as $\left(\mathrm{C}[\mathrm{a}, \mathrm{b}], \|\cdot\|_{\mathcal{L}_\mathrm{p}}\right)$. Considering time-varying functions, the $\mathcal{L}_\mathrm{p}$-space is defined as $\left(\mathrm{C}[0, \infty), \|\cdot\|_{\mathcal{L}_\mathrm{p}}\right)$.

Further information on matrix mathematics can be found, for example, in Paper [46, p. 20] or [45].

A.3 Transformation from Quaternions to Euler Angles

The inverse tangent of the four-quadrant of y and x is necessary to calculate the angles ϕ and ψ. According to [19, p. 33], it is defined as

$$\mathrm{atan2}(\mathrm{y},\mathrm{x}) = \begin{cases} \tan^{-1}\left(\dfrac{\mathrm{y}}{\mathrm{x}}\right) & \text{when } \mathrm{x} > 0 \\ \pi + \tan^{-1}\left(\dfrac{\mathrm{y}}{\mathrm{x}}\right) & \text{when } \mathrm{y} \geq 0 \text{ and } \mathrm{x} < 0 \\ -\pi + \tan^{-1}\left(\dfrac{\mathrm{y}}{\mathrm{x}}\right) & \text{when } \mathrm{y} < 0 \text{ and } \mathrm{x} < 0 \\ \dfrac{\pi}{2} & \text{when } \mathrm{y} > 0 \text{ and } \mathrm{x} = 0 \\ -\dfrac{\pi}{2} & \text{when } \mathrm{y} < 0 \text{ and } \mathrm{x} = 0 \\ 0 & \text{when } \mathrm{y} = 0 \text{ and } \mathrm{x} = 0 \end{cases}$$

and it satisfies the limitation $-\pi \leq \mathrm{atan2}(\mathrm{x},\mathrm{y}) \leq \pi$.

The rotation matrix $\mathbf{R}_o^b = \begin{bmatrix}\mathbf{c}_1^b & \mathbf{c}_2^b & \mathbf{c}_3^b\end{bmatrix}^\top = \begin{bmatrix} \mathrm{c}_{1,\mathrm{x}}^b & \mathrm{c}_{2,\mathrm{x}}^b & \mathrm{c}_{3,\mathrm{x}}^b \\ \mathrm{c}_{1,\mathrm{y}}^b & \mathrm{c}_{2,\mathrm{y}}^b & \mathrm{c}_{3,\mathrm{y}}^b \\ \mathrm{c}_{1,\mathrm{z}}^b & \mathrm{c}_{2,\mathrm{z}}^b & \mathrm{c}_{3,\mathrm{z}}^b \end{bmatrix}$ represents the rotation from $\mathcal{F}_o$ to $\mathcal{F}_b$ as calculated in (2.25). From this, the three Euler angles are calculated as

$$\begin{aligned} \phi &= \mathrm{atan2}\left(\mathrm{c}_{2,\mathrm{z}}^b, \mathrm{c}_{3,\mathrm{z}}^b\right) && \text{(A.18)} \\ \theta &= -\sin^{-1}\left(\mathrm{c}_{1,\mathrm{z}}^b\right) = -\tan^{-1}\left(\frac{\mathrm{c}_{1,\mathrm{z}}^b}{\sqrt{1-(\mathrm{c}_{1,\mathrm{z}}^b)^2}}\right), \ \theta \neq \pm 90^\circ && \text{(A.19)} \\ \psi &= \mathrm{atan2}\left(\mathrm{c}_{1,\mathrm{y}}^b, \mathrm{c}_{1,\mathrm{x}}^b\right) \qquad [19, \text{ p. } 33]. && \text{(A.20)} \end{aligned}$$

Appendix B

Orbital Mechanics

B.1 Earth and Orbit Model

Table B.1 shows the physical data used for the Earth and orbit modeling.

Object	Radius (km)	Mass (kg)	Sidereal Rotation Period	Inclination of Equator to Orbit Plane	Semimajor Axis of Orbit (km)	Orbit Eccentricity	Inclination of Orbit to the Ecliptic Plane	Orbit Sidereal Period
Sun	696,000	1.989×10^{30}	25.38 d	7.25°	—	—	—	—
Mercury	2440	330.2×10^{21}	58.65 d	0.01°	57.91×10^{6}	0.2056	7.00°	87.97 d
Venus	6052	4.869×10^{24}	243 d*	177.4°	108.2×10^{6}	0.0067	3.39°	224.7 d
Earth	6378	5.974×10^{24}	23.9345 h	23.45°	149.6×10^{6}	0.0167	0.00°	365.256 d
(Moon)	1737	73.48×10^{21}	27.32 d	6.68°	384.4×10^{3}	0.0549	5.145°	27.322 d
Mars	3396	641.9×10^{21}	24.62 h	25.19°	227.9×10^{6}	0.0935	1.850°	1.881 y
Jupiter	71,490	1.899×10^{27}	9.925 h	3.13°	778.6×10^{6}	0.0489	1.304°	11.86 y
Saturn	60,270	568.5×10^{24}	10.66 h	26.73°	1.433×10^{9}	0.0565	2.485°	29.46 y
Uranus	25,560	86.83×10^{24}	17.24 h*	97.77°	2.872×10^{9}	0.0457	0.772°	84.01 y
Neptune	24,760	102.4×10^{24}	16.11 h	28.32°	4.495×10^{9}	0.0113	1.769	164.8 y
(Pluto)	1195	12.5×10^{21}	6.387 d*	122.5°	5.870×10^{9}	0.2444	17.16°	247.7 y

Retrograde

Table B.1. – Astronomical data for the sun, the planets, and the moon [50, p. 721]

B.2 Reference Frames and Rotation Matrices

B.2.1 Perifocal Frame

For orbit modeling, the perifocal frame, fixed in space and centered at the orbit's focus, is introduced [51, p. 108]. The satellite's orbit position in the perifocal frame is defined as

$$\mathbf{r}_p = \frac{\mathrm{p}}{(1 + \mathrm{e}\cos\nu)}[\cos\nu \quad \sin\nu \quad 0]^\top \tag{B.1}$$

where ν is the true anomaly, an orbital parameter defined in Table B.2, and p is the semi-latus rectum defined in (B.7). Appendix B.3 specifies the parameters describing the orbit. The satellite's orbit velocity in the perifocal frame is defined as

$$\mathbf{v}_p = \sqrt{\frac{\mu}{\mathrm{p}}}\,[-\sin\nu \quad (\mathrm{e} + \cos\nu) \quad 0]^\top \tag{B.2}$$

where μ is the standard gravitational parameter of the Earth, given as $3.986 \cdot 10^{14}\ \mathrm{m}^3/\mathrm{s}^2$.

B.2.2 Rotation from Perifocal Frame to Inertial Frame

The rotation matrix $\mathbf{R}_p^i$ is defined as

$$\mathbf{R}_p^i = \mathbf{R}_p^i(\Omega)\mathbf{R}_p^i(\mathrm{i})\mathbf{R}_p^i(\omega) \tag{B.3}$$

where

$$\begin{aligned}
\mathbf{R}_p^i(\Omega) &= \begin{bmatrix} \cos\Omega & -\sin\Omega & 0 \\ \sin\Omega & \cos\Omega & 0 \\ 0 & 0 & 1 \end{bmatrix}, \quad \mathbf{R}_p^i(\mathrm{i}) = \begin{bmatrix} 1 & 0 & 0 \\ 0 & \cos\mathrm{i} & -\sin\mathrm{i} \\ 0 & 0 & 1 \end{bmatrix}, \quad \text{and} \\
\mathbf{R}_p^i(\omega) &= \begin{bmatrix} \cos\omega & -\sin\omega & 0 \\ \sin\omega & \cos\omega & 0 \\ 0 & 0 & 1 \end{bmatrix}
\end{aligned} \tag{B.4}$$

are the single rotation matrices. Ω, i, and ω are orbital parameters defined in Table B.2.

B.2.3 Rotation from $\mathcal{F}_i$ to $\mathcal{F}_e$

The rotation from $\mathcal{F}_i$ to $\mathcal{F}_e$ is represented by the rotation matrix

$$\mathbf{R}_i^e = \begin{bmatrix} \cos\theta_{\mathrm{G}} & \sin\theta_{\mathrm{G}} & 0 \\ -\sin\theta_{\mathrm{G}} & \cos\theta_{\mathrm{G}} & 0 \\ 0 & 0 & 1 \end{bmatrix} \tag{B.5}$$

where θ_{G} is the Greenwich Mean Sidereal Time (GSMT), representing the displacement of $\mathcal{F}_e$ relative to $\mathcal{F}_i$. The GSMT is defined as $\theta_{\mathrm{G}} = \theta_{\mathrm{G},0} + \omega_{ie}(\mathrm{t} - \mathrm{t}_0)$, where $\theta_{\mathrm{G},0}$ is the GMST at t_0, $\boldsymbol{\omega}_{ie}$ is the angular velocity of $\mathcal{F}_e$ relative to $\mathcal{F}_i$ about the $\hat{\mathbf{z}}$-axis, and t is the sidereal time. ω_{ie} is defined in Chapter 2.1.3.

B.3 Orbital Mechanics

For the mathematical modeling, simplifying assumptions have been made. A two-body problem is assumed, where the mass of satellite m_1 is much smaller than the Earth's mass m_2. The Earth is assumed to be spherical. Therefore, the nadir vector $\hat{\mathbf{z}}_o$ coincides with the line that specifies the satellite's local altitude. A near circular orbit is assumed. The radius to the spacecraft is defined as

$$\mathrm{r} = \mathrm{r_E} + \mathrm{h_o} \tag{B.6}$$

where $\mathrm{r_E}$ is the Earth's radius, given as $6371.2 \cdot 10^3$ [m], and $\mathrm{h_o}$ is the mean altitude of the spacecraft, defined in Chapter 2.1.5. From this, the semi-major axis a and the semi-latus rectum p are calculated as

$$\mathrm{a} = \frac{\mathrm{r}}{(1-\mathrm{e})} \quad \text{and} \quad \mathrm{p} = \mathrm{a}(1-\mathrm{e}^2) \tag{B.7}$$

The orbital parameters are listed in Table B.2.

orbit parameter	**definition**
right ascension of the ascending node	$\Omega = 80\ ^\circ$
inclination	$\mathrm{i} = 97.6\ ^\circ$
argument of perigee	$\omega = 0\ ^\circ$
semi-major axis	$\mathrm{a} = 6.9057 \cdot 10^6$ m
true anomaly	$\Theta = 0\ ^\circ$

Table B.2. – Orbit parameters

Applying Newton's law of universal gravitation gives the gravitational force acting between the Earth and the rigid body

$$\mathbf{F}_\mathrm{g} = \mathrm{G}\mathrm{m}_1\mathrm{m}_2 \frac{\mathbf{r}_{ib}^i}{\left(\left\|\mathbf{r}_{ib}^i\right\|_2\right)^3} \tag{B.8}$$

where G is the gravitational constant, given as $6.6741 \cdot 10^{-11}\ \mathrm{m}^3/\mathrm{kgs}^2$ and $\mathbf{r}_{ib}^i$ is the satellite's inertial position defined in (2.4). The mass of the HYPSO is given as $\mathrm{m}_1 = 6.8$ kg and the mass of the Earth is given as $\mathrm{m}_2 = 5.9722 \cdot 10^{24}$ kg. The Earth's gravitational constant μ can be calculated as

$$\mu = \mathrm{G}(\mathrm{m}_1 + \mathrm{m}_2) \qquad\qquad [51,\ \text{p. } 82]. \tag{B.9}$$

Newton's second law is given as $\mathbf{F} = \frac{\mathrm{d}^i}{\mathrm{dt}}\mathrm{m}\mathbf{v}_{ib}^i$, where $\mathbf{v}_{ib}^i = \frac{\mathrm{d}^i}{\mathrm{dt}}\mathbf{r}_{ib}^i$. Thus, the satellite's orbital motion can be written as

$$\frac{\mathrm{d}^i}{\mathrm{dt}}\mathbf{v}_{ib}^i = \mathbf{a}_{ib}^i = \mu \frac{\mathbf{r}_{ib}^i}{\left(\left\|\mathbf{r}_{ib}^i\right\|_2\right)^3} + \frac{\mathbf{f}_\mathrm{ext}^i}{\mathrm{m}_1} \tag{B.10}$$

where $\mathbf{v}_{ib}^i$ is the satellite's inertial velocity defined in (2.4) and $\mathbf{f}_\mathrm{ext}^i$ is a vector representing the perturbing forces acting on the satellite like the solar radiation pressure force or the force due to atmospheric drag specified in Chapter 3.3. Thus, the circular orbit angular velocity $\boldsymbol{\omega}_{io}^o \in \mathbb{R}^\mathrm{n}$ may be calculated as

$$\boldsymbol{\omega}_{io}^o = [0 \quad -\boldsymbol{\omega}_0 \quad 0]^\top \text{ , where } \boldsymbol{\omega}_0 = \sqrt{\frac{\mu}{\left(\left\|\mathbf{r}_{ib}^i\right\|_2\right)^3}}. \tag{B.11}$$

The angular velocity from $\mathcal{F}_o$ to $\mathcal{F}_i$, expressed in orbit coordinates, can also be written as

$$\boldsymbol{\omega}_{io}^{o} = \mathbf{R}_i^o \frac{(\mathbf{r}_{ib}^i \times \mathbf{v}_{ib}^i)}{(\mathbf{r}_{ib}^i)^\top \mathbf{r}_{ib}^i} \;=\; \mathbf{R}_i^o \frac{\mathbf{S}(\mathbf{r}_{ib}^{\mathrm{i}})\mathbf{v}_{ib}^i}{\left\|\mathbf{r}_{ib}^i\right\|_2}. \tag{B.12}$$

Taking the time derivative of (B.12) gives

$$\dot{\boldsymbol{\omega}}_{io}^{o} = \frac{\mathbf{S}(\mathbf{r}_{ib}^i)\mathbf{a}_{\mathrm{ib}}^b(\mathbf{r}_{ib}^i)^\top \mathbf{r}_{ib}^i - 2\mathbf{S}(\mathbf{r}_{ib}^i)\mathbf{v}_{ib}^i(\mathbf{v}_{ib}^i)^\top \mathbf{r}_{ib}^i}{\left(\left\|\mathbf{r}_{ib}^i\right\|_2\right)^4} \tag{B.13}$$

for an elliptical (non-circular) orbit, where the Coriolis effect affects the satellite. For a perfect circular orbit, $\dot{\boldsymbol{\omega}}_{io}^{o}$ is equal to zero.
The satellite's position and velocity in $\mathcal{F}_o$ may be written as

$$\mathbf{r}_o = \mathbf{R}_i^o \mathbf{r}_{ib}^i, \quad \text{and} \quad \mathbf{v}_o = \mathbf{R}_i^o \mathbf{v}_{ib}^i \tag{B.14}$$

where the rotation matrix $\mathbf{R}_i^o$ has been defined in (2.29).

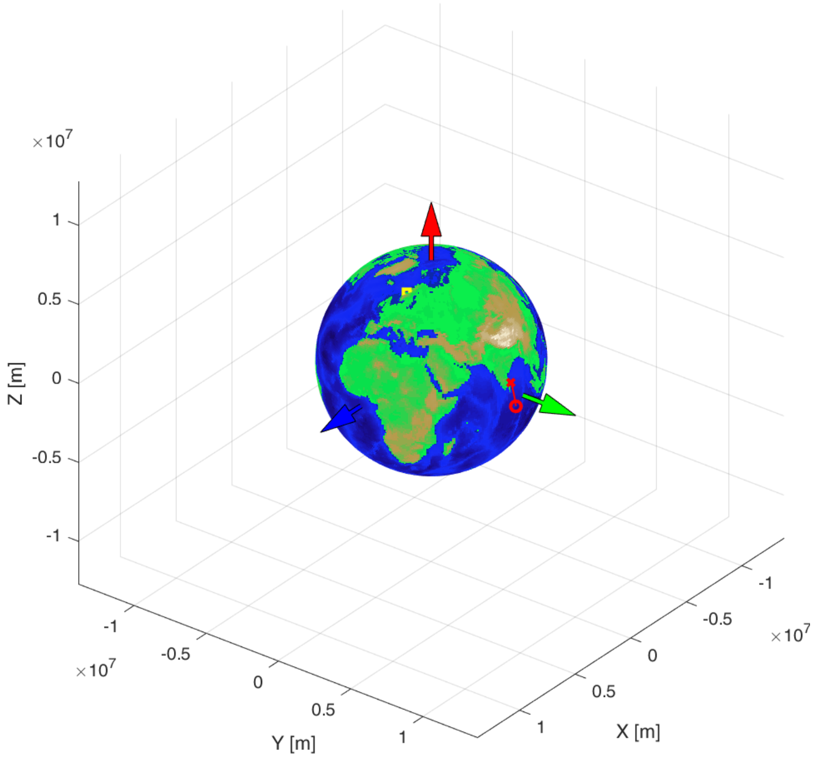

Figure B.1. – Orbit Simulation
[47]

Appendix C

Satellite Projects at NTNU

C.1 Previous Satellites

Until now, the NTNU has launched many satellite projects. Numerous master's theses have been written on the various satellite projects at NTNU. In 2002, satellite research began at NTNU. The name of the NTNU's first student satellite project was NCUBE, where the ADCS was equipped passively with a gravity-gradient boom and actively with magnetic torque coils. In the domain of controller design, this cubesat already applied an extended Kalman filter (EKF) [52]. Another previous satellite project was called NUTS, an abbreviation for NTNU Test Satellite, and it was launched in 2016 [53, p. 1]. The Norwegian Student Satellite Program (ANSAT) launched NUTS as one of three satellites. Research has been done on estimation methods for satellite attitude control within the NUTS project, like the quaternion estimator (QUEST) or extended quaternion estimator (EQUEST), applied to a nonlinear Mahony observer [54].

C.2 HYPSO Mission

The HYPSO uses a network of ground stations supporting its mission operations. The Mission Control Center at NTNU also operates robotic support systems such as unmanned aerial vehicles (UAVs), autonomous surface vehicles (ASVs), and autonomous underwater vehicles (AUVs) [5, p. 4].

Figure C.1 shows that the attitude maneuver combines target pointing with a slewing maneuver to produce pixels that overlap [5, p. 1]. HYPSO uses a network of ground stations supporting its mission operations and communicates with robotic support systems such as UAVs or ASVs.

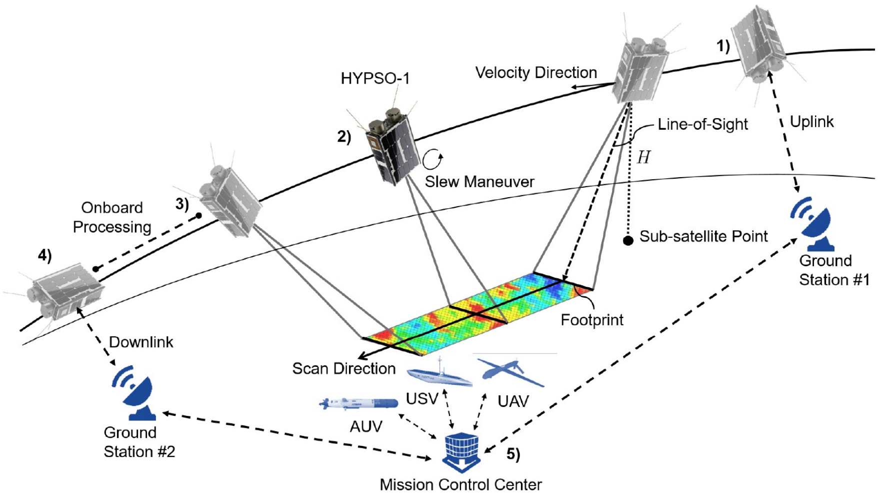

Figure C.1. – HYPSO mission
[5, p. 4]

The satellite undergoes specific operational mission modes, including detumbling, stabilization, estimating the state through star-tracking, hyperspectral imaging (HSI), and communicating with the ground station. The concept of operations for the HYPSO is specified in Table C.1. Under an emergency or anomaly (such as actuator failure or subsystems exceeding safety thresholds in terms of power), the satellite falls back to initializing. Then, the requirements are the same as in detumbling mode.

operational modes	description
imaging	HSI imaging (nadir), HSI imaging (slew maneuver), RGB imaging (nadir), RGB imaging (slew maneuver), combination of HSI and RGB imaging
onboard processing	e.g. compression of HSI frames in software and hardware, debug of HSI camera and / or RGB camera
file transfer	HSI images and RGB images are buffered from OPU to PC
uplink	files are uploaded through UHF and S-band
downlink processing	files are downloaded via UHF and S-band
safe mode	ensures that subsystems do not consume excessive power and functionalities are limited, electric power system (EPS) is triggered to safe mode
critical mode	EPS is triggered to critical mode
hardware critical mode	EPS is triggered to hardware critical mode, ADCS performs detumbling
launch and early orbit phase	stabilizing satellite's angular rate after orbital insertion which is known as detumbling, ADCS performs detumbling using MTQs, EPS and flight computer are the only subsystems turned on

Table C.1. – Mission operational modes

Appendix D

Implementation Details

This Appendix presents details on the implementation and the structure of the storage medium that is attached to this master's thesis.

D.1 Quadratic Programming Control Allocation Toolbox

As explained in Chapter 5.2.1, [49] is a part of the implementation. The m-functions for quadratic programming based CA are listed below:

- `sls_alloc`: active set, sequential least squares CA
- `sls_alloc`: active set, weighted least squares CA
- `mls_alloc`: active set, minimal least squares CA
- `ip_alloc`: interior-point CA
- `cgi_alloc`: cascaded generalized inverses CA
- `fxp_alloc`: fixed-point CA

The m-functions for constrained CA are listed below:

- `vview`: view visible virtual control set
- `vview_demo`: demo of `vview`

For direct and dynamic CA, the m-functions `dir_alloc` and `dca` are available in the toolbox. Other scripts provided by the toolbox are listed below:

- `iscoplanar`: test for coplanar controls
- `wpinv`: calculate weighted pseudoinverse

D.2 Implementation of all Attitude Cases

For each attitude case, there exist different folders (Pointing 1 to Pointing 13 and Slewing 1 to Slewing 13). Each folder has the same contents:

- subfolder `Figures`: figures of the original spacecraft model
- subfolder `Figures CGI`: figures of CA applied to the spacecraft model
- m-file `main`: case-specific settings, general model settings, and CA settings
  The simulation settings are saved as data files.
- data file `Pointing_Data` and `Slewing_Data`: simulation data of original spacecraft model
- m-file `Plots`: generate plots based on simulation data
- data file `Pointing_CGI_Data` and `Slewing_CGI_Data`: simulation data of CA applied to the spacecraft model
- `Plots_CGI`: generate plots based on CA simulation data

Appendix E

Simulation Results for Cases With Full Controllability

This Appendix presents complementary simulation results for the attitude tracking cases with full controllability.

E.1 Comparison for the Second Pointing Case

The following plots are complementary to the results in Chapter 6.1.1.

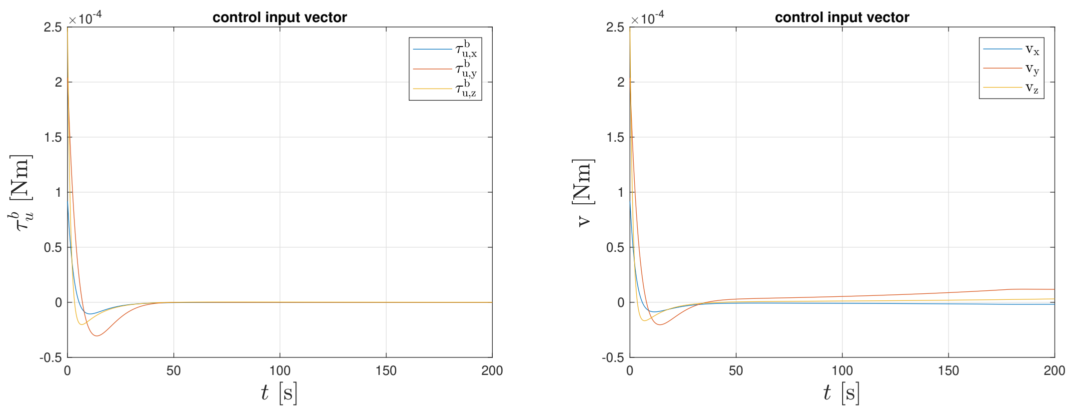

(a) (b)

Figure E.1. – PD controller torque without / with CGI CA

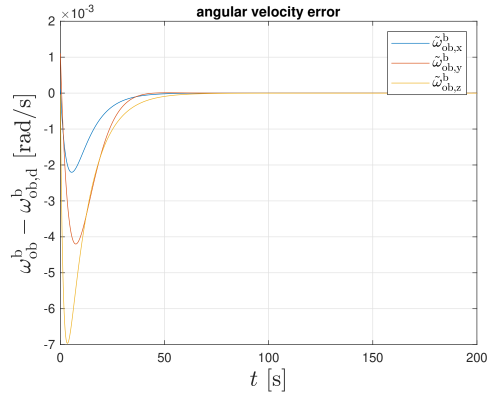

(a)

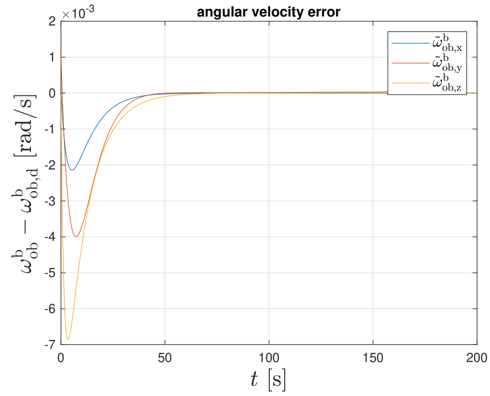

(b)

Figure E.2. – Angular velocity error without / with CGI CA

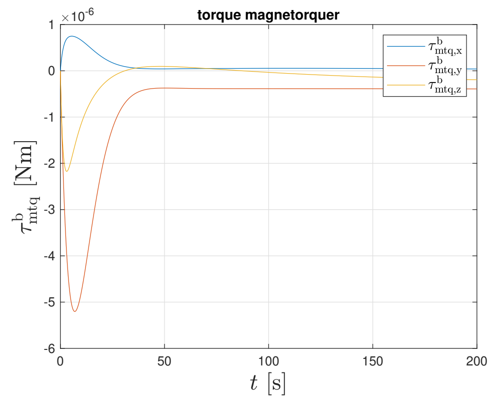

(a)

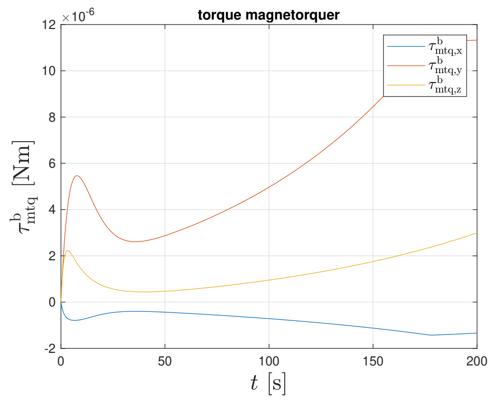

(b)

Figure E.3. – Magnetorquer torque without / with CGI CA

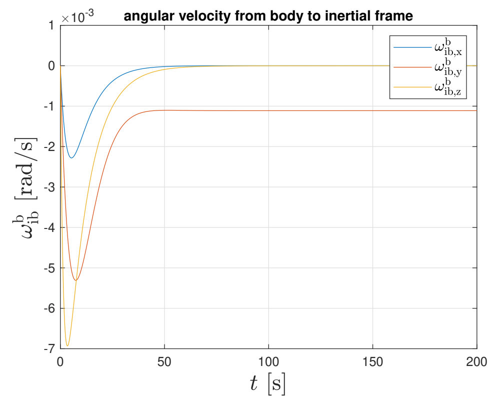

(a)

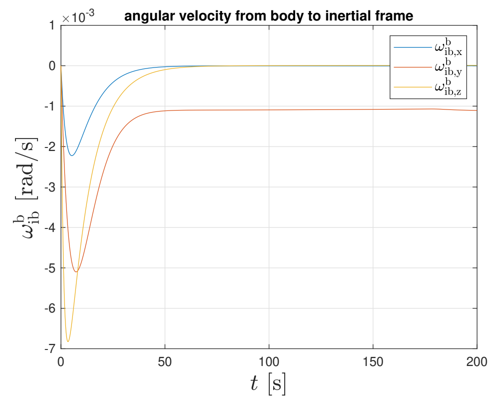

(b)

Figure E.4. – Angular velocity from $\mathcal{F}_b$ to $\mathcal{F}_i$ without / with CGI CA

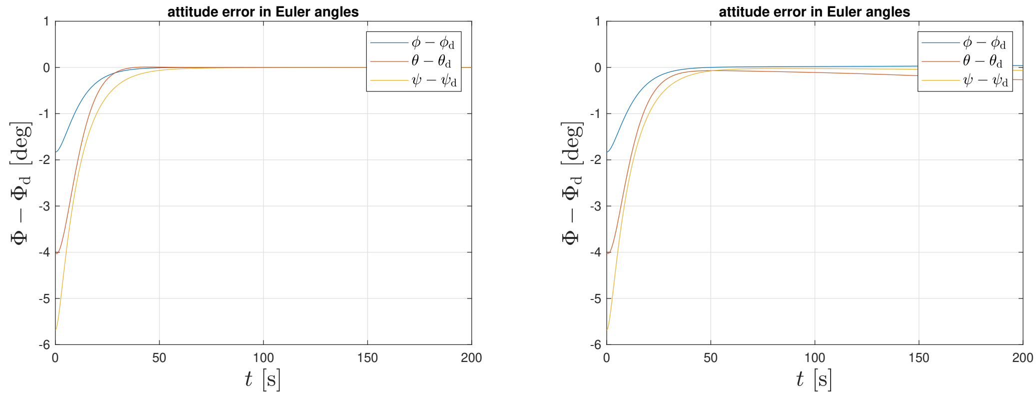

(a) (b)

Figure E.5. – Attitude error (Euler angles) without / with CGI CA

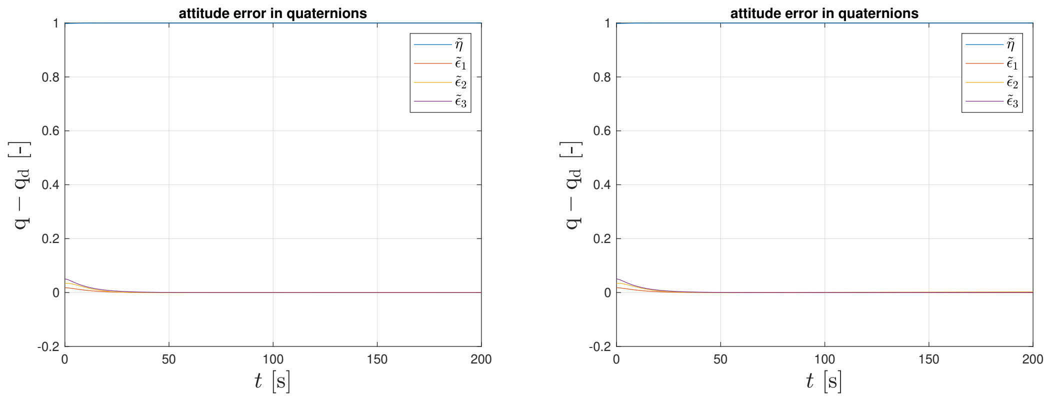

(a) (b)

Figure E.6. – Attitude error (quaternions) without / with CGI CA

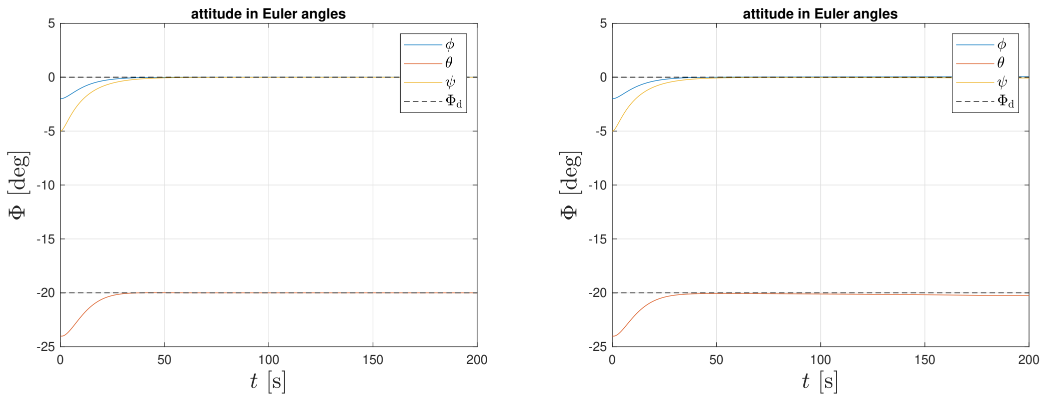

(a) (b)

Figure E.7. – Attitude (Euler angles) without / with CGI CA

E.2 Comparison for the Second Slewing Case

The following plots are complementary to the results in Chapter 6.1.2.

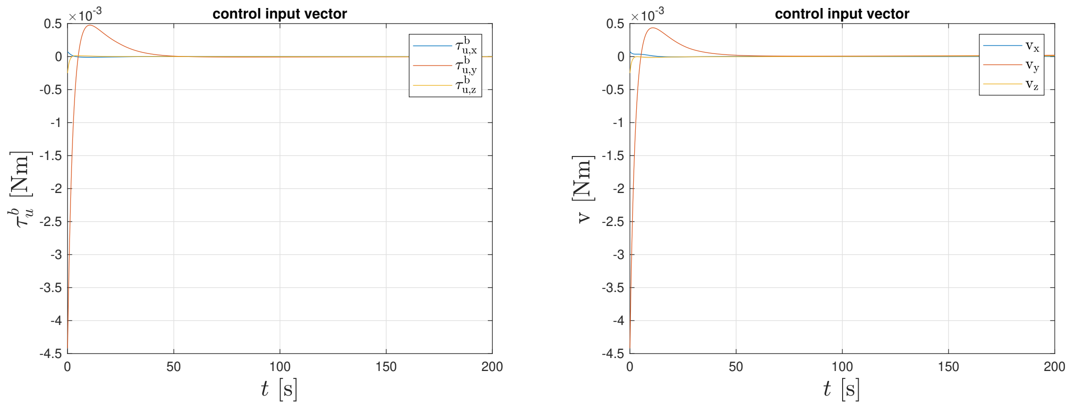

(a) **(b)**

Figure E.8. – PD controller torque without / with CGI CA

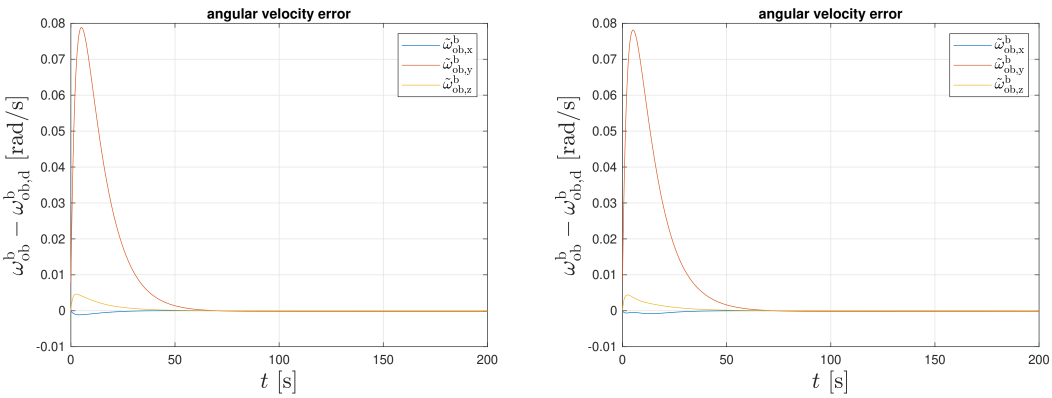

(a) **(b)**

Figure E.9. – Angular velocity error without / with CGI CA

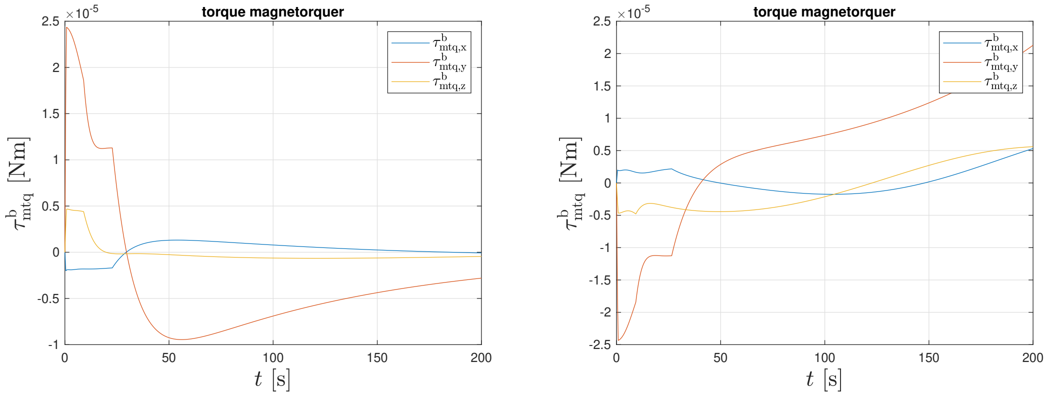

(a) **(b)**

Figure E.10. – Magnetorquer torque without / with CGI CA

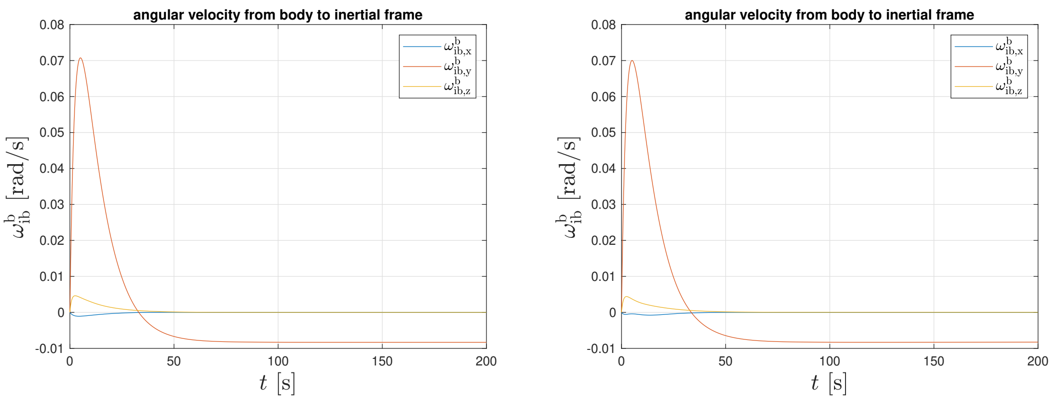

(a) **(b)**

Figure E.11. – Angular velocity from $\mathcal{F}_b$ to $\mathcal{F}_i$ without / with CGI CA

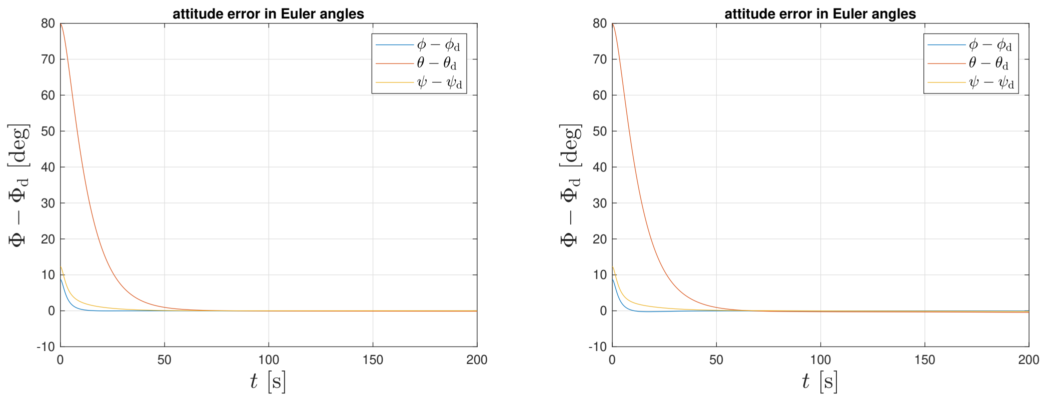

(a) **(b)**

Figure E.12. – Attitude error (Euler angles) without / with CGI CA

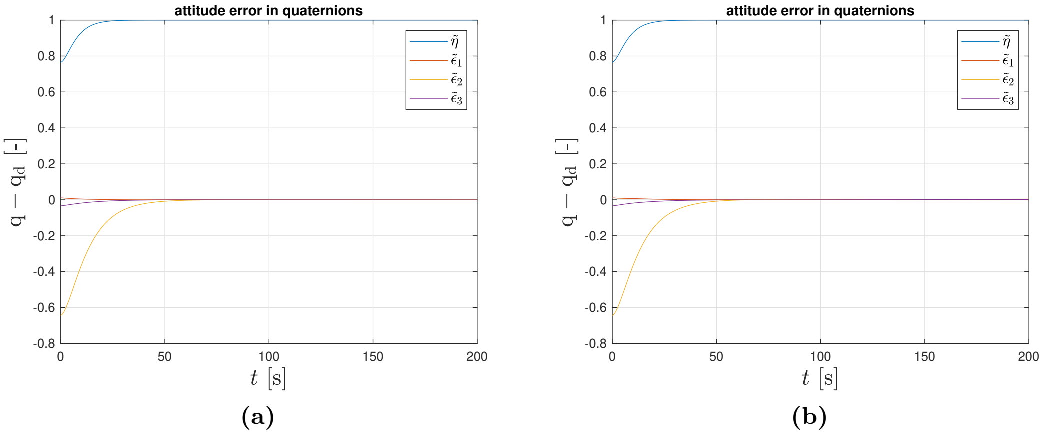

Figure E.13. – Attitude error (quaternions) without / with CGI CA

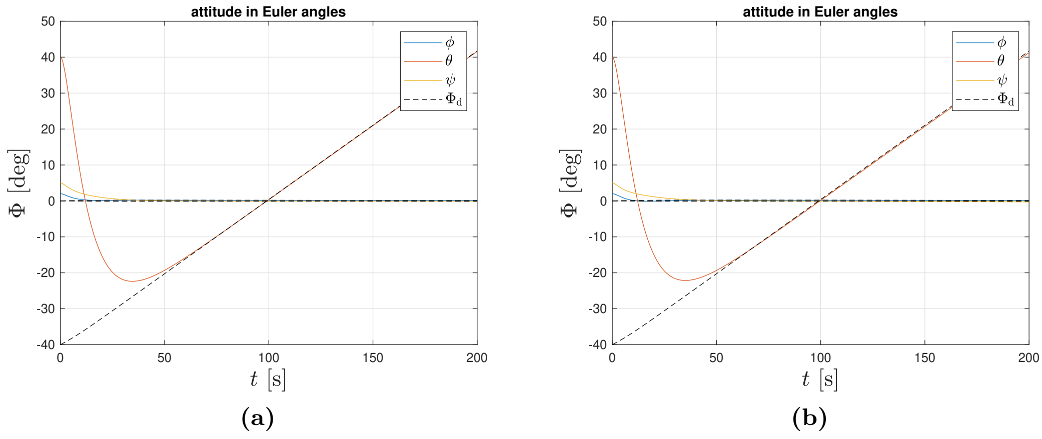

Figure E.14. – Attitude (Euler angles) without / with CGI CA

E.3 Comparison for the Ninth Pointing Case

The following plots are complementary to the results in Chapter 6.1.3.

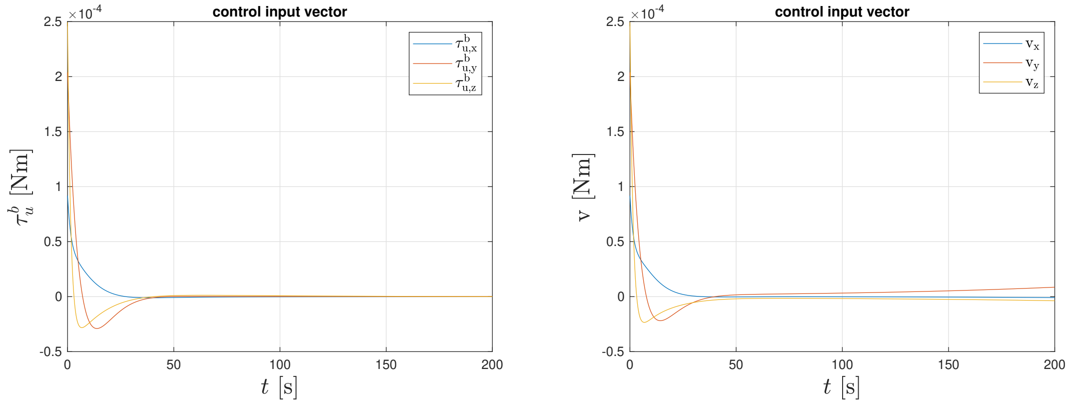

(a) **(b)**

Figure E.15. – PD controller torque without / with CGI CA

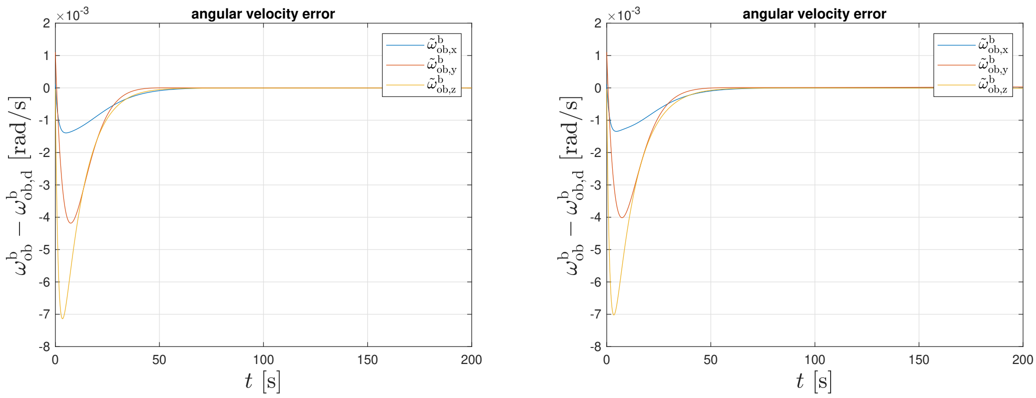

(a) **(b)**

Figure E.16. – Angular velocity error without / with CGI CA

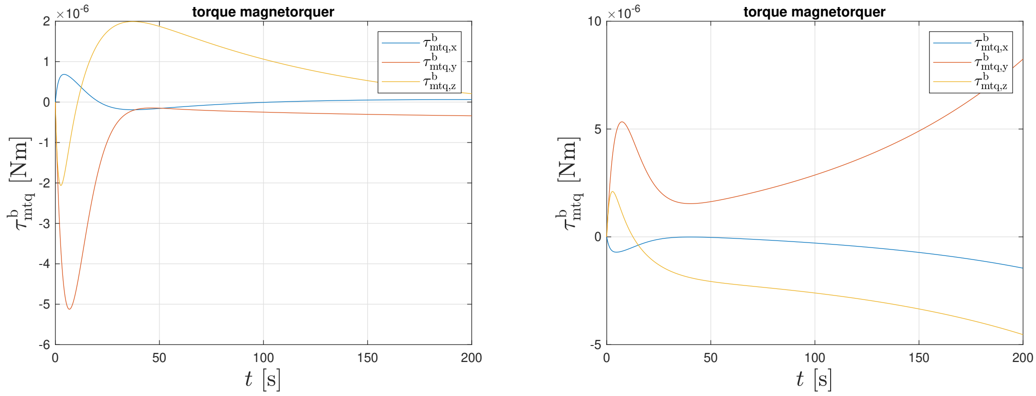

(a) **(b)**

Figure E.17. – Magnetorquer torque without / with CGI CA

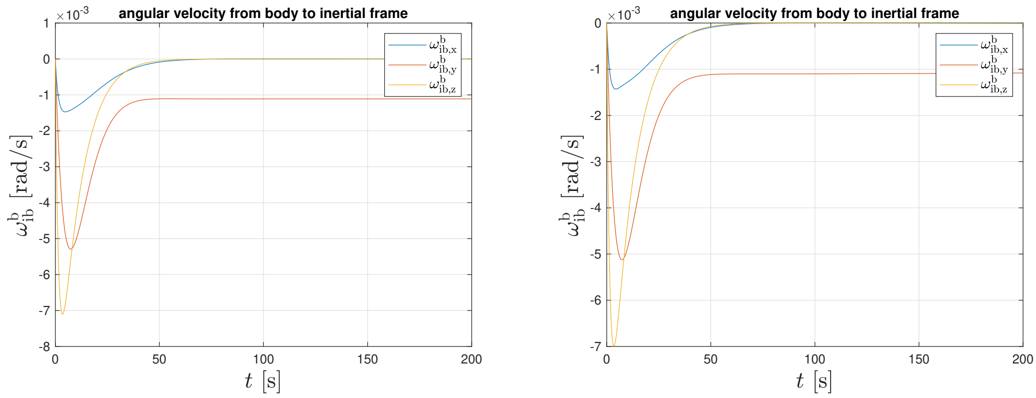

(a) **(b)**

Figure E.18. – Angular velocity from $\mathcal{F}_b$ to $\mathcal{F}_i$ without / with CGI CA

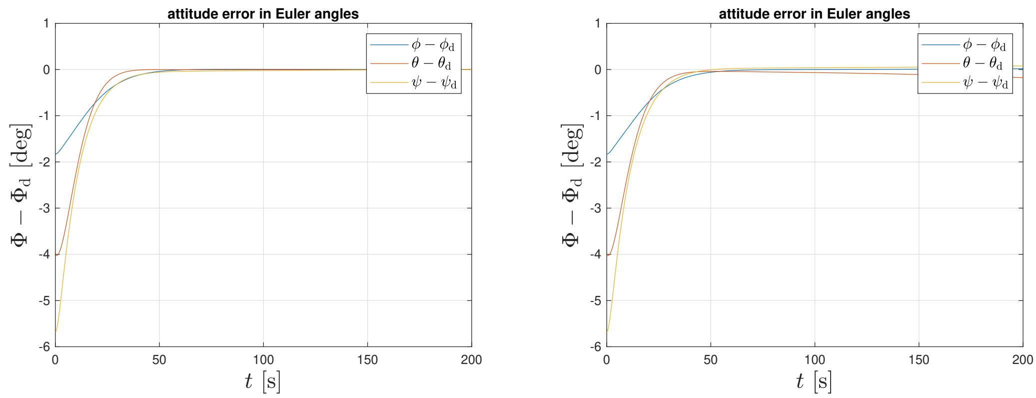

(a) **(b)**

Figure E.19. – Attitude error (Euler angles) without / with CGI CA

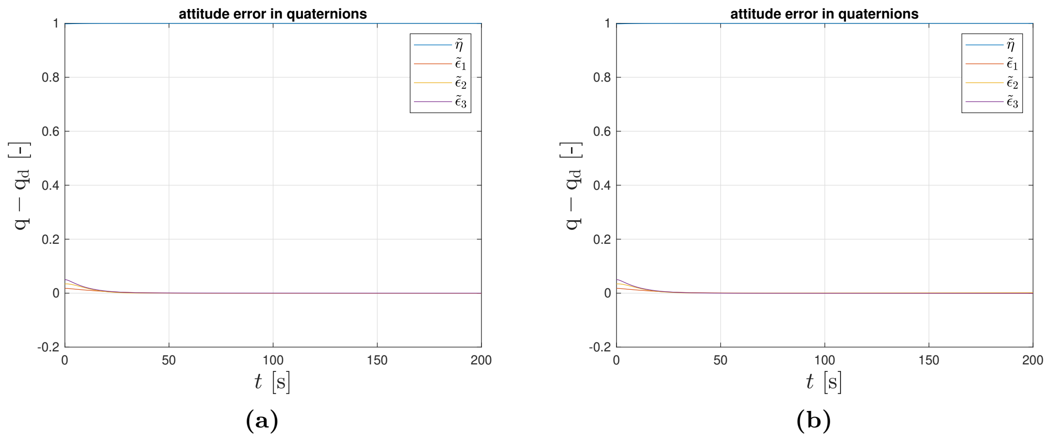

Figure E.20. – Attitude error (quaternions) without / with CGI CA

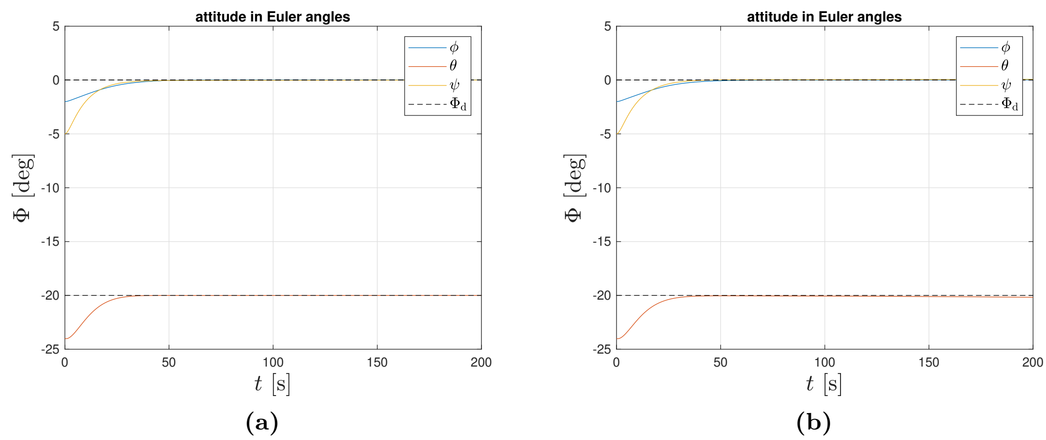

Figure E.21. – Attitude (Euler angles) without / with CGI CA

E.4 Comparison for the Ninth Slewing Case

The following plots are complementary to the results in Chapter 6.1.4.

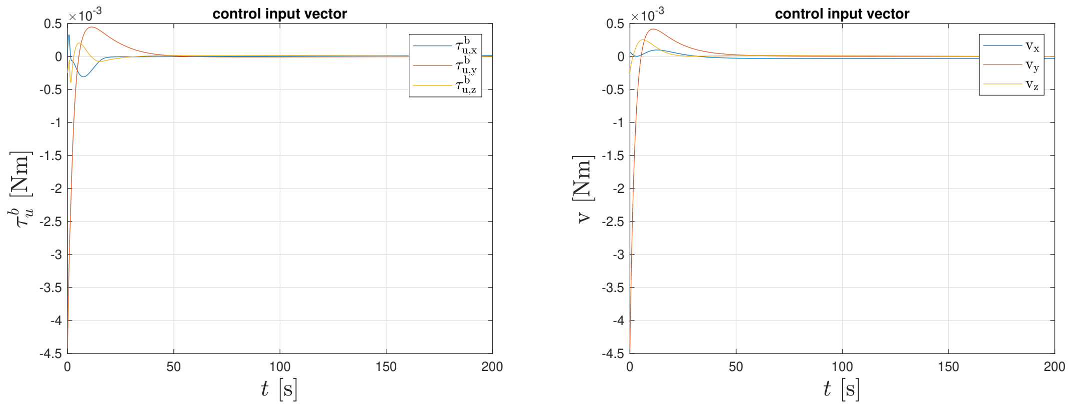

(a) (b)

Figure E.22. – PD controller torque without / with CGI CA

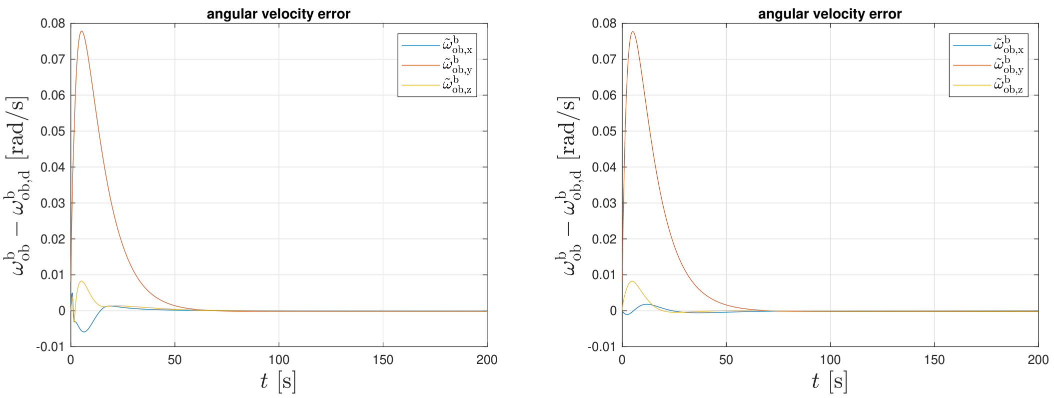

(a) (b)

Figure E.23. – Angular velocity error without / with CGI CA

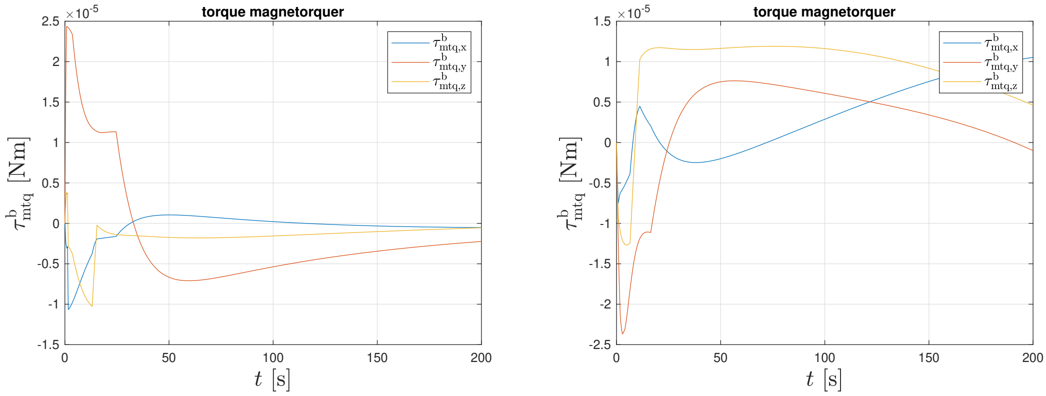

(a) **(b)**

Figure E.24. – Magnetorquer torque without / with CGI CA

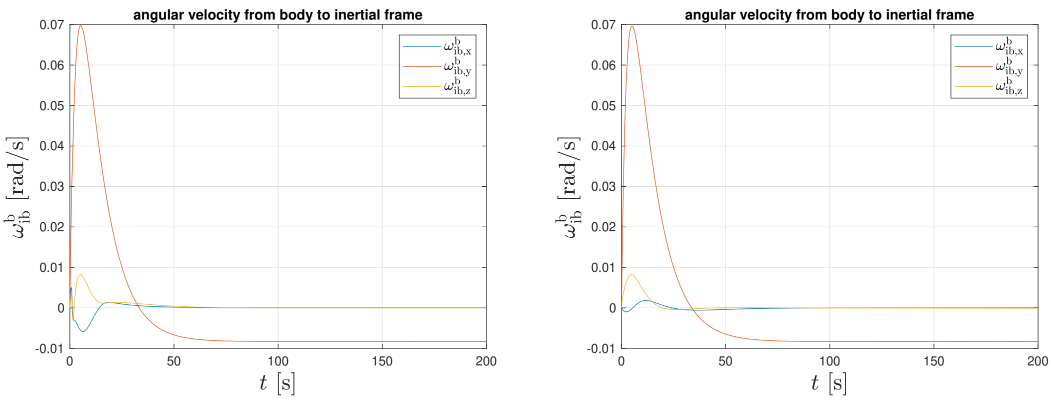

(a) **(b)**

Figure E.25. – Angular velocity from $\mathcal{F}_b$ to $\mathcal{F}_i$ without / with CGI CA

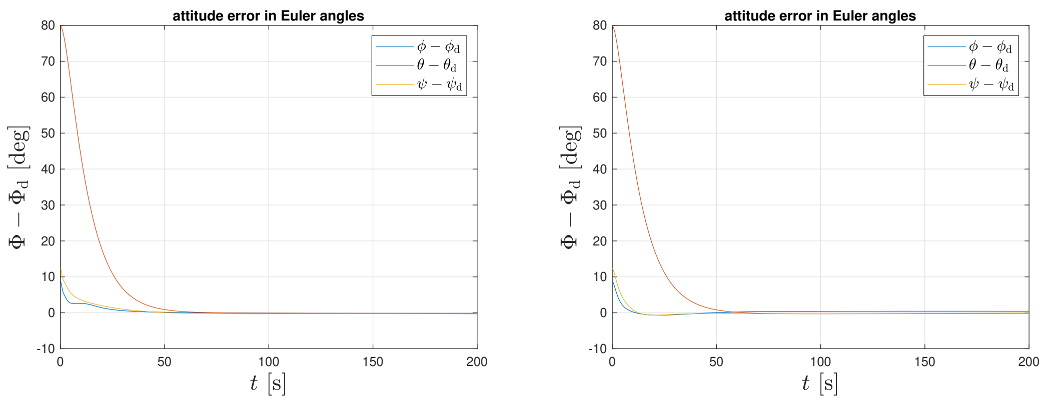

(a) **(b)**

Figure E.26. – Attitude error (Euler angles) without / with CGI CA

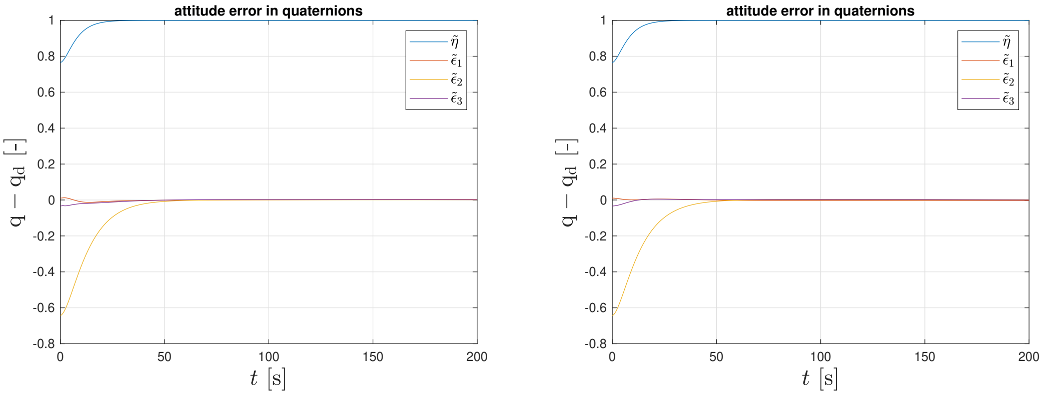

(a) **(b)**

Figure E.27. – Attitude error (quaternions) without / with CGI CA

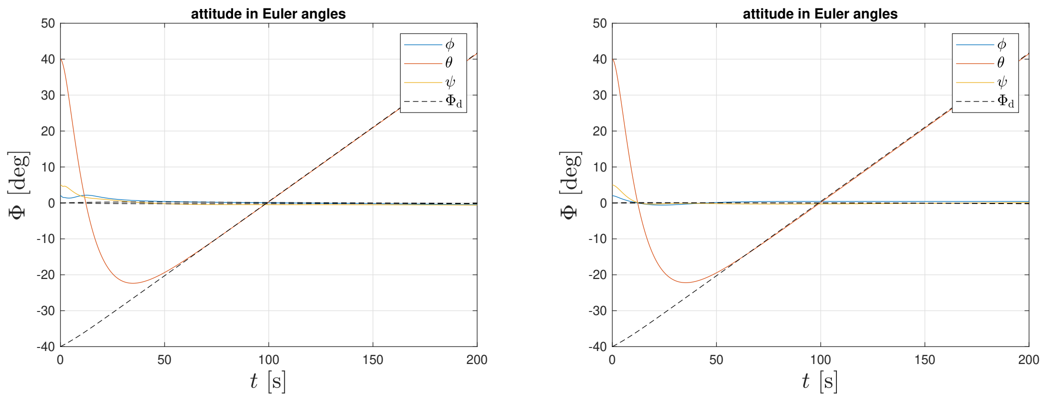

(a) **(b)**

Figure E.28. – Attitude (Euler angles) without / with CGI CA

Appendix F

Simulation Results for Cases Without Full Controllability

This Appendix presents complementary simulation results for the attitude cases without full controllability.

F.1 Comparison for the Twelfth Pointing Case

The following plots are complementary to the results in Chapter 6.2.1.

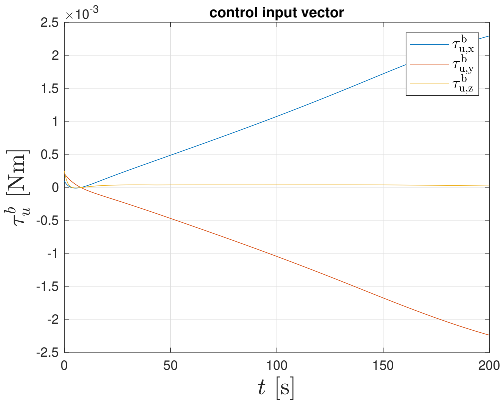

(a)

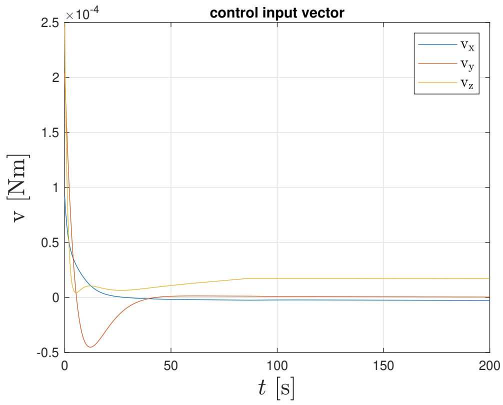

(b)

Figure F.1. – PD controller torque without / with CGI CA

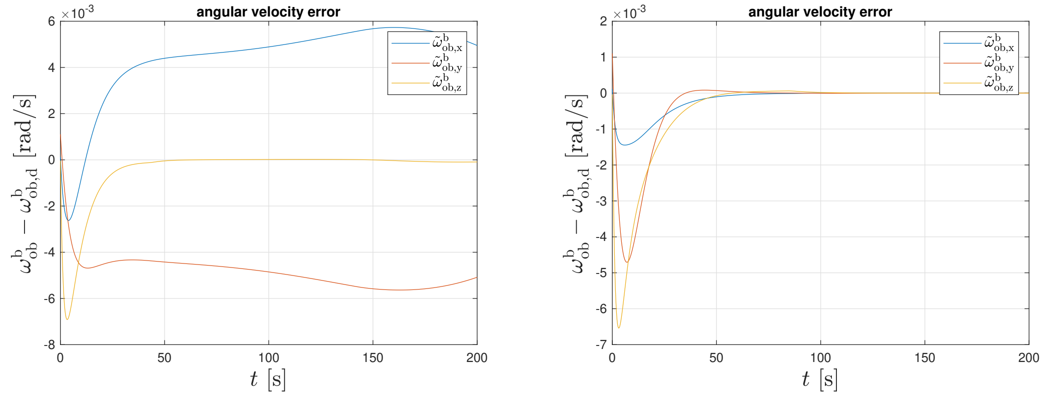

(a) **(b)**

Figure F.2. – Angular velocity error without / with CGI CA

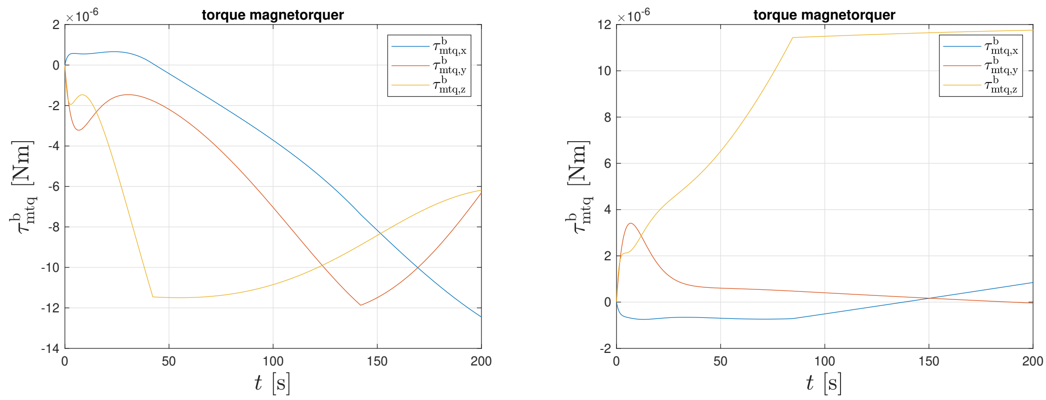

(a) **(b)**

Figure F.3. – Magnetorquer torque without / with CGI CA

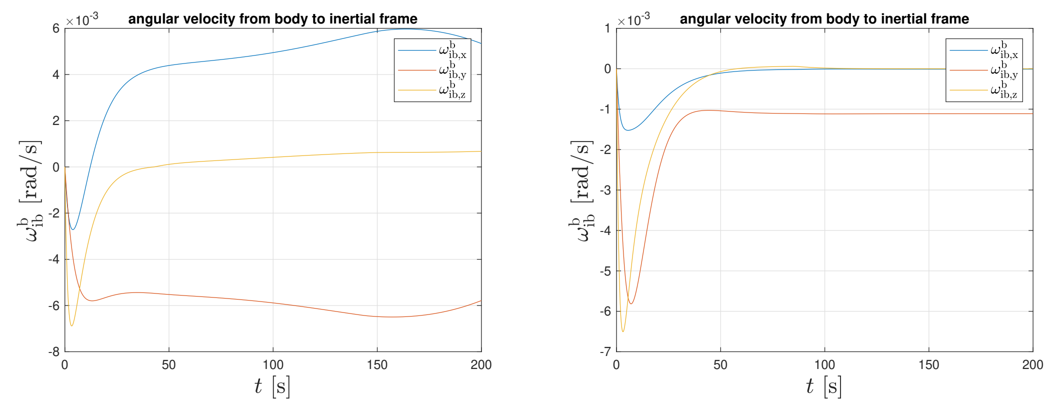

(a) **(b)**

Figure F.4. – Angular velocity from $\mathcal{F}_b$ to $\mathcal{F}_i$ without / with CGI CA

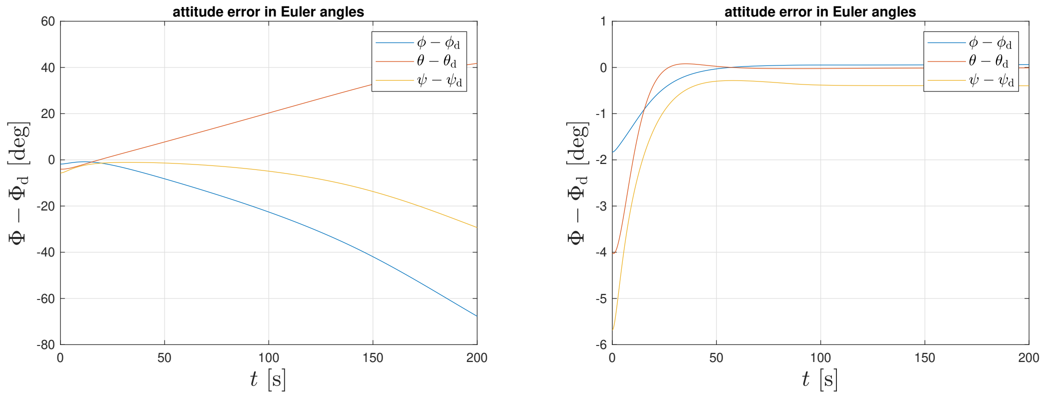

(a) **(b)**

Figure F.5. – Attitude error (Euler angles) without / with CGI CA

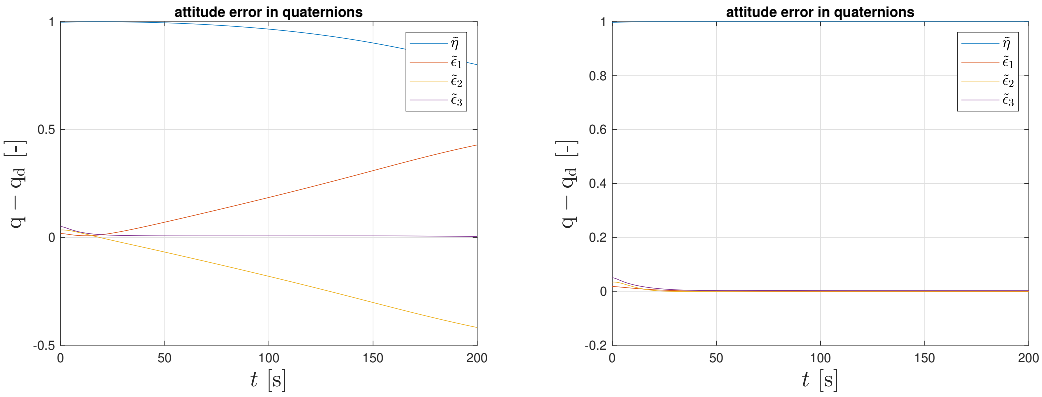

(a) **(b)**

Figure F.6. – Attitude error (quaternions) without / with CGI CA

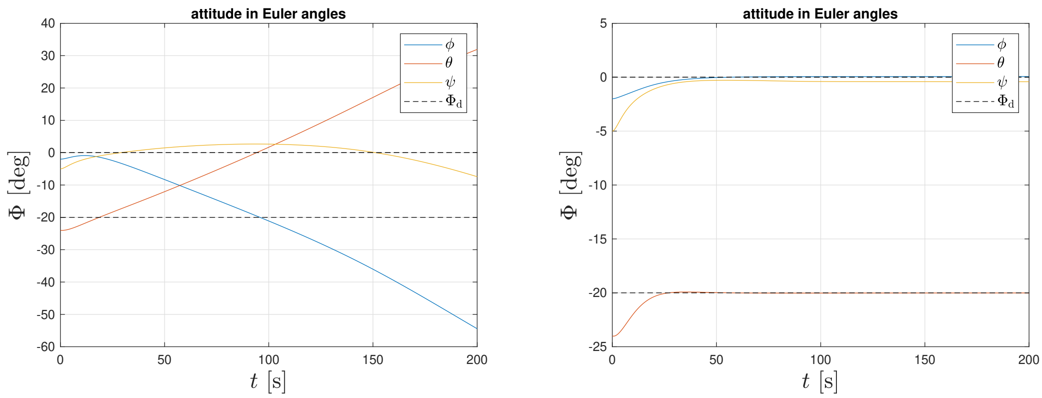

(a) **(b)**

Figure F.7. – Attitude (Euler angles) without / with CGI CA

F.2 Comparison for the Twelfth Slewing Case

The following plots are complementary to the results in Chapter 6.2.2.

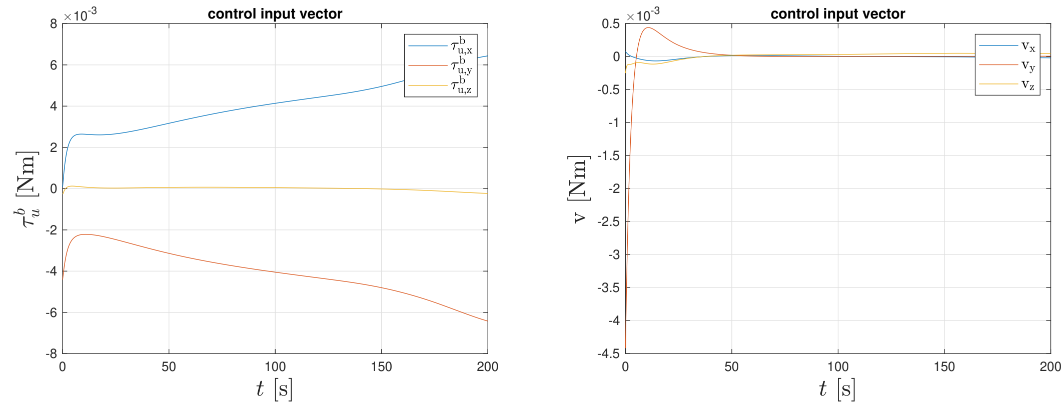

(a) **(b)**

Figure F.8. – PD controller torque without / with CGI CA

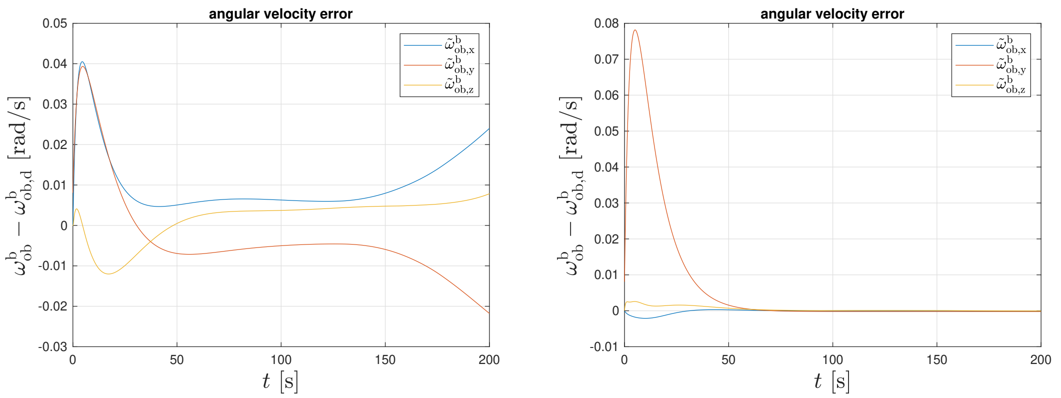

(a) **(b)**

Figure F.9. – Angular velocity error without / with CGI CA

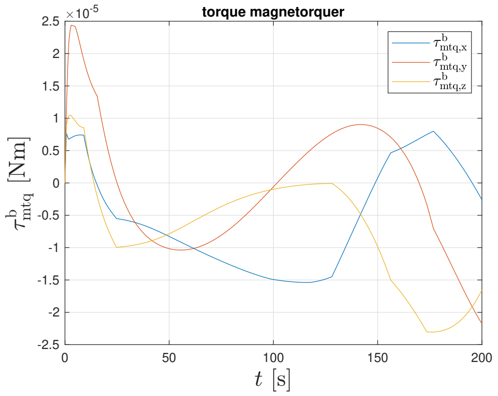

(a)

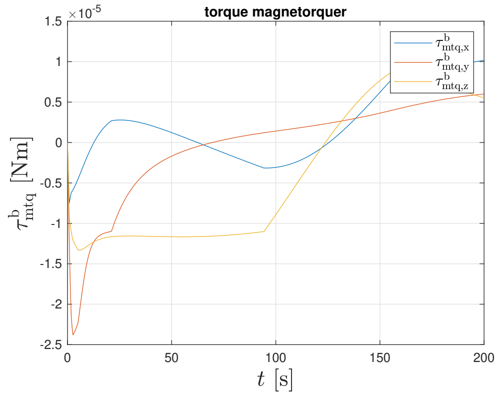

(b)

Figure F.10. – Magnetorquer torque without / with CGI CA

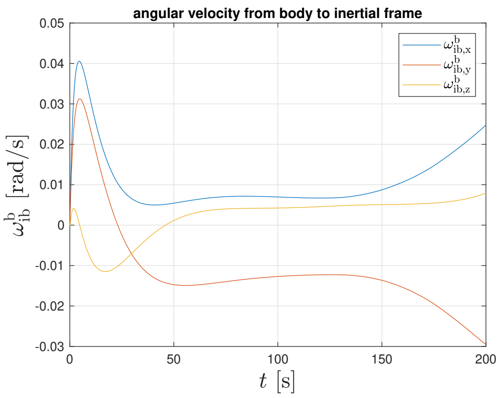

(a)

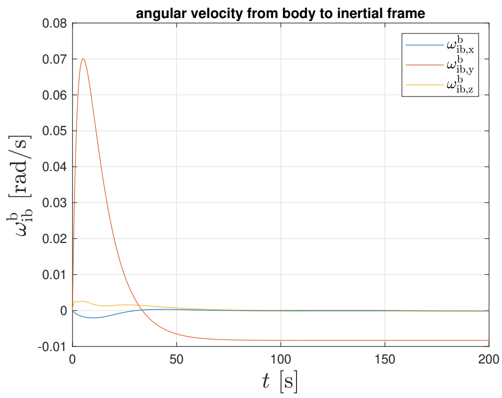

(b)

Figure F.11. – Angular velocity from $\mathcal{F}_b$ to $\mathcal{F}_i$ without / with CGI CA

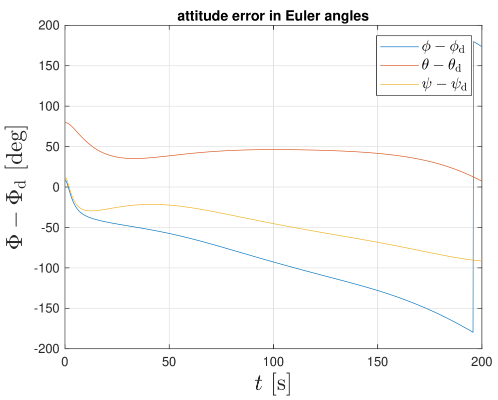

(a)

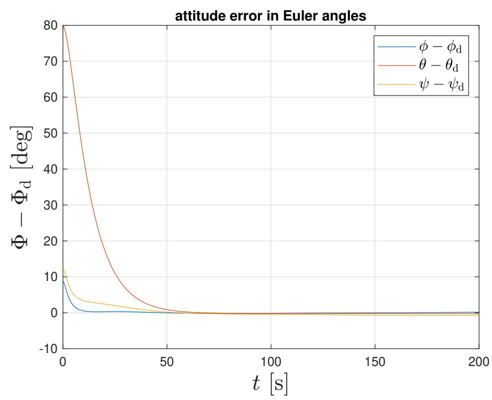

(b)

Figure F.12. – Attitude error (Euler angles) without / with CGI CA

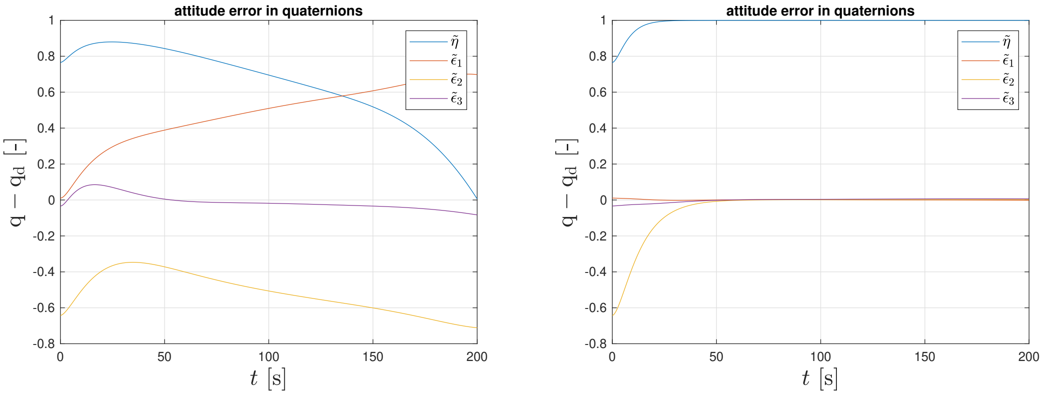

(a) **(b)**

Figure F.13. – Attitude error (quaternions) without / with CGI CA

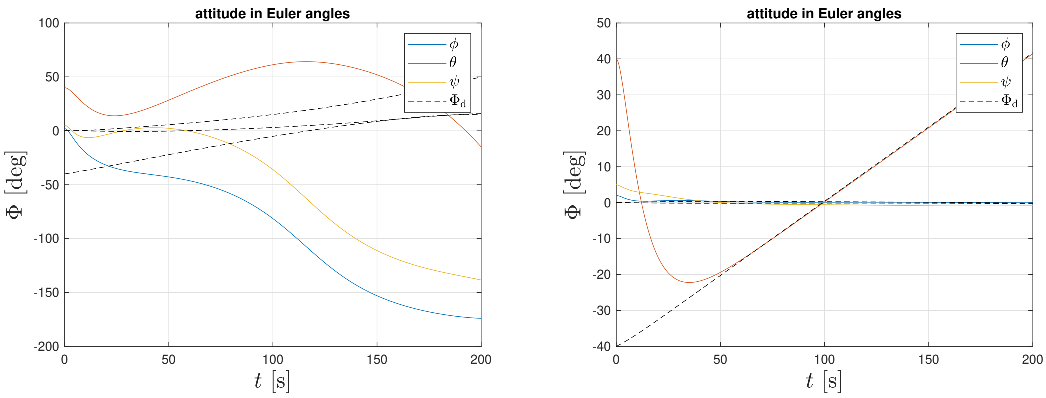

(a) **(b)**

Figure F.14. – Attitude (Euler angles) without / with CGI CA

F.3 Comparison for the Thirteenth Pointing Case

The following plots are complementary to the results in Chapter 6.2.3.

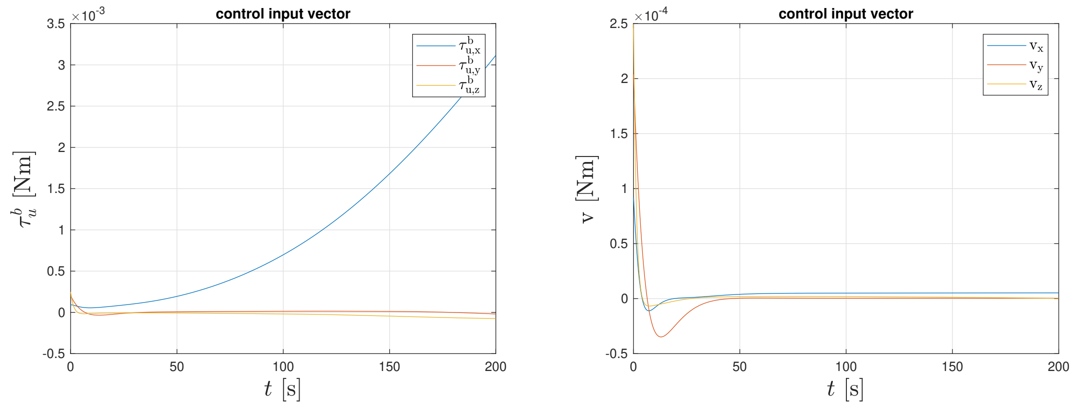

(a) **(b)**

Figure F.15. – PD controller torque without / with CGI CA

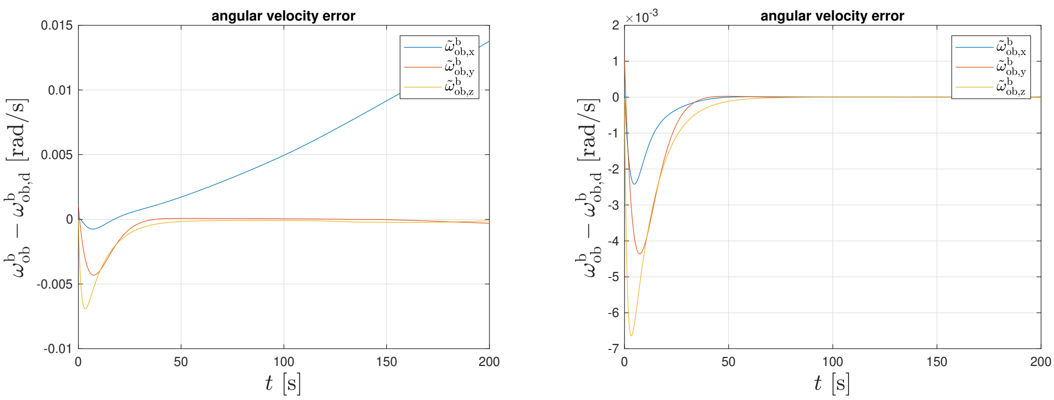

(a) **(b)**

Figure F.16. – Angular velocity error without / with CGI CA

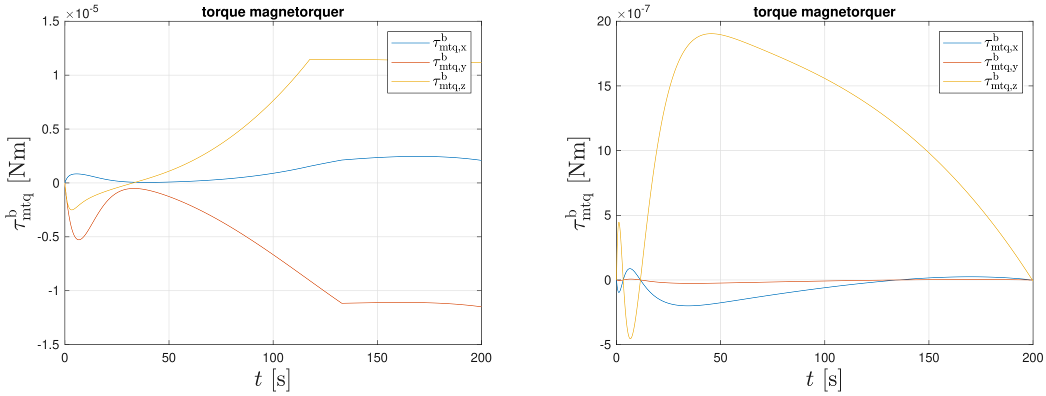

(a) **(b)**

Figure F.17. – Magnetorquer torque without / with CGI CA

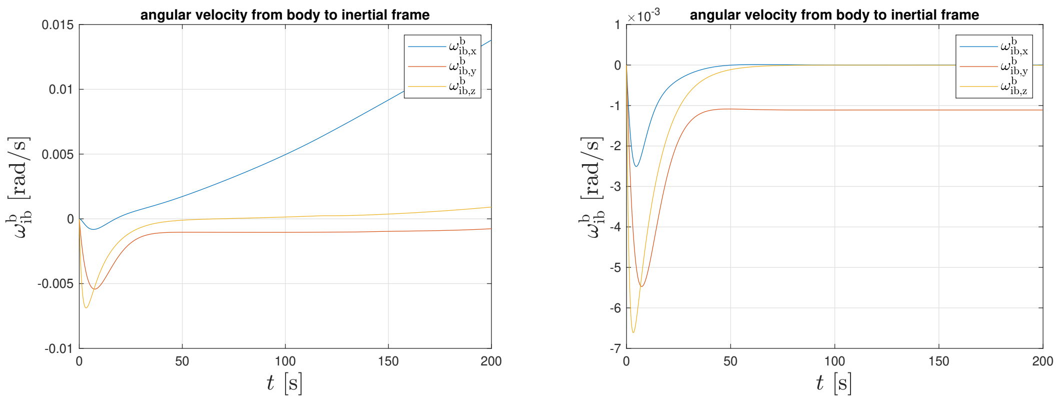

(a) **(b)**

Figure F.18. – Angular velocity from $\mathcal{F}_b$ to $\mathcal{F}_i$ without / with CGI CA

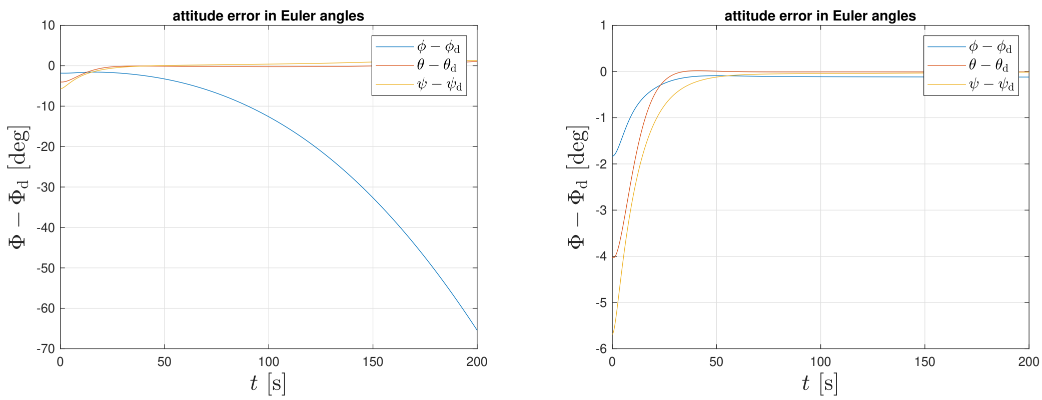

(a) **(b)**

Figure F.19. – Attitude error (Euler angles) without / with CGI CA

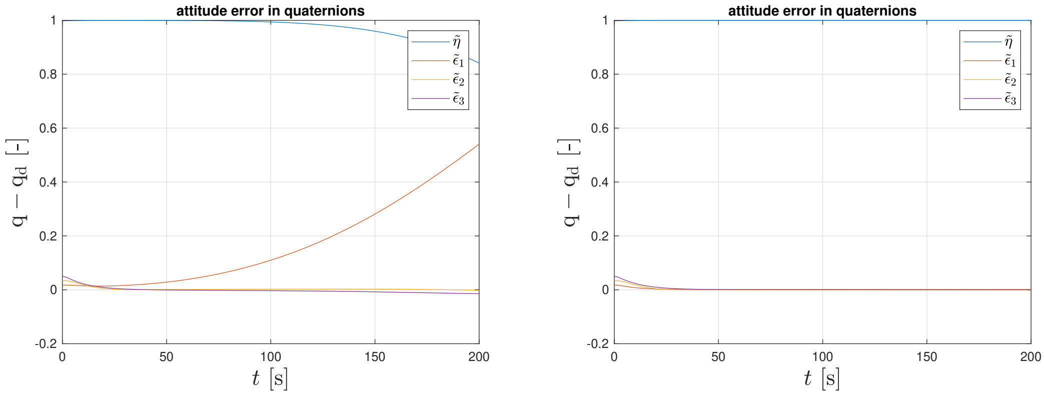

(a) **(b)**

Figure F.20. – Attitude error (quaternions) without / with CGI CA

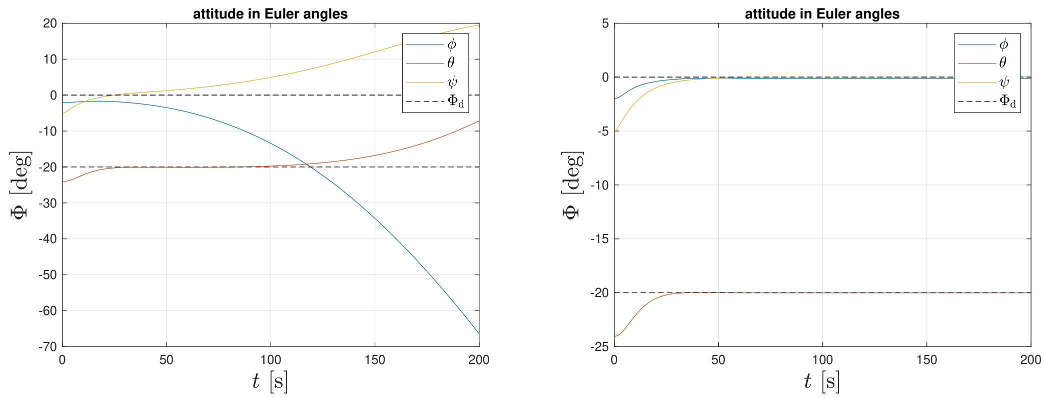

(a) **(b)**

Figure F.21. – Attitude (Euler angles) without / with CGI CA

F.4 Comparison for the Thirteenth Slewing Case

The following plots are complementary to the results in Chapter 6.2.4.

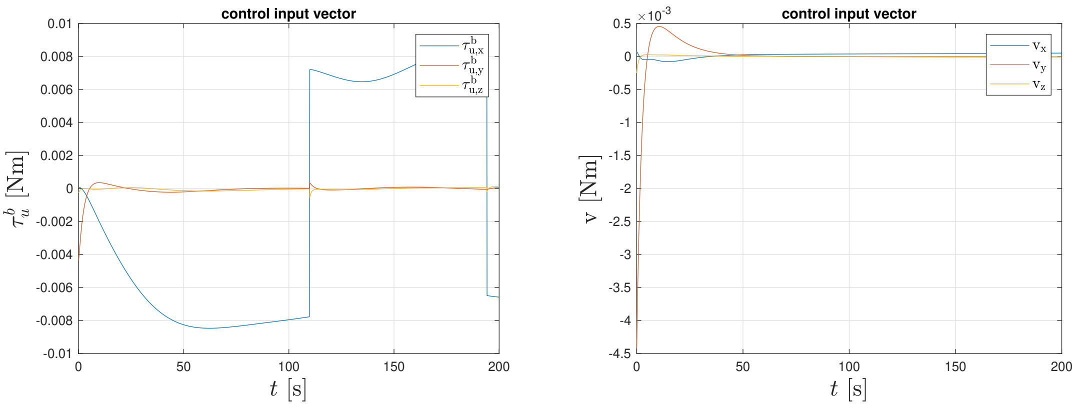

(a) (b)

Figure F.22. – PD controller torque without / with CGI CA

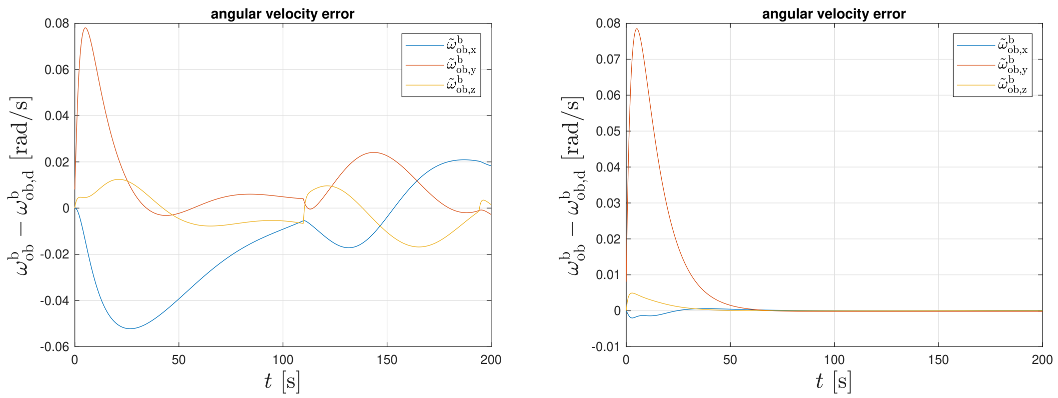

(a) (b)

Figure F.23. – Angular velocity error without / with CGI CA

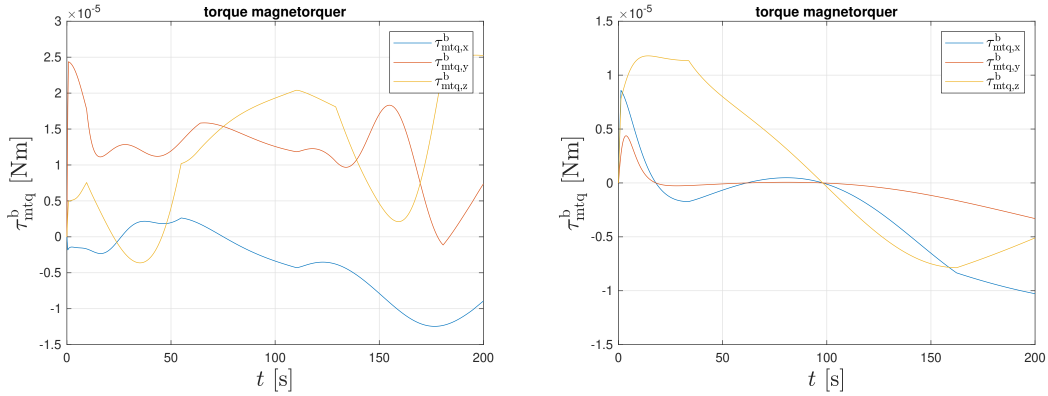

(a) (b)

Figure F.24. – Magnetorquer torque without / with CGI CA

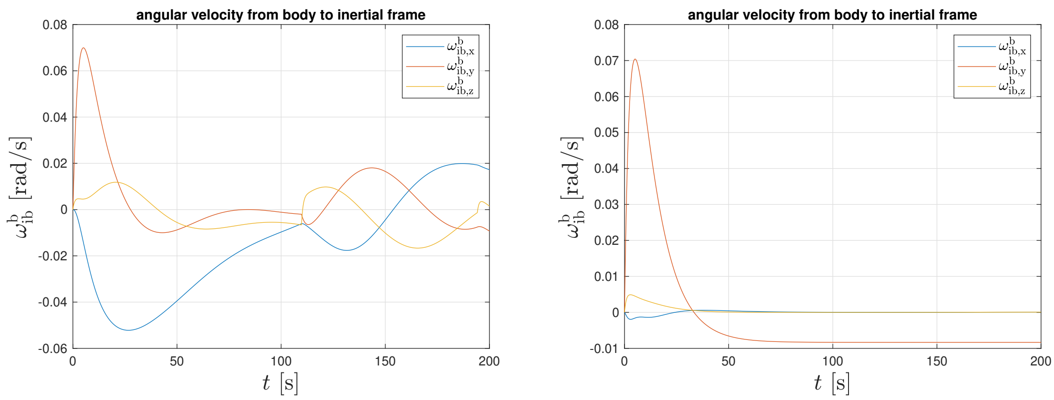

(a) (b)

Figure F.25. – Angular velocity from $\mathcal{F}_b$ to $\mathcal{F}_i$ without / with CGI CA

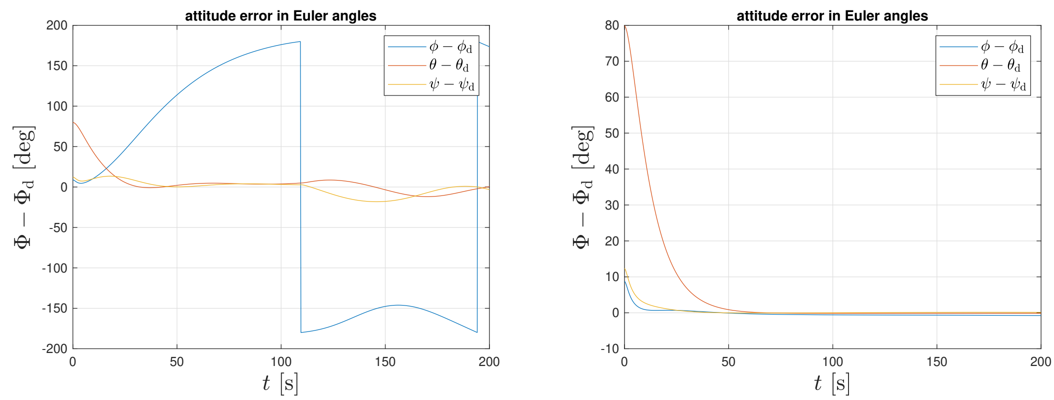

(a) (b)

Figure F.26. – Attitude error (Euler angles) without / with CGI CA

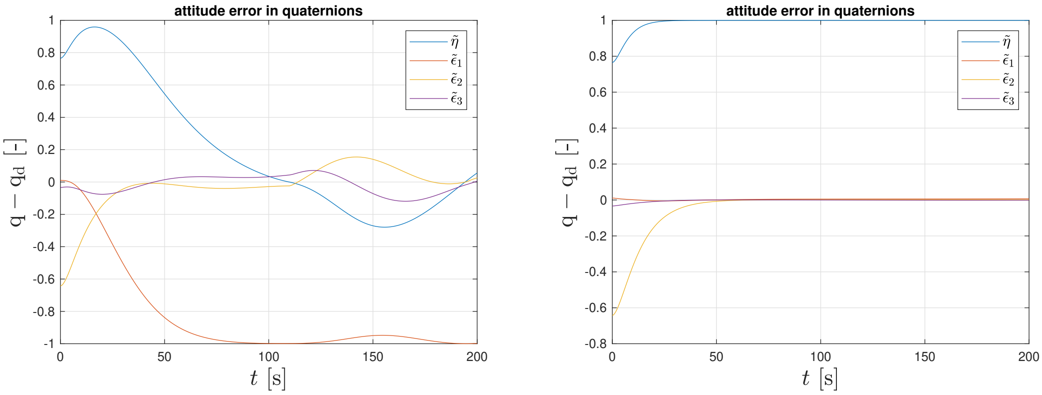

(a) **(b)**

Figure F.27. – Attitude error (quaternions) without / with CGI CA

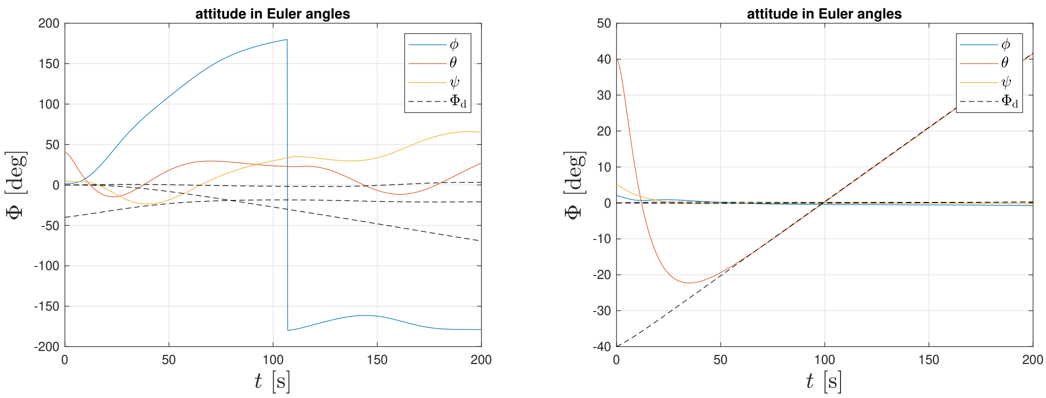

(a) **(b)**

Figure F.28. – Attitude (Euler angles) without / with CGI CA